Università di Pisa

Scuola di Dottorato "Galileo Galilei"
Dottorato in Fisica Applicata

Thesis:

A slow and cold particle beam for nanotechnological purposes

Candidato:
Nicolò Porfido

Supervisor:
Prof. Francesco Fuso

Contents

Foreword

The main topic of this thesis is to evaluate the applicative potential of a laser manipulated Cesium atom beam for specific technological purposes. As demonstrated by a range of measurements, the atom beam, produced out of a modified Magneto-Optical Trap (MOT), owns peculiar dynamical properties in terms of longitudinal velocity distribution of the particles and collimation, the latter achieved through transverse optical molasses.

Such features stimulated in the past efforts aimed at assessing the potential of the system in the frame of atom lithography, or Atomic NanoFabrication (ANF, see [1, 2]. Indeed, the apparatus, originally conceived for such purposes within a European collaboration (FP5 "Nanocold", 2001-2004), led to successful resist-assisted fabrication of parallel nanotrenches onto Gold [3]. However, the limited yield typical of laser cooled atom beams hampered diffusion of atom lithography as a tool alternative to conventional lithography in microelectronic industry.

Nonetheless, the interest to explore potential applications of laser cooled samples in view of the development of unconventional technologies survived. In the last years, great attention has been devoted to exploit the superior abilities of laser manipulation in determining the dynamical properties of vapor samples for the controlled production of charged particle beams. Charged particle beams are nowadays a key component of many technologies. For instance, Focused Ion Beams (FIBs) are emerging as an excellent tool to achieve fabrication, imaging, sculpturing at the nanoscale in a wide variety of materials, allowing users to get an unprecedented degree of control in *top-down* nanofabrication approaches.

In spite of the wide diffusion of FIB in both research laboratories and industrial environments, several problems exist which hinder further decrease of the transverse size in the ion beams, presently reaching the 2.5 nm range. Decreasing the transverse size would improve the spatial resolution of FIB-based techniques (as an example, nanopores with a diameter of about 2 nm have been obtained by ion sculpting [4]), which should ideally reach the single atom size. Among others, the main limitation occurs because of the

chromatic aberration in the ion focusing stage [5], depending in turn on the velocity distribution of the original ion sample. In the present technologies, the techniques adopted to create the ion sample lead in fact to thermal distributions of the kinetic energy, whose spread is reflected in aberrations.

Within such a technological context, it is clear that laser manipulation might produce neutrals which, once ionized through suitable methods, could allow for strongly monochromatic ion beams, able to overcome the limitations inherent to the present technologies. The main idea underlying this thesis work is to photoionize the laser cooled Cesium atom beam produced out of the modified MOT in order to obtain an ion beam, whose properties should in principle depend on the peculiar dynamics of the original neutral beam. Such an effort is carried out within a European collaboration (FP7-MC-IAPP, Industry-Academia Partnerships and Pathways, Project "COLDBEAMS", 2010-2014) with Université Paris-Sud, Orsay (project coordinator Prof. Daniel Comparat) and Orsay Physics, a French industry leader in the development of columns for FIB.

The thesis focuses mostly onto the demonstration of phoionization and analysis of the so-produced ion beam, including a spectroscopy investigation of optical pumping effects on the atom beam. The work carried out prior to the beginning of the new research project, leading essentially to the realization of a robust "slow" and "cold" Cs beam, is summarized in order to determine the dynamical properties of the atoms.

The thesis is organized as follows:

Chap.$\sim$ 1 discusses the technological topics related to the thesis and poses the main scientific motivations of our efforts;

Chap.$\sim$ 2 provides a brief introduction to the Doppler laser cooling and magneto-optical trapping, describing the relevant properties of the Cesium atom and of its interaction with monochromatic radiation in a two-level model approximation;

Chap.$\sim$ 3 extends the analysis of chap. 2 to include the interaction between radiation and multilevel atoms, focusing on the origin of optical pumping and sub-Doppler cooling mechanisms;

Chap.$\sim$ 4 treats the laser-cooled ion beams; in this chapter the expression of the ionization rate for the two-photon, two-color ionization scheme used in our set-up is derived. Furthermore, the expected performances of the so-produced ion source are discussed and compared with other approaches.

Chap.$\sim$ 5 gives an overview of the several parts of the experimental apparatus used to produce the atomic beam;

Chap.$\sim$ 6 shows the results of the measurements made on the atomic beam in order to determine its density, average value and spread of the longitudinal velocity and transverse intensity distribution;

Chap.$\sim$ 7 shows the results of measurements made on the cold ion beam to determine the CW ion yield; furthermore, the effects of the optical pumping on the ion yield are highlighted. Finally, average value and spread of the ion longitudinal velocity distribution are determined by Time-Of-Flight measurements.

Chapter 1

Introduction: laser manipulation and technology

In this chapter we provide an introduction to the general framework of this thesis. In section 1.1 we illustrate the current status of the miniaturization process in the nanotechnological field, while section 1.2 shows the properties of the laser cooling techniques that can be relevant for nanofabrication purposes. Finally, in section 1.3 we present the recently introduced application of laser cooling methods to the production of ion beams with better dynamical properties with respect to the present ones.

1.1 The quest for miniaturization

Nowadays, the continuous trend towards the miniaturization in nanotechnology stimulates the quest for new fabrication methods, capable of addressing the weaknesses of the present ones and, eventually, of superseding them.

The more urgent requests come from the semiconductor industry whose production cycles are, at present, based almost completely on the photolithographic *top-down* process.

Optical lithography is a "subtractive" method, in which the structures are defined removing material on the surface of the substrate. Subtractive methods are at present dominant in the semiconductor industry, and very

probably they will continue to be for the next years [6]. At present, the state of the art in the lithography is the process at 22 nm, introduced by IBM in 2008 in a single 6-transistor SRAM cell [7] and that, most probably, will be developed on the large scale production by Intel (that will start the delivery in May 2012 with the microarchitecture *Ivy Bridge* in the *Core iX* CPU family).

The current predominance of these methods is essentially due to two reasons: i) they are *parallel*, thus intrinsically efficient; ii) they are well known and, thus, well optimized: for example, at present the average wafer yield of a fab (site for the production of integrated circuits) is very high, up to 200 wafers (standard 300 mm diameter) per hour [8]. However, despite the efficiency and the optimization of the optical lithography methods, the presence of fundamental limits due to diffraction phenomena strongly suggests, even if not in the foreseeable future, the necessity of implementing alternative approaches.

The problem is felt so seriously in the integrated circuit manufacturing that the candidate substitutes, actively developed since the last years, have been categorized under the specific label of Next Generation Lithography (NGL) [9]. This broad family includes extreme ultraviolet lithography (EUVL), electronic and ion beam lithography (EBL and IBL), scanning probe lithography (SPL) etc.

Each one of these methods has its own advantages and disadvantages. EUVL is the most promising candidate to bring the integrated circuits fabrication process under the 10 nm limit and to substitute the optical lithography in the near future. However, it is still a lithographic method that, therefore, does not overcome the diffraction limit, but simply shifts it to smaller scales exploiting shorter wavelength radiation (20 nm against the presently used 193 nm ArF laser radiation). Furthermore, it is connected to relevant technological problems that only very recently seems to have been partially solved [10], due to the absorption of EUV by materials, imposing the use of reflective optics, with a completely new engineering of the fabrication devices. About EBL, IBL and SPL, their advantage is that completely arbitrary patterns can be produced, and the extremely small de Broglie wavelength of particle

beams eliminates completely, in practical terms, the diffraction limit [11]. The evident disadvantage is that they are serial methods; even if a 10 nm resolution has been reached with EBL almost 40 years ago [12], the pattern time for a 10 mm diameter silicon wafer, about 1 h, never made this method attracting for industry. The weaknesses of these methods will probably prevent their exploitation in the context of the atom scale technologies.

Parallel to the lithographic subtractive methods, in the last years another huge family of processes, the "additive" ones, have been developed. These rely on the direct fabrication of nanostructures through the deposition of material, usually in the vapor state, manipulated to make it impinge on the surface of a substrate in a highly controlled way. At present, these methods do not appear as a ready-to-use alternative to the lithographic ones. However, it is not an utopia to think that these processes could actually *integrate* the present ones, filling their deficiencies.

1.2 The envisioned use of laser manipulation

Since direct deposition methods are fundamentally based on the manipulation of vapors, they can be assisted in this task by the well developed laser-cooling techniques. In fact, the laser manipulation of vapors has advanced significantly in the last decades for an extremely wide range of applications, spanning from fundamental to more applicative ones: Bose-Einstein condensates, molecular cooling, metrology, coherent matter, quantum information.

Among the applications of laser-cooling, *atom lithography* [13–15], known also as atomic nanofabrication (ANF) [1, 2, 16, 17], is worth to be cited. With this technique, mimicking the optical lithography with a reversal in the roles of matter and radiation, using the experimental apparatus on which the work reported in the present thesis has been carried out, nanostructures with 30 nm feature width [3] have been produced, in years in which the industry was implementing the process at 90 nm.

Although the quite small *critical dimension* of the structures produced, these techniques never left the laboratory status. In fact, the main drawback lying in the use of laser cooling techniques that, in the actual world, hampered

their large scale use, is in general the relatively low particle yield intrinsic of this kind of techniques.

As mentioned above, very unlikely techniques based on laser-cooling will ever be implemented on an industrial scale. Anyway, there are several niches in the semiconductor industry in which laser-cooling based methods could actually integrate existing approaches. First of all, laser cooling methods are quite flexible, especially in terms of usable atomic species: Sodium [13], Chromium [15], Aluminum [18], group III elements [19] like Gallium [20], Indium [21], Cs [22], Iron [23, 24], Erbium [25] and Ytterbium [26] have been laser manipulated. This list includes elements like Erbium and Ytterbium, used, for example, in the doping of optical fibers and, as salts, for the production of laser devices, or like Chromium, a very important material in the semiconductor industry, since it is used to fabricate the photomasks. In the fabrication of a mask (the "master") a high flux and an efficient particle yield are not very stringent requirements, as they are in the lithography of the Si wafers (the "replica"). For example, a low-flux deterministically controllable Chromium cold source [27–30] could actually find a quite immediate application in the production of the *grayscale* masks [31]. These masks, as the name suggests, are characterized by patterns in which the transition between blank and opaque zones is not abrupt, like in the conventional binary masks, but, on the contrary, takes place in a gradual way; for these features they are mainly used in Micro-Electro-Mechanical Systems (MEMS) fabrication, where they enable the production of 3D structures with smoothly varying slopes and vertical patterns. The transition zones are made of variable size Chromium dots, whose dimensions must be highly controlled since they determine the local transmittance of mask. It is thus evident that the fabrication of this kind of masks could take advantage of the control possibilities on the size of the directly deposited dots, offered by a deterministic source of cold atoms.

1.3 Laser manipulation and ion beams

Very recently, there has been a resurgence of interest in laser cooling techniques in the context of the focused ion beams (FIB) [32], tools used for a variety of tasks like failure analysis [33], lithographic mask repair [34], microscopy [35], TEM specimen preparation [36] and maskless dopant implantation [5].

The versatility of the FIBs arises from the variety of physical phenomena taking place when an ion beam is directed onto a substrate material [37]. In fact, energetic ions hitting the surface of a solid sample lose energy to the electrons of the solid as well as to its atoms. The most important physical effects of incident ions on the substrate are: sputtering of neutral and ionized substrate atoms (this effect enables substrate milling), electron emission (this effect enables imaging, but may cause charging of the sample), displacement of atoms in the solid (induced damage) and emission of phonons (heating). Chemical interactions include the breaking of chemical bonds, thereby dissociating molecules (this effect is exploited during deposition).

The basic FIB instrument consists of a vacuum system and chamber, an ion source, an ion optics column, a beam deflector and a sample stage (in fig. 1.1 a FIB system is schematically depicted).

The structure of the column is similar to that of a scanning electron microscope, the major difference being the use of an ion beam instead of an electron beam. The beam generated from the ion source undergoes a first refinement through the spray aperture and then is condensed in the first electrostatic lens. The upper octupole then adjusts the beam stigmatism. The ion beam energy is typically between 10 and 50 keV, with beam currents varying between 1 pA and 10 nA. Using the variable aperture mechanism, the beam current can be varied over four decades, allowing both a fine beam for high-resolution imaging on sensitive samples and a heavy beam for fast and rough milling. Blanking of the beam is accomplished by the blanking deflector and aperture, while the lower octupole is used for raster scanning the beam over the sample in a user-defined pattern. In the second electrostatic lens, the beam is focused to a fine spot, enabling a resolution in the sub 10 nm range. The multichannel plate (MCP) is used to collect secondary particles

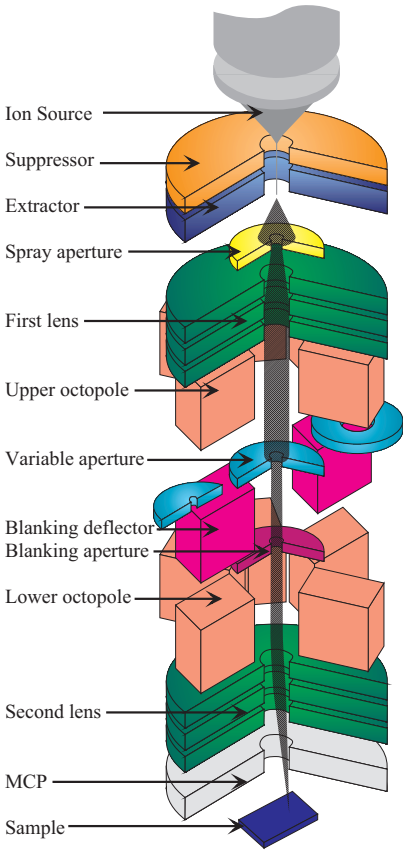

Figure 1.1: Schematic diagram of a FIB system (from [37]).

(ions and electrons) for imaging.

The more common source used in FIBs is the liquid-metal ion source (LMIS) [38, 39], whose schematic diagram is shown in fig. 1.2. The LMIS is constituted by a tungsten needle attached to a reservoir that holds the liquid metal, the most commonly used being Gallium [40]. Ga^+ ion emission occurs via a two step process: (i) the heated Ga flows and wets the tungsten needle having a tip radius of $2 \div 5$ μm; a strong electric field (10^8 V/cm) applied to the end of the wetted tip causes the liquid Ga to form a point source on the order of 2-5 nm in diameter in the shape of a "Taylor cone". The conical shape forms as a result of the electrostatic and surface tension force balance that is set up due to the applied electric field. (ii) Once force balance is achieved, the cone tip is small enough such that the extraction voltage can

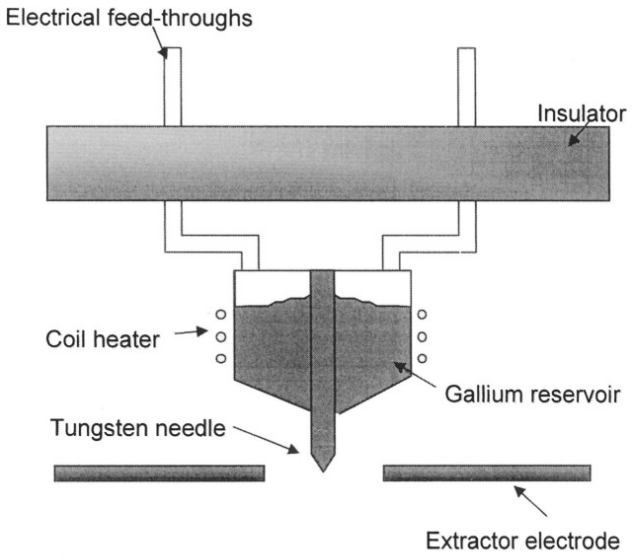

Figure 1.2: Schematic diagram of the LMIS (from [32]).

pull Ga from the W tip and efficiently ionize it by field evaporation of the metal at the end of the Taylor cone. The current density of ions that may be extracted is on the order of about 10^8 A/cm^2. A flow of Ga to the cone continuously replaces the evaporated ions.

The main advantages of this kind of ion source are the reliability and steadiness of the ion beams produced, the workability of its implementation and the very high brightness, mostly due to its small source size, that allows the production of focused ion beams with spot sizes in the sub-10 nm range, while maintaining currents in the range of 1-10 pA.

However, in spite of its very good features, the LMIS FIB source performances are limited by several factors. One is the intrinsic low flexibility in terms of the ionic species that can be implemented in an LMIS, due to the need of wetting the tungsten tip, that has restricted the choice to Ga, Ag, Al, Be and Cs [5]. The other huge limitation on the source performances is represented by the chromatic aberration in the focusing optics that form the focused ion beam, limiting the achievable resolution. The cause of the chromatic aberration is the large initial energy spread, more than several eV, of the Ga^+ ions. This spread is due to space charge effects occurring in the very small emission area on the surface of the emitter [38]. Of course, the

empasse lies in the fact that reducing the chromatic aberrations requires to reduce the space-charge effect, forcing a trade-off between beam current and resolution.

Trying to solve this problem, two main kind of ion sources, completely different from LMIS, have been proposed in the past: gas phase [41], and plasma [42]. These alternative designs offer only partial solutions to the problems affecting the LMIS, since they introduce other disadvantages. In fact, gas phase sources have narrower energy spreads, on the order of 1 eV, but the current is significantly less and they are more complicate to operate [43]. Also plasma sources are affected by a brightness that is orders of magnitude less than the LMIS [44].

More recently, a new kind of ion source, called UCIS (Ultra Cold Ion Source [45, 46]), has been proposed. This source is based on the ionization of laser cooled atoms and promises to offer substantial improvements in the FIB technology. For example, the laser cooling techniques can provide a broader choice of elements to be ionized, thus mitigating the first of the above mentioned problems affecting the LMIS.

At present, a lot of efforts are made in trying to integrate laser cooling and FIB technology: the first result of these efforts is shown in fig. 1.3, representing the surface of a microchannel plate imaged exploiting an UCIS Cr ion beam.

The UCIS tries to circumvent the performance limitations affecting the LMIS following an alternative route. For example, it has been demonstrated that the UCIS has a brightness comparable to that of the LMIS [47]. However, since the brightness of an ion beam is inversely proportional to the source size and to the initial angular spread of the beam itself, the LMIS attains very high brightness by reducing the source size. On the contrary, the UCIS high brightness is due to the reduced angular spread of the ions, as direct consequence of the very low temperature of the original atoms.

Due to the exploitation of laser cooling, the UCIS performances are not only comparable but, in several aspects, even better than those of the LMIS. For example, because of the extremely low temperatures of the cold ions, the longitudinal energy spread of an UCIS ion beam is dominated by the

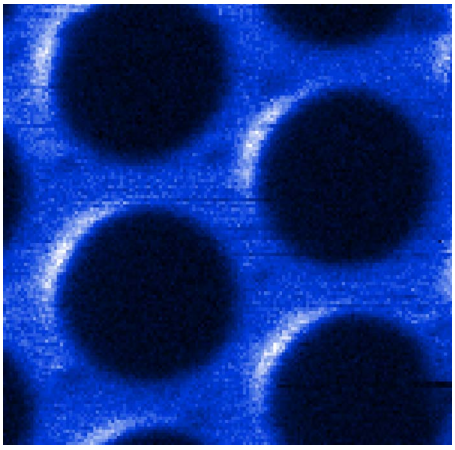

Figure 1.3: Secondary electron image, taken using a laser-cooled Cr FIB. The target is a piece of a microchannel plate with 10 μm pores, which are clearly resolved. The Cr ion beam energy is 2 keV and the one standard deviation beam radius is 250 nm. This image is 300 $\times$ 300 pixels and took 90 s to acquire.

extraction potential gradient across the finite source size. With typical source sizes, widths of 0.1 eV [48] are possible, reducing the effects of chromatic aberrations and making design of the ion optics less demanding. Another advantage of the low longitudinal energy spread lies in the possibility to focus the beam on the nanometer scale at energies much lower than the conventional ion sources. This opens possibilities for much better control over the implantation depth of ions and the size of the damage regions associated with ion milling. The control can be further increased with the possibility, on experimentally practicable times, of controlling by means of time-dependent electric fields [49–51] both the longitudinal and the transverse ion phase-space distribution, leading to an additional reduction of the chromatic aberrations effects.

In this thesis we have photoionized the pre-existing laser cooled atomic beam in order to produce an ion beam. While the working principles of our ion source are similar to those of the configurations investigated by other research groups, our approach owns a few distinctive features.

In fact, the most common scheme in this context is based on the photoion-

ization of a cold atomic cloud obtained in a MOT [49, 52] and the subsequent extraction and acceleration of the produced charges through suitable electric fields. In some sense, such a scheme can be seen as a variant of LMIS, since ions have to be extracted out of the ionization region (the cold atomic cloud for the UCIS, the apex of the Taylor cone for the LMIS). On the contrary, in our configuration the ionizing radiation acts on an already formed particle beam (that is, a sample with a net and well-defined longitudinal velocity).

This kind of source, at least in principle, could offer several advantages. From a practical point of view, for example, the ion optics could be simplified, since there is no more the need to extract the ions from a tiny region. Moreover, if no further electric field is applied, the availability of an ultra low (longitudinal) energy ion source could allow to probe unexplored operative regimes in critical applications, such as the ultra low energy implantation in the fabrication of memories based on silicon nanocrystals [53]. Finally, the overall design of our laser cooled atomic beam, originally conceived for technological applications, offers to the system an inherent technical compatibility with industrial-oriented applications. For instance, a single laser beam is used for the atom funneling through the pyramid hole, a relatively compact and scalable vacuum chamber is used, a very simple ionization scheme has been implemented.

Such a set of reasons gave us the main motivations to accomplish the work described in this thesis.

Chapter 2

Laser cooling of Cesium atoms

Fundamental tool of the research presented in this thesis is the application of techniques of laser manipulation to produce a Cesium atomic beam with sub-thermal kinetic energy. This chapter starts describing, in section 2.1 several properties of the Cesium atom, that will be useful in the following, focusing in particular on the hyperfine structure of its energy levels. Then, in section 2.2 the fundamental properties of the interaction between radiation and ideal two-level atoms are introduced. Although naive, this model is useful to explain the origin of the radiation pressure force and the working principle of the Doppler cooling and the magneto-optical trapping, explained in section 2.2.2 and in section 2.2.3, respectively.

2.1 The Cesium atom

Due to their electronic properties, the alkalis are the most common species in the experiments on cooling and trapping of neutral atoms. The frequency of excitation from the ground to the first excited state falls in the visible or near infrared range, where it is relatively simple to generate suitable laser radiation. Moreover, since the optical transitions involve a single electron, they are relatively simple to describe, provided that the hyperfine structure is properly taken into account. This aspect is very important in designing laser manipulation schemes.

In a two-level model approach, for example, "closed" transitions can be found where, in principle, one can manipulate an entire atomic sample without losses due to transitions towards non interacting states.

In the following we will highlight the limitations of this model and the necessity of a more complicated and realistic one. In this section we provide a brief description of the atomic properties of Cesium that will be needed in the following discussion.

2.1.1 Hyperfine structure

The ^{133}Cs (of which in table 2.1 we list some properties useful in the following) is the only stable isotope of Cesium; in the ground state the total electronic angular momentum (J) is 1/2, therefore this state is represented as $6^2S_{1/2}$; in the excited state it can be $J = 1/2$ or $J = 3/2$, and the two excited states are represented respectively as $6^2P_{1/2}$ and $6^2P_{3/2}$. The transitions between the ground and first excited state, components of a fine-structure doublet, are called D_1 line ($6^2S_{1/2} \rightarrow 6^2P_{1/2}$) and D_2 line ($6^2S_{1/2} \rightarrow 6^2P_{3/2}$). Since the nuclear angular momentum (I) is 7/2, there is an hyperfine structure (fig. 2.1) resulting from the coupling of the total electronic angular momentum $\mathbf{J}$ with the total nuclear angular momentum $\mathbf{I}$; the atomic total angular momentum $\mathbf{F}$ is then $\mathbf{F} = \mathbf{J} + \mathbf{I}$. In the ground state ($J = 1/2$, $I = 7/2$) it is $3 \leq F \leq 4$; in the excited state of the D_2 line ($J = 3/2$, $I = 7/2$) it is $2 \leq F \leq 5$, while in the excited state of the D_1 line ($J = 1/2$, $I = 7/2$) it is $3 \leq F \leq 4$.

2.1.2 Zeeman effect and hyperfine levels

An atom with total angular momentum F has $2F + 1$ Zeeman sublevels ($m_F = -F, \ldots, F$, with m_F projection of F on the quantization axis) that, in the absence of magnetic field, are degenerate. On the contrary, the presence of a magnetic field $\mathbf{B}$ removes this degeneracy (Zeeman effect) as shown in fig. 2.2. If the magnetic interaction is very small with respect to the hyperfine interaction[1], so that F is still a good quantum number [55], the state $|F,\ m_F\rangle$

[1]This condition is very well satisfied in typical magneto-optical trap conditions.

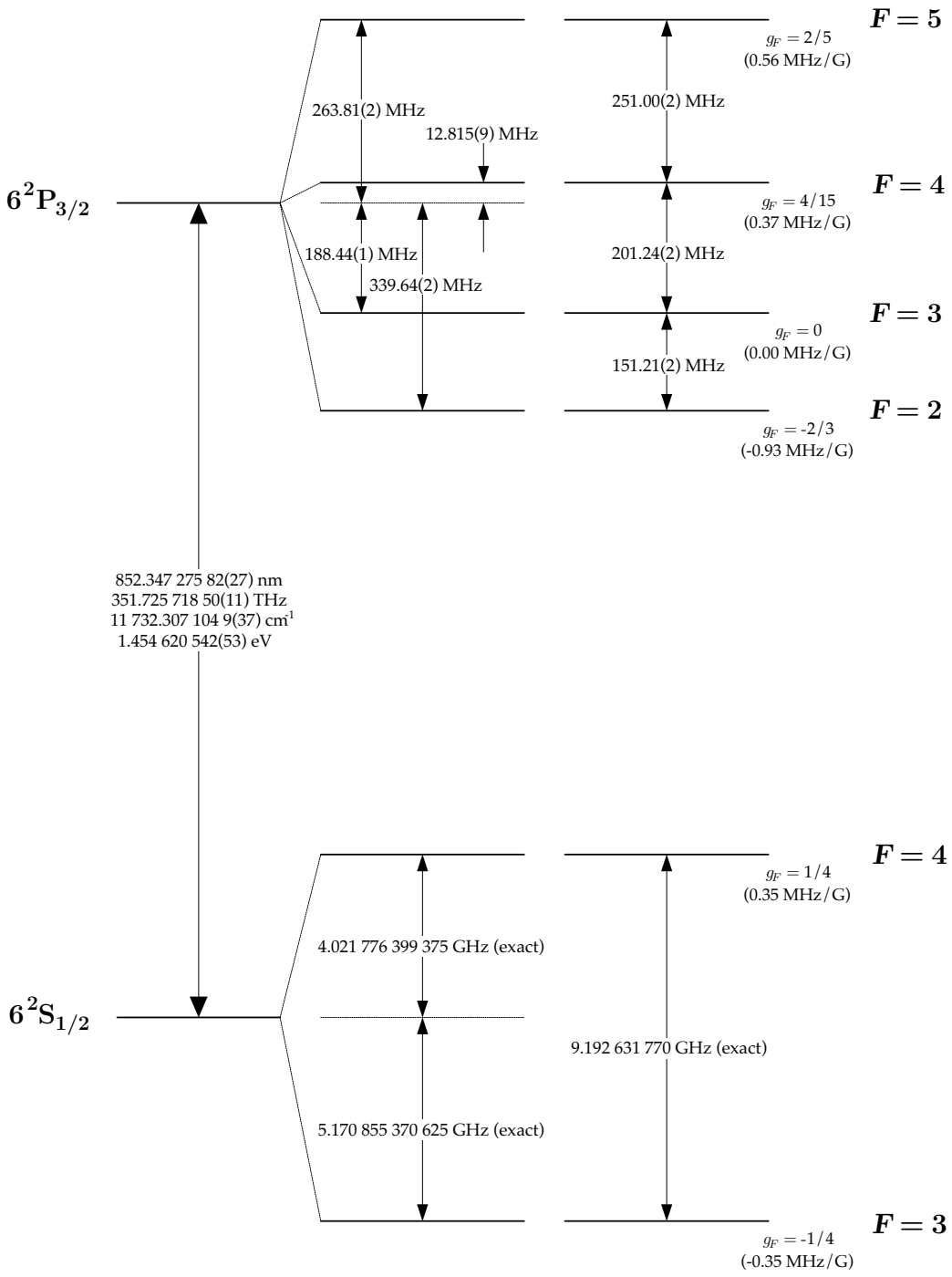

Figure 2.1: Hyperfine structure of the D_2 transition in Cs (from [54]). The frequency separations of the hyperfine energy levels and the g_F factors (eq. (2.2)) are also reported.

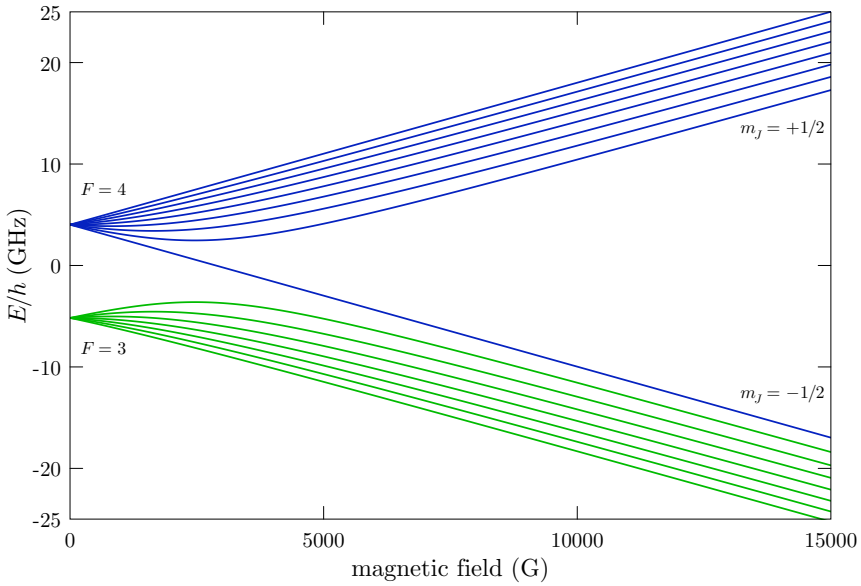

(a)

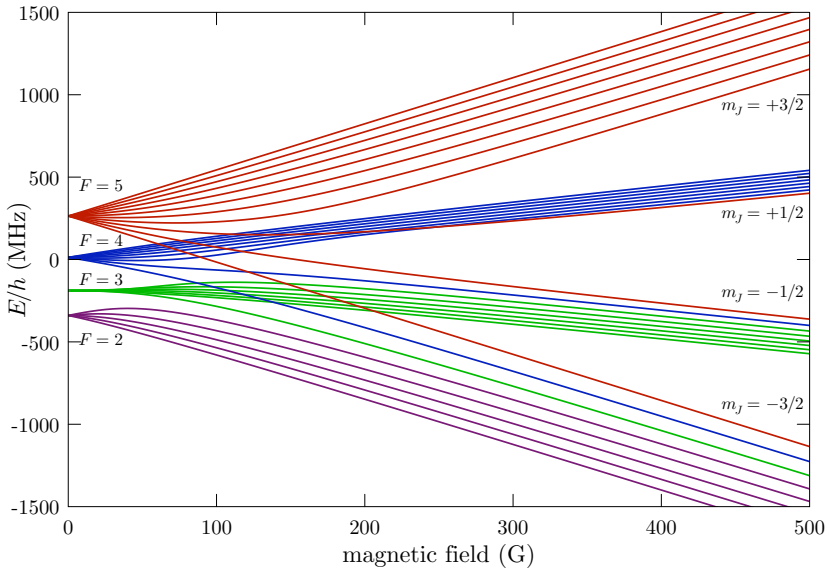

(b)

Figure 2.2: Hyperfine structure of (a) the ground ($6^2S_{1/2}$) and (b) the excited ($6^2P_{3/2}$ states of the D_2 lines of Cesium in an external magnetic field.)

Atomic mass	M	$2.206 \cdot 10^{-25}$ kg
D_2 natural linewidth (FWHM)	Γ	$2\pi \cdot 5.234$ MHz
$^2P_{3/2}$ average lifetime	τ	30.405 ns
D_2 wavelength	λ	852.35 nm
D_2 saturation intensity	$I_{sat} = \frac{\hbar\Gamma\omega_{eg}^3}{12\pi c^2}$	1.1 mW/cm^2
Recoil velocity	$v_{rec} = \frac{\hbar k}{M}$	3.5 mm/s
Recoil temperature	$T_{rec} = \frac{\hbar^2 k^2}{M k_B}$	198.34 nK
Doppler temperature	$T_D = \frac{\hbar\Gamma}{2k_B}$	125.61 μK
Maximum radiation pressure	$F_{pr}^{max} = \frac{\hbar k\Gamma}{2}$	$1.28 \cdot 10^{-20}$ N

Table 2.1: Cs numerical data.

undergoes a linear energy shift:

$$\Delta E_{m_F} = g_F \mu_B m_F B \tag{2.1}$$

where μ_B is the Bohr magneton, g_F is given by:

$$g_F = g_J \frac{F(F+1) + J(J+1) - I(I+1)}{2F(F+1)} \tag{2.2}$$

with g_J Landè factor:

$$g_J = 1 + \frac{J(J+1) + S(S+1) - L(L+1)}{2J(J+1)}. \tag{2.3}$$

where L and S are, respectively, the electronic orbital and spin angular momenta.

As we will discuss in section 2.2.3, the mechanical action exerted by the light on the atoms and the Zeeman effect obtained in a spatially-varying magnetic field are the basic working principles of the magneto-optical trap.

2.2 Atom-radiation interaction in the two level approximation: laser cooling and trapping

The interaction between resonant radiation and an ideal two-level atom is a well known subject [56] that here will be only summarized in its main points. In section 2.2.1 we introduce the Rabi frequency and the saturation intensity, quantities used in section 2.2.2 to derive the expression of the radiation pressure force exerted by resonant radiation on the atoms. Then, we show how the radiation pressure force is used in Doppler cooling. Finally, section 2.2.3 illustrates the operation of the magneto-optical trap (MOT), detailing a particular implementation, called pyramidal MOT (PMOT), that is the atomic source of our experiment.

2.2.1 Rabi frequency and saturation intensity in the two-level model

Let us consider an atomic system with two levels $|g\rangle$ and $|e\rangle$, with an energy separation $\hbar\omega_{eg}$. When it interacts with a monochromatic electromagnetic field $\mathbf{E}(\mathbf{r},t) = \mathbf{E}_0(\mathbf{r})\cos(\omega t)$, in a perturbative approach the interaction Hamiltonian is dominated by the electric dipole term:

$$H^{int} = -\mathbf{E}(\mathbf{r},t)\cdot\mathbf{d} = \hbar\Omega(\mathbf{r})\cos(\omega t) \tag{2.4}$$

where $\mathbf{E}$ is the external electric field, $\mathbf{r}$ and $\mathbf{d}$ the position and the dipole moment of the atom and where we define the complex Rabi frequency:

$$\Omega(\mathbf{r}) = \Omega_0(\mathbf{r})e^{i\phi(\mathbf{r})} = -\frac{\langle e|\mathbf{E_0}(\mathbf{r})\cdot\mathbf{d}|g\rangle}{\hbar} \tag{2.5}$$

whose phase is given by $\phi(\mathbf{r})$ while its modulus is related to the intensity $I(\mathbf{r})$ of the field by the expression:

$$\Omega_0(\mathbf{r}) = \Gamma\sqrt{\frac{I(\mathbf{r})}{2I_{sat}}} \tag{2.6}$$

where Γ represents the natural linewidth and

$$I_{sat} = \frac{\hbar\Gamma\omega_{eg}^3}{12\pi c^2} \tag{2.7}$$

the corresponding saturation intensity.

2.2.2 The radiation pressure force and Doppler cooling of a two-level atom

In the eq. (2.4) we introduced the interaction term between an ideal two-level atom and a coherent, monochromatic radiation field. In absence of spontaneous emission, the total Hamiltonian of the atom-radiation system is the superposition of three terms:

$$H^{tot} = H^{atom} + H^{rad} + H^{int} \tag{2.8}$$

where H^{atom} is the sum of the atomic kinetic and internal energy terms:

$$H^{atom} = \frac{\mathbf{p}^2}{2M} + \frac{\hbar\omega_{eg}}{2}(|e\rangle\langle e| - |g\rangle\langle g|) \tag{2.9}$$

where $\mathbf{p}$ is the atomic momentum operator and M the atomic mass. The operator H_{rad} is the hamiltonian of a single-mode quantized radiation field:

$$H^{rad} = \hbar\omega a^\dagger a \tag{2.10}$$

with $a^\dagger$ and a creation and destruction operators for the photon of energy $\hbar\omega$, while the operator H_{int} (coincident with the expression of eq. (2.4)), can be

rewritten as:

$$H^{int} = \frac{\hbar\Omega(\mathbf{r})}{2}(|e\rangle\langle g|e^{-i\omega t} + |g\rangle\langle e|e^{+i\omega t}) \tag{2.11}$$

The evolution of a two-level system interacting with the monochromatic field of eq. (2.4) is regulated by the temporal evolution of the density matrix ρ. This, in turn, is found solving the master equation:

$$\frac{d\rho}{dt} = \frac{i}{\hbar}\left[\rho;\ H^{tot}\right] - \gamma\rho \tag{2.12}$$

where $\gamma\rho$ describes phenomenologically the decay of the diagonal (populations) and off-diagonal (coherences) density matrix elements. Exploiting the hermiticity of the density matrix and the rotating wave approximation (prescribing the replacement of all the off-diagonal elements with the slowly varying variables $\sigma_{ge} = \rho_{ge}e^{-i\omega t}$), from eq. (2.12) the optical Bloch equations (OBE) can be obtained:

$$\frac{d\rho_{gg}}{dt} = -\Omega\ \mathrm{Im}(\sigma_{ge}) + \Gamma\rho_{ee} \tag{2.13}$$

$$\frac{d\rho_{ee}}{dt} = \Omega\ \mathrm{Im}(\sigma_{ge}) - \Gamma\rho_{ee} \tag{2.14}$$

$$\frac{d\sigma_{ge}}{dt} = i(\omega_{ge} - \omega)\sigma_{ge} - i\frac{\Omega}{2}(\rho_{ee} - \rho_{gg}) - \frac{\Gamma}{2}\sigma_{ge} \tag{2.15}$$

where ρ_{ee} and ρ_{gg} represent the populations of the excited and ground states. The stationary solutions of the OBE determine the populations involved in the transition. It is trivial to see that, in stationary conditions, the population ρ_{ee} of the excited state is given by:

$$\rho_{ee} = \frac{|\Omega|^2}{\Gamma^2 + 2|\Omega|^2 + 4\delta^2} \tag{2.16}$$

where $\delta = \omega - \omega_{eg}$ is the detuning of the monochromatic field with respect to the atomic resonance. Accordingly, the total number of spontaneously emitted photons (per unit time) $\Gamma_{scatter}$ is given by:

$$\Gamma_{scatter} = \Gamma\rho_{ee} = \frac{\Gamma}{2}\frac{2|\Omega|^2}{\Gamma^2 + 2|\Omega|^2 + 4\delta^2}. \tag{2.17}$$

Now, the photons absorbed transfer momentum from the field to the atoms; on the contrary, the spontaneously emitted photons do not have a net average effect on the atomic motion, since they make the atoms recoil in random directions. From this it follows that, in a sequence of many absorption-spontaneous emission cycles, an atom undergoes a non-zero average variation of its momentum, due to the photons absorbed. The absolute value of the resulting force, called radiation pressure, can be written as:

$$F_{pr} = \hbar k \Gamma_{scatter} = \frac{\hbar k \Gamma}{2} \frac{2|\Omega|^2}{\Gamma^2 + 2|\Omega|^2 + 4\delta^2}. \tag{2.18}$$

where k is the wavevector of the radiation field. The dependence of eq. (2.18) on Ω and δ is shown in fig. 2.3. At high radiation intensities we note a saturation of the force at the maximum value $\hbar k\Gamma/2$ (see table 2.1). In this situation, the acceleration $a_{max} = F_{pr}^{max}/M$ of an atom can reach values of several thousands g.

The radiation pressure force of eq. (2.18) is the basis of the laser cooling capabilities to manipulate and control the atomic motion [57, 58]. Through interaction with the radiation it is possible to reduce considerably the average value and the width of the velocity distribution, and therefore the temperature, of an atomic sample. For an atom in motion with velocity $\mathbf{v}$, the Doppler effect detunes an electromagnetic wave (of wavevector $\mathbf{k}$ and detuning δ) of the quantity $\delta(\mathbf{v}) = \delta - \mathbf{k} \cdot \mathbf{v}$. Because of this velocity dependent detuning, the radiation pressure in eq. (2.18) depends on the velocity of the atom [58], too. As a consequence, an atom interacting with two counterpropagating laser beams of low intensity and with the same frequency (configuration called optical molasses [59]) is subjected to a force:

$$F = F(\delta + \mathbf{k} \cdot \mathbf{v}) - F(\delta - \mathbf{k} \cdot \mathbf{v}) \simeq \frac{16\hbar k^2 \delta \Omega_0^2}{\Gamma^3 \left(1 + \left(\frac{2\delta}{\Gamma}\right)^2 + \frac{2\Omega_0^2}{\Gamma^2}\right)^2} \tag{2.19}$$

with Ω_0 defined in eq. (2.6) where, for simplicity, the dependence on the atomic position $\mathbf{r}$ has been dropped. Equation (2.19) has been obtained by a perturbative approximation of the sum of the radiation pressure forces

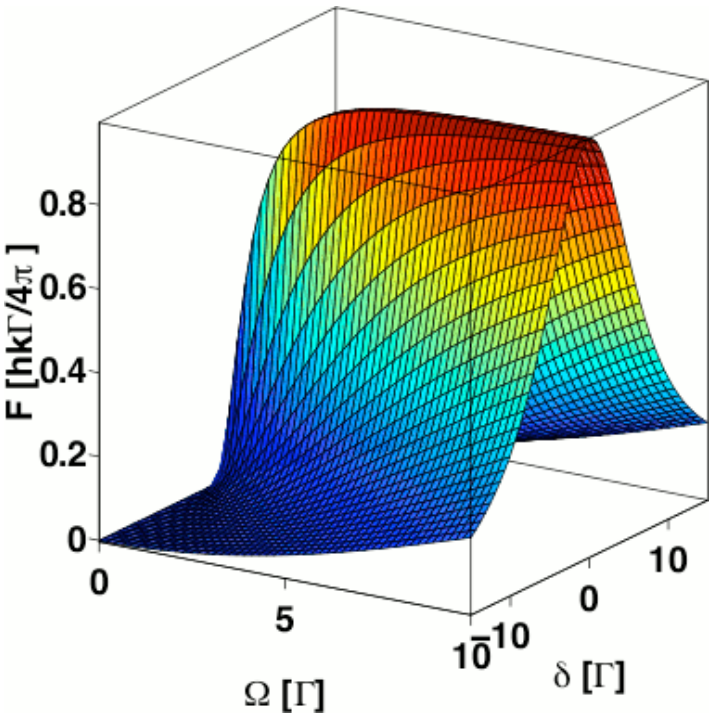

Figure 2.3: Radiation pressure force in units of $\hbar k\Gamma/2$ as function of the Rabi frequency and the laser detuning.

exerted on the atom by the two beams, in the hypothesis of low intensity (the interference terms between the stimulated transitions probability amplitudes are neglected) and low atomic velocity (it is assumed $|\mathbf{k}\cdot\mathbf{v}| \ll \Gamma$). In case of red detuning ($\delta < 0$) the atom is subjected to a viscous force, characterized by the viscosity coefficient:

$$\gamma = -\frac{16\hbar k^2 \delta \Omega_0^2}{\Gamma^3 \left(1 + \left(\frac{2\delta}{\Gamma}\right)^2 + \frac{2\Omega_0^2}{\Gamma^2}\right)^2}. \tag{2.20}$$

The acceleration of a Cs atom in an optical molasses is shown in fig. 2.4, as a function of its velocity, for different Rabi frequency and detuning values.

The optical molasses can be realized in three dimensions, with three couples of laser beams propagating in the orthogonal directions; in this configuration the atomic motion can then be cooled in all directions.

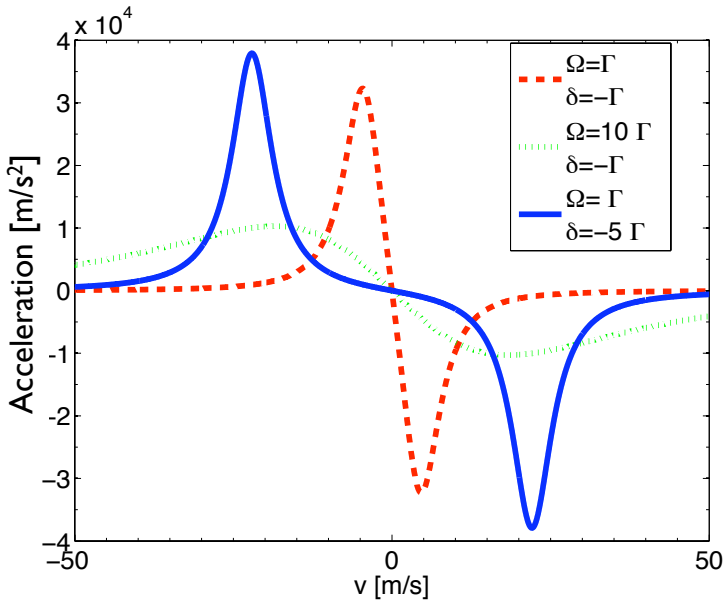

Figure 2.4: Acceleration computed for a Cesium atom subjected to the radiation pressure force in a one dimensional optical molasses.

We remark that, if it was not for some other mechanism coming into play, the temperature of an atomic sample in an optical molasses would tend rapidly to zero, a clearly not physical situation that would violate the Heisenberg

principle. Actually, the heating mechanism related to the random recoil in the momentum space due to the spontaneous emissions must be considered. The scattered photons give to the atoms a zero average velocity, but a root mean square velocity different from zero, in this way contributing to their heating. This increases the kinetic energy related to the motion in random directions, limiting the minimum temperature reachable by the Doppler cooling process. It is possible to show [60] that, far from saturation conditions ($I \ll I_{sat}$), the minimum temperature reachable in the Doppler cooling is:

$$T_D = \frac{\hbar\Gamma}{2k_B} \tag{2.21}$$

where k_B is the Boltzmann constant. The Doppler limit for Cesium, reported in table 2.1, is about 126 μK.

2.2.3 Magneto-optical trap

In a magneto optical trap (MOT) to the red detuned laser beams, confining the atoms in the velocity space, a not homogeneous magnetic field is added, that traps them in the real space, too. To explain the basic mechanism, let us consider an atom with ground state $F = 0$ and excited state $F = 1$ [61]. In the presence of a magnetic field linearly non-homogeneous (for example $B(x) \approx bx$), the Zeeman sublevels are no longer degenerate and their energy shift (eq. (2.1)) becomes dependent (at the first perturbative order) on the position as:

$$\Delta E_B(x) \simeq \mu_B m_F g_F B(x) = \mu_B m_F g_F b x \tag{2.22}$$

If the atom is located at $x > 0$ (assuming $b > 0$ and $g_F > 0$), the excited state $M_e = 1$ increases its energy away from the origin (see fig. 2.5), like the energy of an atom in the state $M_e = -1$ decreases; in this way the magnetic field is such that the transition with $\Delta M = -1$ is "more resonant". If the polarization of the laser beam impinging towards $-\hat{x}$ is σ^-, while that of the incident beam propagating to $+\hat{x}$ is σ^+, then more photons are scattered from the σ^- beam and the atom is pushed towards the origin. In the origin itself the force acting on a stationary atom is zero: in fact there is not the

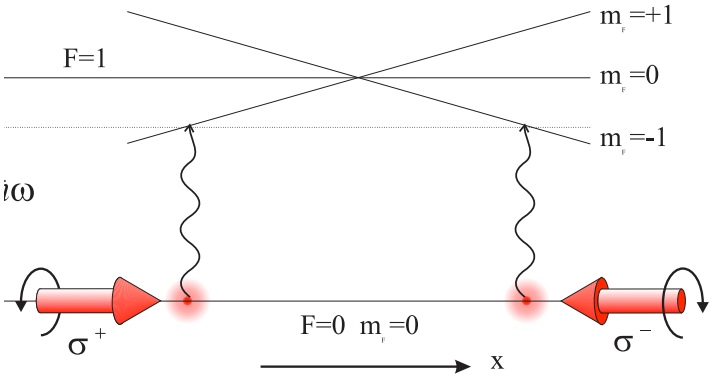

Figure 2.5: Schematic diagram of a one dimensional MOT.

effect of the magnetic field ($B(0) = 0$) and the detunings are the same for both the transitions, so that the total radiation pressure force vanishes.

In the three-dimensional case, the magnetic field necessary to the trapping can be generated by two coils in anti-Helmholtz configuration. Assuming the axis of the coils is along the z axis, the field near the origin can be written as:

$$\mathbf{B} \simeq \frac{b}{2}(-x,\ -y,\ 2z) \tag{2.23}$$

Furthermore, in the three orthogonal directions, three pairs of laser beams in configurations $\sigma^+ - \sigma^-$ counter-propagate. The atoms feel the total force:

$$F = \mathbf{F}_\pm = \pm\frac{\hbar\mathbf{k}\Gamma}{2}\frac{2|\Omega|^2}{\Gamma^2 + 2|\Omega|^2 + 4(\delta \mp \mathbf{k}\cdot\mathbf{v} \pm \mu_{eff}B/\hbar)^2} \tag{2.24}$$

where $\pm$ refer to the pairs of counterpropagating laser beams and $\mu_{eff} = (g_e M_e - g_g M_g)\mu_B$ is the effective magnetic moment of the transition. In fig. 2.6 the trends of the absolute value of $\mathbf{F}$ as a function of the atomic velocity are plotted, computed from eq. (2.24) for several combinations of intensity and detuning of the laser beams and magnetic field gradient.

When Doppler and Zeeman shifts are both small with respect to δ, the expression of the force in eq. (2.24) approximates to a linear dependence on the position and velocity of the atom:

$$\mathbf{F} = -\gamma\mathbf{v} - \chi\mathbf{x} \tag{2.25}$$

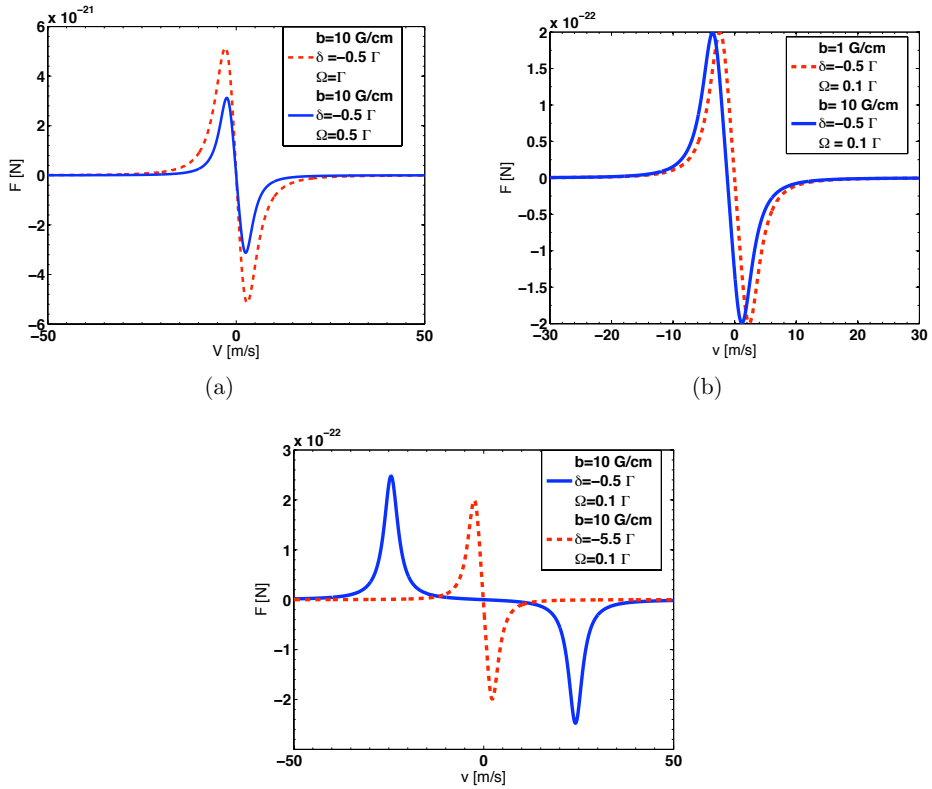

Figure 2.6: Force acting on an atom in a 1D MOT as a function of its velocity along the $\hat{x}$ axis of fig. 2.5.

where γ has been defined in eq. (2.20) and the elastic constant χ is given by:

$$\chi = \frac{\mu_{eff} b}{\hbar k} \gamma \tag{2.26}$$

Therefore, for small oscillations around the origin, an atom in a MOT behaves like a damped harmonic oscillator, with the motion equation: $\ddot{\mathbf{x}} + 2\beta\dot{\mathbf{x}} + \omega_0^2 \mathbf{x} = 0$ where $\mathbf{x}$ is the atomic position, $\omega_0^2 = \chi/M$ and $\beta = \gamma/2M$. The damping rate is given by $\gamma_{MOT} = \gamma/M$ while the frequency oscillation is $\omega_{MOT} = \sqrt{\chi/M}$. With a typical magnetic field gradient of 10 G/cm, the frequency oscillation is several kHz, while the damping rate is some hundreds kHz; therefore the atomic motion is over-damped.

Pyramidal magneto-optical trap

Although a conventional MOT, as discussed above, is realized with six laser beams counterpropagating along the three principal directions, several different geometries have been implemented, like the axicon [62] and the pyramid [63], used as source of cold atoms in our experiment [64].

In the PMOT configuration (fig. 2.7) a single laser beam circularly polarized illuminates the internal reflective walls of an hollow pyramid. In the directions orthogonal to the pyramid axis, each reflection produces two counterpropagating laser beams with opposite circular polarizations. In the axial direction, the double reflections on the inner surfaces generate counterpropagating laser beams only out of the axis, due to the presence of a hole on the apex of the pyramid. Thus, within the pyramid there are cooling forces in any point, except along a central parallelepiped-shaped region, where the apical hole prevents the light to be retroreflected.

The missing retroreflection makes the formation of a "static" MOT on the axis impossible. Therefore, the pyramidal MOT works as an atomic funnel. In conclusion, we anticipate that in the apparatus there are additional compensation coils that allow to shift the zero of the magnetic field outside the axis, where a static MOT can be formed for diagnostic purposes.

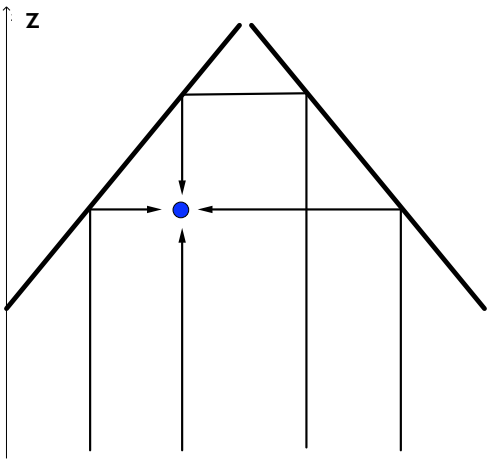

Figure 2.7: Scheme of the reflections of the laser beams inside the pyramid.

Chapter 3

Multilevel atom-radiation interaction

Since the capabilities of the two-level model, illustrated in chapter 2, do not extend much further the simple Doppler cooling mechanism, in this chapter we treat the interaction between radiation and a more realistic multilevel model of the Cesium atom. Several aspects of the atom-radiation interaction, like the optical pumping phenomena among Zeeman and hyperfine levels neglected in the two-level model but necessary for the correct interpretation of the experimental findings, are reviewed. This chapter is organized in two sections, whose subjects have in common that they both heavily rely on optical pumping.

Section 3.1 starts defining the relative line intensities (section 3.1.1), of which in section 7.2.2 we will report the experimental values for the three hyperfine transitions: $6^2S_{1/2}F_g = 4 \rightarrow 6^2P_{3/2}F_e = 3$, $6^2S_{1/2}F_g = 4 \rightarrow 6^2P_{3/2}F_e = 4$ and $6^2S_{1/2}F_g = 4 \rightarrow 6^2P_{3/2}F_e = 5$ to which we will refer simply as T43, T44 and T45, respectively. We will show in the following that these quantities are heavily affected by the optical pumping which, in turn, strongly depends on the length of the interaction time between atoms and radiation. In section 3.1.2 we detail the geometrical configuration of our two-photon, two-color ionization scheme, anticipating several atomic beam properties (detailed in chapter 6) that we will need in order to define an "average" interaction

time. In section 3.1.3 we focus on the expression of the Rabi frequency in a multilevel system; then, in section 3.1.4, the concepts of transition strengths and transition strength ratios are presented. In section 3.1.5 we will show how the two-level model fails in reproducing correctly the experimental relative line intensities, because of hyperfine and Zeeman optical pumping phenomena explained in section 3.1.6. In section 3.1.7 we describe the simulation, based on the numerical solution of the multilevel OBE, implemented to reproduce numerically the effects of those phenomena on the experimental data. We remark that the use of a model based on the atomic coherences is justified by the ionization rate that, in our configuration, is sufficiently low (see section 4.3) to ensure that the description of the atomic states is not heavily modified with respect to situations in which the ionization laser is not present. A detailed comparison between numerical and experimental relative line intensities will be accomplished in section 7.2.2. To conclude, in section 3.2 we briefly summarize the sub-Doppler cooling mechanisms, that can be interpreted on the basis of the optical pumping phenomena introduced in the previous sections.

3.1 Optical pumping in the multilevel Cs atom

In this section we focus on the interaction between polarized radiation and multilevel Cs atoms, modeling the phenomena behind the experimental data that will be presented in section 7.2.2.

3.1.1 Relative line intensities

We define the line intensity $\mathcal{I}$ of a transition and, consequently, the relative line intensity $\mathcal{R}$ as follows. If we consider the fluorescence emission of an ideal two-level system, a reasonable definition of line intensity is the maximum height of the spectral line[1]. Accordingly, from eq. (2.17), the line intensity for

[1]The maximum height is considered as difference between the peak of the spectral line and zero, defined as the fluorescence yield when the excitation radiation is far detuned from the atomic resonance.

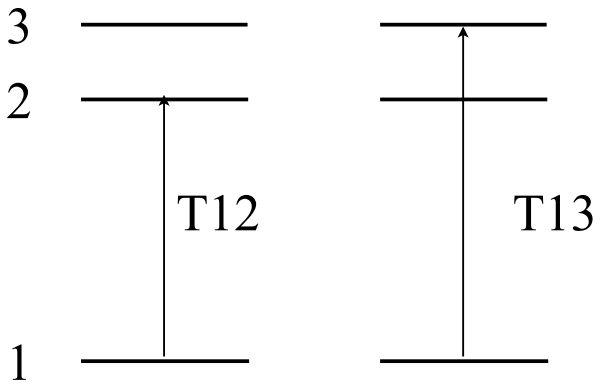

Figure 3.1: Ideal three level system.

a two level system is proportional to the excited state population in resonance conditions and it reads:

$$\mathcal{I} = \mathcal{I}_0 \rho_{ee}(\delta = 0) = \mathcal{I}_0 \frac{\Omega^2}{\Gamma^2 + 2\Omega^2} \tag{3.1}$$

where $\mathcal{I}_0$ is a parameter taking into account several factors (fluorescence collection efficiency, spectral response of the apparatus, etc). In a multilevel atom, analyzed in the following, the line intensity will be again considered to be proportional to the relative excited state population, even if its explicit expression will not coincide anymore with eq. (3.1).

For example, we can use eq. (3.1) to obtain the relative line intensities in a three level system. We consider the two transitions T12 and T13 connecting the levels $|1\rangle \rightarrow |2\rangle$ and $|1\rangle \rightarrow |3\rangle$ of the ideal closed three level system depicted in fig. 3.1. From eq. (3.1) the line intensities are then:

$$\mathcal{I}_{12} = \mathcal{I}_0 \frac{\Omega_{12}^2}{\Gamma^2 + 2\Omega_{12}^2} \tag{3.2}$$

$$\mathcal{I}_{13} = \mathcal{I}_0 \frac{\Omega_{13}^2}{\Gamma^2 + 2\Omega_{13}^2} \tag{3.3}$$

where Ω_{ij} is the Rabi frequency for the transition Tij. Consequently, we define the relative line intensity $\mathcal{R}_{12,13}$ between the two transitions T12 and

T13:

$$\mathcal{R}_{12,13} = \frac{\mathcal{I}_{12}}{\mathcal{I}_{13}} = \frac{\Omega_{12}^2}{\Omega_{13}^2} \frac{\Gamma^2 + \Omega_{13}^2}{\Gamma^2 + \Omega_{12}^2} \tag{3.4}$$

We remark that eq. (3.4) is well suited only for an ideal three level system interacting with resonant radiation for an indefinite interaction time. Since the experimental relative line intensities reported in section 7.2.2 have been measured for real Cesium atoms interacting with resonant radiation for a finite time, we obviously expect that eq. (3.4) cannot properly describe them.

3.1.2 Details on the configuration

As already mentioned, in this section we briefly describe the geometrical configuration of the two-photon, two color ionization scheme in which the relative line intensities have been measured. The main motivation of the present discussion is given by the experimental observation that optical pumping heavily affects the data presented in section 7.2.2. On the other hand, in literature it has been demonstrated [65–67] that the optical pumping effects heavily depend on the interaction time between atoms and radiation; in turn, the interaction time is determined by the details of the geometrical configuration. As a consequence, the determination of the interaction time is not straightforward. The present discussion is intended to find an effective interaction time by means of a simple 2D simulation. We leave the discussion of the physical aspects of the photoionization process to chapter 4.

In our configuration, depicted in fig. 3.2, the Cs atoms move through two orthogonally propagating, collimated, π polarized and spatially superposed laser beams: one excites the atoms to an hyperfine sublevel of the state $6^2P_{3/2}$; the other one is responsible for the ionization of the excited atoms. In chapter 4 we will show how, in this photoionization scheme, the ionization yield is proportional to the excited state population and, thus, to the intensity of the line on which the excitation laser is tuned.

However, from fig. 3.2 we infer that the determination of an "average" interaction time is not trivial, since:

1. the transverse density distribution of the atomic beam in the $(x,\ y)$

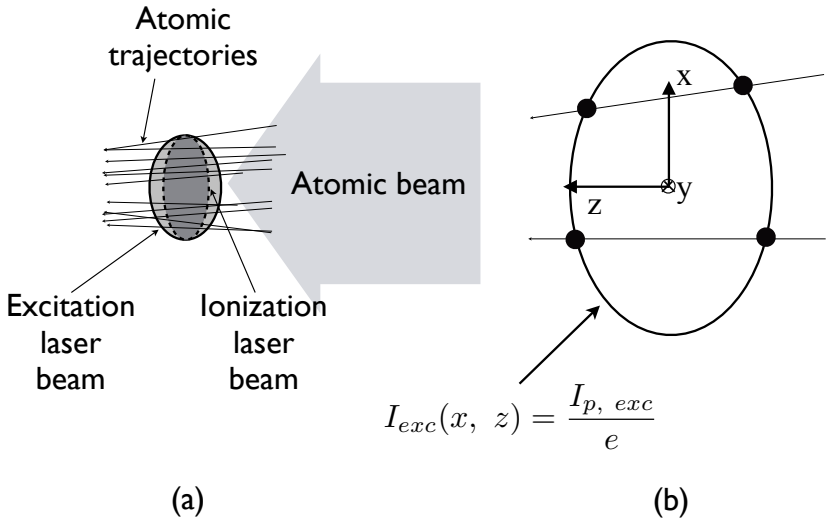

Figure 3.2: Configuration of the laser beams in the two-photon two color ionization scheme. The origin of the reference system coincides with the point of maximum radiation intensity. The excitation and ionization laser beams are propagating in the negative $\hat{x}$ direction, while the atoms move in the $\hat{z}$ direction. Several atomic trajectories are also represented, as an example.

plane is not flat, and it can be approximated with a two-dimensional Gaussian:

$$n(x,\ y) = n_0\ e^{-\frac{x^2+y^2}{w_{at}^2}} \tag{3.5}$$

where n_0 is the peak atomic density and $w_{at} = 2.4$ mm (see section 6.4)

2. the distribution of the atomic longitudinal velocities v_z is Gaussian:

$$\mathcal{N}(v_z, \sigma_z) = \mathcal{N}_0 e^{-\frac{(v_z - \langle v \rangle)^2}{\sigma_z^2}} \tag{3.6}$$

with $\langle v \rangle = 12$ m/s and $\sigma_z = 0.59$ m/s (see section 6.3). Consequently, atoms with the same trajectories but different longitudinal velocities have different interaction times with the radiation

3. the atomic beam is not perfectly collimated; the divergence angles are distributed according to:

$$\mathcal{N}(\theta, \sigma_{trasv}) = \mathcal{N}_0 e^{-\frac{\theta^2}{\sigma_{trasv}^2}} \tag{3.7}$$

with $\sigma_{trasv} = 2.97$ mrad (see section 6.2). Therefore, atoms moving with the same velocity but different divergence angles with respect to the z axis (refer to fig. 3.2 for the reference system) will interact for different time intervals with the radiation

4. the laser intensity profile is not flat-top; in particular, we ascertained experimentally that the intensity profile of the excitation laser beam is well represented by a two-dimensional Gaussian[2]:

$$I(x,\ z) = I_{p,exc}\ e^{-\frac{x^2}{w_{x,exc}^2}} e^{-\frac{z^2}{w_{z,exc}^2}} \tag{3.8}$$

where $I_{p,exc}$ is the peak excitation intensity, $w_{x,exc} = 1.6$ mm and $w_{z,exc} = 1.1$ mm.

To determine the "average" interaction time we then relied on a numerical calculation, including all the factors listed above. For a great number of atoms, we compute the trajectories[3] according to:

$$x(t) = x_0 + v_x t \tag{3.9a}$$

$$z(t) = v_z t \tag{3.9b}$$

where x_0 and v_z are extracted from the distributions in eq. (3.5) and eq. (3.6), while v_x is given by:

$$v_x = \langle v \rangle \cdot \theta \tag{3.10}$$

with θ randomly extracted from eq. (3.7). The substitution of the eq. (3.9) into eq. (3.8) allows to obtain the expression of the time dependent laser intensity in which the atoms move:

$$I_{exc}(t) = I_{p,\ exc}\ e^{-\frac{(x_0+v_x t)^2}{w_{x,\ exc}^2}} e^{-\frac{(v_z t)^2}{w_{z,\ exc}^2}} \tag{3.11}$$

[2]In eq. (3.8), $w_{x,exc}$ and $w_{z,exc}$ differ from the common definition of laser waist by a factor $\sqrt{2}$.

[3]To reduce the numerical effort necessary for a full 3D computation, we limit the calculation of the trajectories to the (x, z) plane, disregarding the motion along the y axis. We remark that we cannot exclude contributions to the results of the model due to the 2D approximation.

The parameter τ_{int}, related to the interaction time, is defined as $\tau_{int} = |t_1 - t_2|$, where t_1 and t_2 are the two roots of:

$$I_{exc}(t) = \frac{I_{p,\ exc}}{e} \tag{3.12}$$

It is clear from eq. (3.12) that we arbitrarily define τ_{int} as the time necessary to an atom to go between two points in which the intensity is $1/e$ of the peak value $I_{p,\ exc}$ (these couples of points are indicated by the black dots in fig. 3.2 (b) for several possible atomic trajectories).

In fig. 3.3 we show an histogram of the interaction times τ_{int} computed according to the above procedure on 10^5 trajectories. At first sight, the

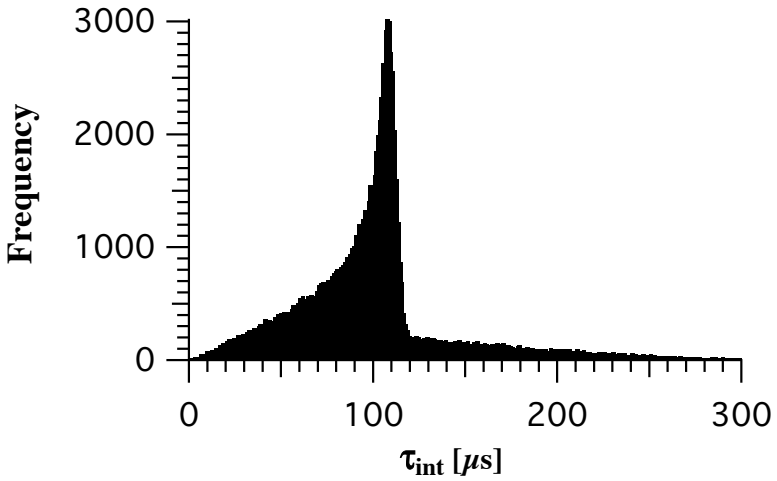

Figure 3.3: Frequency histogram of the interaction times between atoms and radiation for the configuration of fig. 3.2. The mean, mode and median of the data are 102 μs, 105 μs and 100 μs, respectively. The bin width is 1 μs.

distribution of the interaction times appears highly skewed; however, the mean, mode and median of the data are not too different:

- mean = 102 μs
- mode = 105 μs
- median = 100 μs

In the following we will use as interaction time the most probable value 105 μs, as obtained above.

We conclude this section pointing out that the skewness of the distribution of the interaction times shown in fig. 3.3 is probably due to the limited overall time interval considered in the simulation. This leads to underestimate the contribution of slow atoms (atoms having a low longitudinal velocity) entering the interaction region at early times. Tests have been made extending the overall time interval considered in the simulation: in the results, the long time tail appears more populated, but the average, median and most probable value are practically unchanged.

3.1.3 Rabi frequency, saturation intensity and selection rules in the multilevel model

The expressions of the Rabi frequency in eq. (2.5) and eq. (2.6) are suited only for a two-level system, while for a real multilevel system it is necessary to generalize their expression in order to take into account the Zeeman structure (shown in fig. 3.4) of the energy levels involved in the transitions. In section 3.1.6 we will demonstrate that the multiplicity of the Zeeman sublevels has to be properly taken into account, in order to interpret correctly the experimental data. Remembering eq. (3.12), the Rabi frequency between two Zeeman states $|F_g,\ m_g\rangle$ and $|F_e,\ m_e\rangle$ can be written as:

$$\Omega_{ge}(t) = \frac{E_0}{\hbar} \exp\left(-\frac{t^2}{2\tau_{int}^2}\right) \langle F_g,\ m_g | e r_q | F_e,\ m_e \rangle. \tag{3.13}$$

where F and m_F are the atomic total angular momentum modulus and m_F its projection onto the quantization axis (see section 2.1.1) and q is the polarization of the light. To write the eq. (3.13) we exploited eq. (3.11), introducing in the time-dependent radiation intensity the parameter τ_{int} determined in section 3.1.2, so that:

$$I_{exc}(t) = I_{p,\ exc}\ e^{-\frac{t^2}{\tau_{int}^2}}. \tag{3.14}$$

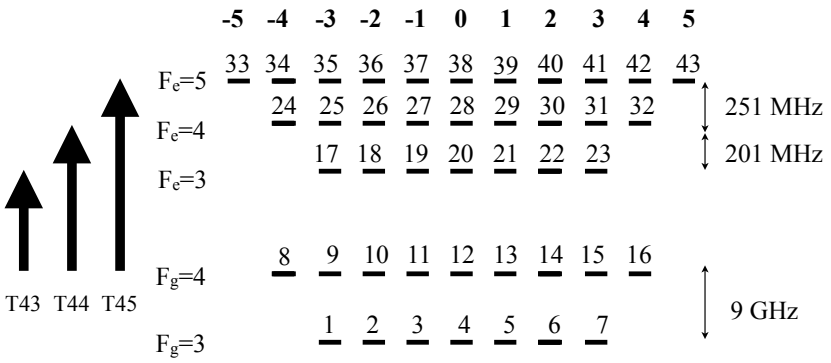

Figure 3.4: Zeeman structure of the Cs hyperfine levels involved in the T43, T44 and T45 transitions. The numbers are the labels of the Zeeman levels considered in the model reported in section 3.1.7. Since we considered only hyperfine transitions having $F_g = 4$ as lower energy level, the $F_e = 2$ is not shown, being not accessible for the selection rule $\Delta F = 0,\ \pm 1$.

We remark that eq. (3.14) gives an approximated expression for the time-dependent radiation intensity, that does not take into account possible off-axis atomic trajectories. This simplifying assumption relies on the determination of the average interaction time discussed in section 3.1.2.

From eq. (3.14) it follows that the excitation electric field, to which the Rabi frequency is proportional (see eq. (2.6)), can be written as:

$$E(t) = E_0\ e^{-\frac{t^2}{2\tau_{int}^2}} \tag{3.15}$$

where E_0 is the radiation electric field amplitude.

The term $\langle F_g,\ m_g|er_q|F_e,\ m_e\rangle$ in eq. (3.13) represents the dipole matrix element between the two levels involved in the transition. The dipole matrix element can be factorized [68, 69] as the product of a coefficient c_{F,m_F}, depending on the particular hyperfine transition, and the reduced dipole matrix element $\langle n_g L_g||e\vec{r}||n_e L_e\rangle$, having the same value for all the hyperfine transitions in the fine structure manifold:

$$\langle F_g,\ m_g|er_q|F_e,\ m_e\rangle = c_{F,m_F}\langle n_g L_g||e\vec{r}||n_e L_e\rangle \tag{3.16}$$

(where F is the total atomic angular momentum, m_F its projection onto the

quantization axis and q the component of the photon angular momentum on the quantization axis) with

$$c_{F,m_F} = \sqrt{(2J_e+1)(2J_g+1)(2F_e+1)(2F_g+1)(2L_g+1)}\cdot \\ \cdot \begin{Bmatrix} L_g & J_g & S \\ J_e & L_e & 1 \end{Bmatrix} \cdot \begin{Bmatrix} J_g & F_g & I \\ F_e & J_e & 1 \end{Bmatrix} \cdot \begin{pmatrix} F_e & 1 & F_g \\ m_e & q & -m_g \end{pmatrix}. \quad (3.17)$$

where L, S, J, I and m_F have been introduced in section 2.1.1 and section 2.1.2. The expressions in curly (round) brackets are the Wigner $6-j$ $(3-j)$ symbols. The value of q is the component of the photon angular momentum on the quantization axis: it is 0 for π-transitions, as in our configuration. The reduced dipole matrix element $\langle n_g L_g||e\vec{r}||n_e L_e\rangle$ (n is the principal quantum number) can be calculated via the expression:

$$|\langle n_g J_g||e\vec{r}||n_e J_e\rangle| = \sqrt{(2J_e+1)(2L_g+1)} \begin{Bmatrix} L_g & L_e & 1 \\ J_e & J_g & S \end{Bmatrix} \cdot \\ \cdot |\langle n_g L_g||e\vec{r}||n_e L_e\rangle|, \quad (3.18)$$

in which the value of $\langle n_g J_g||e\vec{r}||n_e J_e\rangle$ can be obtained from its relationship with the $6P_{3/2}$ decay rate Γ [70]:

$$\Gamma = \frac{\omega^2}{3\pi\epsilon_0\hbar c^3}\frac{2J_g+1}{2J_e+1}|\langle n_g J_g||e\vec{r}||n_e J_e\rangle|^2. \quad (3.19)$$

With reference to fig. 3.4, let us consider a transition between a Zeeman ground level ($a = 1,\ldots,16$) and an excited Zeeman level ($b = 17,\ldots,43$), driven by q-polarized radiation. Substituting eq. (3.19) into eq. (3.18), and in turn the latter into eq. (3.16), the Rabi frequency of eq. (3.13) can be rewritten in the convenient form [71]:

$$\Omega_{ab}(t) = C_{ab}^q \sqrt{\frac{3I_{p,\ exc}\lambda^3\Gamma}{4\pi^2\hbar c}} \exp\left(-\frac{t^2}{2\tau_{int}^2}\right) \quad (3.20)$$

where the dependence on the particular hyperfine levels involved is confined

into the angular momentum coupling coefficient C_{ab}^{q}:

$$C_{ab}^{q} = \frac{c_{F,m_F}}{\sqrt{(2J_g+1)(2L_g+1)}} \frac{1}{\left\{ \begin{array}{ccc} L_g & L_e & 1 \\ J_e & J_g & S \end{array} \right\}} = \\ = \sqrt{(2J_e+1)(2F_e+1)(2F_g+1)} \cdot \\ \cdot \left\{ \begin{array}{ccc} J_g & F_g & I \\ F_e & J_e & 1 \end{array} \right\} \cdot \left(\begin{array}{ccc} F_e & 1 & F_g \\ m_e & q & -m_g \end{array} \right) \tag{3.21}$$

The Rabi frequency of eq. (3.20) has been used in the simulation reported in section 3.1.7.

Finally, the $6-j$ and $3-j$ symbols of eq. (3.21) impose the following selection rules for the hyperfine transitions, useful in the following: $\Delta F = |F_e - F_g| = 0,\ 1$, $\Delta m = m_e - m_g = 0, \pm 1$ (0 for π polarized, ± 1 for circularly polarized radiation). Furthermore, the transition $|F_g,\ m_g = 0\rangle \rightarrow |F_e,\ m_e = 0\rangle$ is prohibited if $F_g = F_e$.

3.1.4 Transition strengths and transition strength ratios

The strength of a transition between two Zeeman sublevels in a hyperfine manifold is given by the square of the dipole matrix element shown in eq. (3.16). Therefore the strength of the transition can be written as [72]:

$$|c_{F,\ m_F}|^2 = (2J_e+1)(2J_g+1)(2F_e+1)(2F_g+1)(2L_g+1) \cdot \\ \cdot \left\{ \begin{array}{ccc} L_g & J_g & S \\ J_e & L_e & 1 \end{array} \right\}^2 \cdot \left\{ \begin{array}{ccc} J_g & F_g & I \\ F_e & J_e & 1 \end{array} \right\}^2 \cdot \\ \cdot \left(\begin{array}{ccc} F_e & 1 & F_g \\ m_e & q & -m_g \end{array} \right)^2$$

Because of the degeneracy on F of the hyperfine levels in the absence of a magnetic field, the strength of the $F_g \rightarrow F_e$ transition can be quantified by

$S_{F_gF_e}(\times 9/11)$	$F_e = 3$	$F_e = 4$	$F_e = 5$
$F_g = 3$	21/44	15/44	0
$F_g = 4$	7/44	21/44	1

Table 3.1: Table of the factors $S_{F_gF_e}$, which provide a measure of the relative strength of the hyperfine transitions $F_g \to F_e$ of the D_2 line in Cesium.

the factor:

$$S_{F_gF_e} = \sum_{m_g=-F_g}^{F_g} \sum_{m_e=-F_e}^{F_e} |c_{F,m_F}|^2. \tag{3.22}$$

The numerical values of the S_{Fg,F_e} factors are reported in table 3.1 for the hyperfine transitions of the D_2 line. The transition strength ratios are defined as [73, 74] :

$$R_{F_gF_e,F'_gF'_e} = \frac{S_{F_gF_e}}{S_{F'_gF'_e}}. \tag{3.23}$$

From table 3.1 we compute the values relative to the T43 T44 and T45, useful in the following:

$$R_{45,44} = \frac{44}{21} \approx 2.1 \tag{3.24}$$

$$R_{44,43} = \frac{21}{7} = 3 \tag{3.25}$$

3.1.5 Relative line intensities in the two-level model

In this section we see how, according to the two-level theory, the relative line intensities for the T43, T44 and T45 in Cs depend on the excitation intensity. We will exploit eq. (3.4) but, before doing that, we have to find suitable expressions of the Rabi frequency for these transitions. Neglecting, for simplicity, the time dependence of the atom-radiation interaction, by means of eq. (3.20) we define an "overall" Rabi frequency $\tilde{\Omega}_{F_g,F_e}$ for the hyperfine transition $F_g \to F_e$:

$$\tilde{\Omega}_{F_g,F_e} = \tilde{\Omega}_0 \sqrt{\sum_{m_g=-F_g}^{F_g} \sum_{m_e=-F_e}^{F_e} |c_{F,m_F}|^2} = \tilde{\Omega}_0 \sqrt{S_{F_g,F_e}} \tag{3.26}$$

where we exploited eq. (3.22) and noted that:

$$\tilde{\Omega}_0 = \sqrt{\frac{3I_{p,\ exc}\lambda^3\Gamma}{4\pi^2\hbar c}} \frac{1}{\sqrt{(2J_g+1)(2L_g+1)} \begin{Bmatrix} L_g & L_e & 1 \\ J_e & J_g & S \end{Bmatrix}} \tag{3.27}$$

is the same for the T43, T44 and T45. By means of eq. (3.26) and eq. (3.4) we obtain the relative line intensities:

$$\mathcal{R}_{45,44} = \left(\frac{\tilde{\Omega}_{45}}{\tilde{\Omega}_{44}}\right)^2 \frac{\Gamma^2 + 2\tilde{\Omega}_{44}^2}{\Gamma^2 + 2\tilde{\Omega}_{45}^2} \tag{3.28}$$

$$\mathcal{R}_{44,43} = \left(\frac{\tilde{\Omega}_{44}}{\tilde{\Omega}_{43}}\right)^2 \frac{\Gamma^2 + 2\tilde{\Omega}_{43}^2}{\Gamma^2 + 2\tilde{\Omega}_{44}^2}. \tag{3.29}$$

In fig. 3.5 the relative line intensities $\mathcal{R}_{45,44}$ and $\mathcal{R}_{44,43}$ are plotted as a function of the excitation power. The quantity $\tilde{\Omega}_0$ has been computed using the actual experimental parameters, so that the theoretical relative line intensities in fig. 3.5 can be directly compared to the experimental ones, represented by the points in fig. 7.8. Comparing fig. 3.5 and fig. 7.8 we can make two

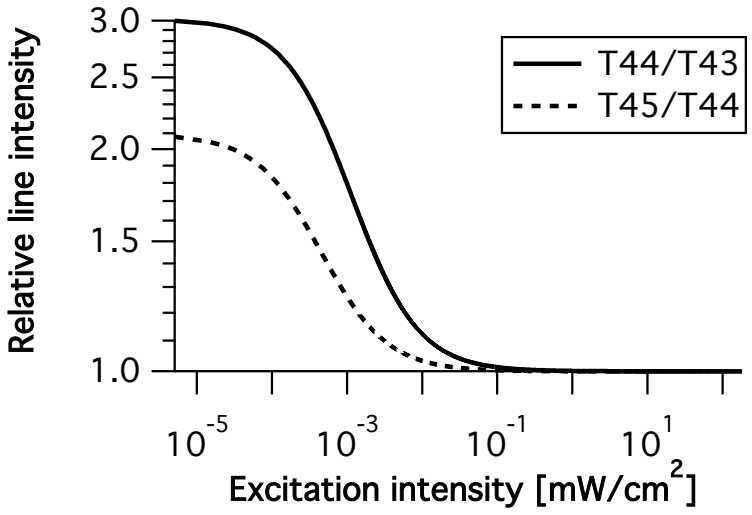

Figure 3.5: Relative line intensities for the hyperfine transitions T45/T44 and T44/T43 computed according to the two-level atomic model.

considerations:

- at extremely low excitation intensity both the experimental and two-level theoretical relative line intensities tend to the corresponding transition strength ratio: $\mathcal{R}_{45,44} \approx R_{45,44} = 2.09$, $\mathcal{R}_{44,43} \approx R_{44,43} = 3$. From this we infer that, in the extremely low ($I \ll I_{sat}$) intensity regime, a multilevel system can actually be approximated as a "superposition" of two-level systems

- when the excitation intensity is increased, the accuracy of the two-level model breaks down. In this approximation, in fact, all the T43, T44 and T45 transitions tend to the same intensity (i.e. their relative line intensities tend to 1) at high excitation power; this is due to the saturation of the excited state populations that tend to 1/2 for all three transitions. On the contrary, as we will point out in chapter 7, the experimental results show clearly that the dependence on the excitation intensity of the $\mathcal{R}_{45,44}$ is completely different from that of $\mathcal{R}_{44,43}$: while the latter retains somehow the behavior predicted by the two-level model, decreasing with the excitation intensity, the $\mathcal{R}_{45,44}$, instead, increases rapidly.

It is then clear that the two-level model describes properly the interaction between radiation and multilevel atoms only in an extremely low intensity regime; when this increases, the phenomena neglected (the optical pumping, treated in section 3.1.6) increasingly affect the experimental data.

3.1.6 Hyperfine and Zeeman optical pumping

Several experimental investigations demonstrated the dependence of optical pumping effects on the excitation intensity [65], magnetic field [75] and interaction time [67]. In particular, it has been shown that in a multilevel atom, even if the excitation takes place in a moderate intensity regime (as we will see in section 7.2.2, experimentally we explored the intensity range $0.02 \div 200$ mW/cm^2), an enough long interaction time ($\tau_{int} \approx 100$ μs, as in our situation) between atoms and radiation ensures the appearance of not

negligible optical pumping effects. These effects are based, as we discuss in this section, on the leakage between hyperfine states and on the occurrence of "dark" Zeeman levels. The presence, typical of the alkaline atoms, of two hyperfine ground states ($F_g = 3$ and $F_g = 4$, see fig. 3.4) is the cause of the population leakage at the basis of the hyperfine optical pumping (HP) [71, 76, 77]. The occurrence of the HP is due to the probability that an excited atom spontaneously decays into an hyperfine ground state different from that from which it started. When this probability is not zero, the transition is told to be "open". Let us refer to fig. 3.4, considering an atom, initially in the level $F_g = 4$, that is excited to the state $F_e = 3$ by resonant radiation. It is evident that the atom can decay back to the $F_g = 4$ state, but also to the $F_g = 3$, since this decay does not violate any of the selection rules reported in section 3.1.3. The same considerations are true also in the case of the $F_g = 4 \rightarrow F_e = 4$ case; therefore, the T43 and T44 transitions are defined as "open". On the contrary, in the case of the T45, because of the selection rule $\Delta F = 0, \pm 1$, the atom excited to the $F_e = 5$ state can decay back only into the $F_g = 4$ level: then, the transition T45 is "closed". However, in a multilevel system, radiation tuned on the T45 resonance has a non zero probability to bring an atom from the $F_g = 4$ to the $F_e = 4$ state, from which it can then decay back into the ground hyperfine level $F_g = 3$. When the atom is in the $F_g = 3$ level, it cannot be excited again by the radiation, since the frequency detuning between $F_g = 3$ and $F_g = 4$ states is about 9 GHz. According to such a mechanism, the atoms are accumulated in the "dark" ground hyperfine level $F_g = 3$. In the laser cooling experiments, the existence of this pumping makes necessary the presence, beyond the cooling laser beam, of a "repumping" laser beam that, tuned on the $F_g = 3 \rightarrow F_e = 4$ transition, recycles the atoms.

The Zeeman pumping (ZP) [78] is responsible for the piling up, during the interaction with polarized radiation, of the atomic population in certain ground Zeeman sublevels from which the absorption of a photon is forbidden and that, for this, act as traps for the atoms. It is well known that this phenomenon, when taken into account, affects the interaction between radiation and even a two-level system, leading, for example, to the introduction of correction

factors for the transition Rabi frequency used in section 2.2.2 [79].

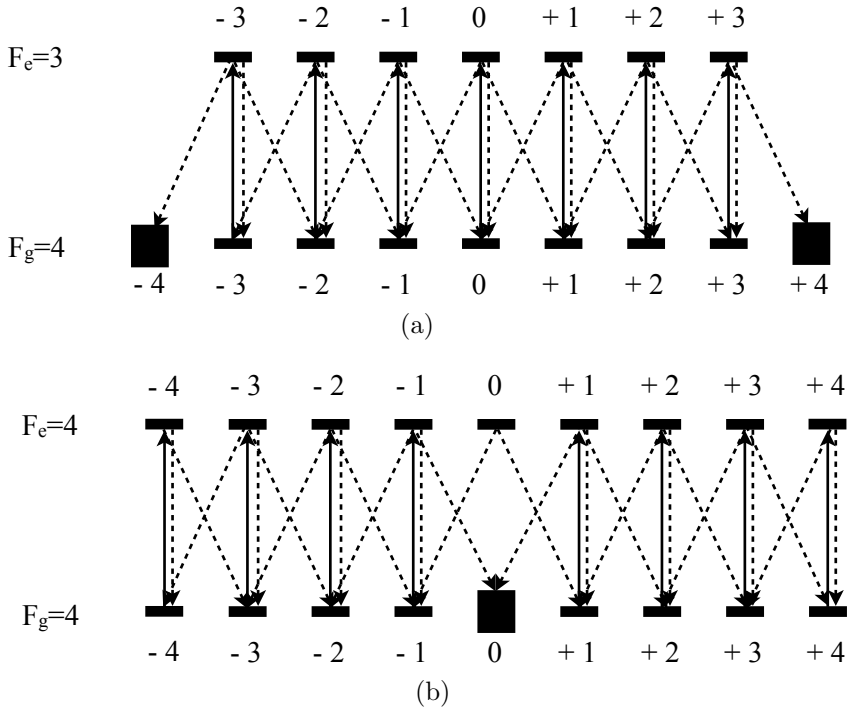

Figure 3.6: Zeeman sublevels involved in the (a) T43 and (b) T44. The continuous and dashed lines represent the absorption and spontaneous emission transitions between the Zeeman sublevels, respectively. The larger thickness of the levels $F_g = 4, m_g = \pm 4$ in (a) and $F_g = 4, m_g = 0$ in (b) indicates that they act as traps for the atoms.

Let us consider the T43 and the Zeeman structure of the levels involved in the transition, as shown in fig. 3.6 (a), where the vertical continuous lines represent the absorption of a π polarized photon, while the dashed lines represent the spontaneous emissions. We see that, differently from the continuous arrows, the dashed ones can be tilted, due to the difference between the m-selection rule for the absorption ($\Delta m = 0$) and for the spontaneous emission ($\Delta m = 0,\ \pm 1$) processes. This fact leads to the accumulation of the population in the $F_g = 4,\ m_g = \pm 4$ levels, that the atoms cannot leave owing to the absence of suitable levels to which they can be excited. The situation is quite similar for the T44; the only difference is that here the trap level is represented by $|F_g = 4,\ m_g = 0\rangle$, because of the selection rule, mentioned

in section 3.1.3, stating that the transition $|F_g,\ m_g = 0\rangle \rightarrow |F_e,\ m_e = 0\rangle$ is forbidden when $F_g = F_e$.

3.1.7 Numerical treatment of the multilevel atom-radiation interaction

From the discussion of section 3.1.6, we realize that the interpretation of optical pumping effects on the population dynamics of an atomic sample interacting with polarized radiation, is a task hard enough to justify the use of a numerical simulation. We also remark that in other situations treated in the literature [65, 69], the excitation intensities were low enough to justify approximations leading to an analytical solution of the population dynamics problem. In our experimental conditions these approximations are not applicable, since the atoms move across a spatially varying intensity whose peak value can be 200 times the saturation intensity. Analogously to what we saw in section 2.2 for the two-level system, the internal dynamics of the multilevel systems can be properly described in the semiclassical formalism of the OBE [72]. The numerical solution of these equations during the motion of the atoms through the laser beam determines the transient behavior of the populations of all the relevant hyperfine levels. Furthermore, in this framework also the coherences between the levels are taken into account [80], whose effect is negligible in the low intensity regime but becomes important increasing the laser intensity, determining the evolution of nonlinearities in the laser-atom interaction [81].

We make a digression, remarking that in our setup the measured ion yield is the result of two distinct steps: at first the excitation and ionization processes occur, as determined by the atom-radiation interaction; then the ion capture, controlled by the ion collection capabilities of the charge detection system, takes place. This remark justifies the approach we followed in modeling separately the two processes. In fact, in this section we concentrate on the excitation/ionization, while in section 7.4.2 we will focus on the modeling

of the electrostatic configuration, computing the ion trajectories inside the vacuum chamber and deducing the dynamical features of the ion beam.

The Liouville's equation for the density matrix evolution [82]

$$\frac{d\rho}{dt} = -\frac{i}{\hbar}\left[H, \rho\right] \tag{3.30}$$

gives rise to $N \times N = 43^2 = 1849$ evolution equations for populations and coherences. The procedure and the approximations to take into account the spontaneous emission and reduce the number of equations are well known, and their discussion will be omitted here. On the contrary, we will focus mainly on the details of the experimental configuration that we considered in order to reproduce accurately the experimental data.

As mentioned in section 3.1.2, the simulation is carried out for a single atom interacting with the radiation for a time $\tau_{int} = 105$ μs.

The equations ruling the time evolution of the density matrix elements ρ_{ab} are a generalization of the eq. (2.13) [82]:

$$\dot{\rho}_{ab} = -i\omega_{ab}\rho_{ab} - \frac{i}{\hbar}\sum_{c}(H^{int}_{ac}\rho_{cb} - \rho_{ac}H^{int}_{cb}) + l_{ab} \tag{3.31}$$

where H^{int}_{ij} is given by eq. (2.4), the Ω_{ij} by eq. (3.13) and where the terms l_{ab} describe phenomenologically the decay of the excited-state populations and of the coherences. On the basis of the same approximation used to obtain the eq. (2.13), and disregarding all the couplings not between an excited ($b = 17, \ldots, 43$) and a ground ($a = 1, \ldots, 16$) state, the set of evolution

equations reads [71, 80, 81]:

$$\text{for } a = 1, \ldots, 7$$

$$\frac{d\rho_{aa}}{dt} = \Gamma \sum_{q=-1}^{1} \sum_{b=17}^{32} (C_{ab}^{q})^2 \rho_{bb}, \tag{3.32a}$$

$$\text{for } a = 8, \ldots, 16$$

$$\frac{d\rho_{aa}}{dt} = \sum_{b=17}^{43} \Omega_{ba} \mathrm{Im}(\sigma_{ba}) + \Gamma \sum_{q=-1}^{1} \sum_{b=17}^{43} (C_{ab}^{q})^2 \rho_{bb}, \tag{3.32b}$$

$$\text{for } b = 17, \ldots, 43$$

$$\frac{d\rho_{bb}}{dt} = -\sum_{a=8}^{16} \Omega_{ab} \mathrm{Im}(\sigma_{ab}) - \Gamma \rho_{bb} - r_{ion}(t) \rho_{bb}, \tag{3.32c}$$

$$\text{for } a = 8, \ldots, 16, \quad b = 17, \ldots, 43$$

$$\frac{d\sigma_{ab}}{dt} = i(\omega_{ab} - \omega)\sigma_{ab} - \frac{i}{2}\Omega_{ba}(\rho_{bb} - \rho_{aa}) - \frac{\Gamma}{2}\sigma_{ab} \tag{3.32d}$$

where the C_{ab}^{q} are given by eq. (3.21). The roles of the several terms in these equations are worth to be briefly discussed.

The eq. (3.32a), sum of the decay terms from the excited states, describes the increase in the "dark" hyperfine $F_g = 3$ ground state population during the propagation of the atoms across the radiation. Therefore, these terms are directly related to the HP. Similar contributions, together with the stimulated transitions terms, appear also in eq. (3.32b) and eq. (3.32c) for the evolution of the $F_g = 4$ and $F_e = 3,\ 4,\ 5$ populations, respectively. The third term in eq. (3.32c) takes into account the loss of excited atoms due to the ionization: the expression of the ionization rate $r_{ion}(t)$ will be given in eq. (4.13). Here we just anticipate (we will give more details in section 4.3) that in our experimental conditions, as typical in CW experiments, the ratio between the excited atoms loss rate for photoionization, $r_{ion}(t)$, and for radiative spontaneous emission, Γ, is about 10^{-6}. Hence, the ionization process allows to probe the excited state population practically without perturbing the population itself. This implies that the population in the excited state is determined only by the interaction with the excitation radiation. Finally,

eq. (3.32d) governs the time dependence of the atomic coherences between ground and excited sublevels.

We also underline the presence, in eq. (3.32a) and eq. (3.32b), of the sums on the polarizations $q = -1,\ 0,\ 1$ of the spontaneously emitted photons, accounting for the spontaneous emission selection rules $\Delta m = 0,\ \pm 1$. These terms are responsible for the population buildup taking place in the Zeeman states that we discussed in section 3.1.6. We remark that in the simulation it is possible to "switch off" the effects of the ZP, suppressing the sums on the polarizations q, so that the evolution of the populations is ruled only by the HP. In section 7.2.2 we will exploit this fact to ascertain the roles played by HP and ZP separately in determining the trend of the experimental data.

The initial atomic internal state is chosen as a superposition of equally populated ground Zeeman levels [71], that is $\rho_{aa} = \frac{1}{16}$. This is justified due to the relatively weak magnetic field. Furthermore, several tests with the simulation didn't show critical dependence of the results on the initial conditions. While for the non-diagonal elements we set $\rho_{ab} = 0$. Furthermore, the solution is evaluated between the instants $\pm 10\ \tau_{int}$.

When the numerical computation of the OBE is over, the computed excited Zeeman populations ρ_{bb} are used to evaluate the quantity [65, 83]:

$$I(\delta,\ P_{exc}) = \int_{-\infty}^{+\infty} r_{ion}(t) \sum_{b=17}^{43} \rho_{bb}(t,\ \delta,\ P_{exc}) dt, \tag{3.33}$$

where δ and P_{exc} represent[4], respectively, the detuning and the power of the excitation laser. The line intensity (as defined in section 3.1) is given by $I_{45} = I(0,\ P_{exc})$, $I_{44} = I(-\delta_{45},\ P_{exc})$ and $I_{43} = I(-\delta_{35},\ P_{exc})$ for the T45, T44 and T43 respectively.

In a two-photon, two-color ionization scheme the line intensity, as defined in eq. (3.33), has a clear physical meaning, being proportional to the ionized fraction of the atomic population and, consequently, related to the experimental ionization rate. In fact, if we consider, in the approximation of very

[4]In the following we will take as the origin of the frequency axis the T45 frequency. So, when the laser is tuned on the T45, $\delta = 0$; when it is tuned on the T44, $\delta = -\delta_{45} = -251$ MHz; when it is tuned on the T43, $\delta = -\delta_{35} = -452$ MHz.

low ionization rate (that is, we consider the number of excited atoms N_{at}^{exc} as being determined exclusively by the interaction with the excitation radiation), the number of atoms dN_{at}^{exc} entering the ionization volume and being excited between t and $t + dt$:

$$dN_{at}^{exc}(t) = F_{at}\ \rho_{ee}(t)dt \tag{3.34}$$

where F_{at} is the atomic flux and $\rho_{ee}(t)$ the excited state population, we have that the corresponding number of ions generated (per unit time) between t and $t + dt$ is:

$$dF_{ion}(t) = r_{ion}(t)dN_{at}^{exc}(t) = F_{at}r_{ion}(t)\rho_{ee}(t)dt. \tag{3.35}$$

Hence, the ionization rate (number of ions generated per unit time) can be written as:

$$\begin{aligned} F_{ion} &= \int_{-\infty}^{+\infty} dF_{ion}(t) = \\ &= F_{at}\int_{-\infty}^{+\infty} r_{ion}(t)\rho_{ee}(t)dt = F_{at}I(\delta,\ P_{exc}) \end{aligned} \tag{3.36}$$

Finally, taking into account the efficiency $\eta \leq 1$ of the charge collecting system, we find the following relation between the experimental ionization rate F_{ion}^{exp} and the numerically computed $I(\delta,\ P_{exc})$:

$$F_{ion}^{exp} = \eta F_{ion} = \eta F_{at} I(\delta,\ P_{exc}). \tag{3.37}$$

Actually, because of the unavailability of an independent charge source allowing an absolute calibration of the charge collection system, the factor η is unknown. Accordingly, the direct comparison between experimental and numerical data, embodied in eq. (3.37), is impossible. However, the uncertainty related to η can reasonably be avoided if we refer to the relative line intensities, analogously to what we did in section 2.2:

$$\mathcal{R}_{F_gF_e,F'_gF'_e} = \frac{F_{ion}^{exp}(F_g \to F_e)}{F_{ion}^{exp}(F'_g \to F'_e)} = \frac{I(F_g \to F_e)}{I(F'_g \to F'_e)} \tag{3.38}$$

where we exploited eq. (3.37). In section 7.2.2 the measured ion yields will be used to obtain the experimental relative line intensities that will be directly compared to the numerically computed ones, via the eq. (3.38).

3.2 Sub-Doppler cooling

Having introduced optical pumping in a multilevel system, in this section we treat briefly the sub-Doppler cooling process, that just on the effects of optical pumping heavily relies.

Since a long time is has been experimentally ascertained that the temperature of eq. (2.21) is not a fundamental lower limit for the laser cooling techniques [84]. The theory, which was subsequently developed, had to take into account the multiplicity of the sublevels constituting an atomic state (i.e. Zeeman levels and hyperfine structure) and the dynamics of the optical pumping between them, in order to explain the achievement of ultralow temperatures. At the basis of the onset of these temperature regimes there is the non-adiabatic response of the atom to the polarization state of the field in which it moves, where the term "non-adiabatic" indicates the possibility of transitions between different states. The two most relevant sub-Doppler cooling schemes are called lin $\perp$ lin and $\sigma_+\sigma_-$.

3.2.1 Configuration lin$\perp$lin

If we consider the superposition of two one-dimensional laser beams with linear orthogonal polarizations, the resulting field is:

$$\begin{aligned}\mathbf{E}(z,t) &= E_0\hat{\mathbf{x}}\cos(kz-\omega t) + E_0\hat{\mathbf{y}}\cos(kz+\omega t) = \\ &= E_0((\hat{\mathbf{x}}+\hat{\mathbf{y}})\cos kz\cos\omega t + (\hat{\mathbf{x}}-\hat{\mathbf{y}})\sin kz\sin\omega t)\end{aligned} \tag{3.39}$$

The polarization of this field (fig. 3.7) changes on distances of $\lambda/2$ from linear (at 45° with respect to the polarizations of the two beams) to σ^+ to again linear (but orthogonal to the previous direction), to σ_-. The effect of this polarization gradient has been analyzed in [85] in the particular case

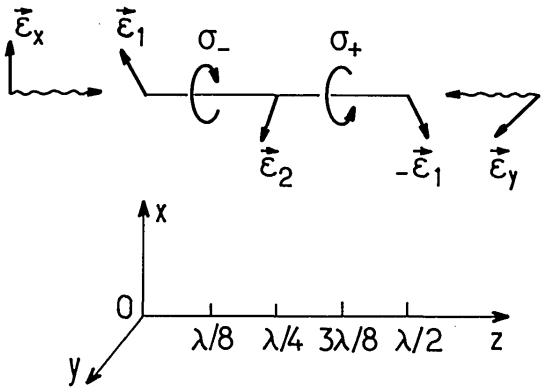

Figure 3.7: Spatial variation of the polarization of the field resulting from the superposition of two counterpropagating beams with linear and orthogonal polarizations.

of a transition $J_g = 1/2 \rightarrow J_e = 3/2$. Briefly, there is a change of the atomic populations during the motion through the radiation field: in fact, where the polarization is σ^+, the ground state population is pumped in the sublevel $m_g = 1/2$, since $\langle \Delta m_{trans} \rangle = \langle \Delta m_{abs} \rangle - \langle \Delta m_{em.\ sp.} \rangle \geq 0$ (we remind the selection rules $\Delta m^{abs}_{\sigma_+} = +1$ and $\Delta m_{em.\ sp.} = \pm 1, 0$). So, in a cycle absorption-spontaneous emission the average Δm for every scattering event is non negative; this causes a population increase in the Zeeman sublevel $m_g = J_g$. The situation is the opposite where the polarization is σ_-, with the ground state population pumped in the Zeeman sublevel $m_g = -J_g$. Moving in such a field, the atomic populations have to change between the levels $m_g = 1/2$ and $m_g = -1/2$ on distances on the order of $\lambda/2$. Furthermore, a quasi-resonant field not only produces optical pumping between the Zeeman sublevels of the ground state, but it induces also energy shifts (*light shift* [86]), because of the ac Stark effect.

At the origin of the cooling there is the fact that it is possible to select the couples of sublevels involved in the transition and to make their energy shifts dependent on the atomic position. Referring to fig. 3.8, we consider an atom that moves from $z = \lambda/8$ with velocity v; for this polarization configuration, the atom is in the sublevel $m_g = -1/2$ since, because of the light shift, this is the level with less energy. During its motion, the atom has to use a part

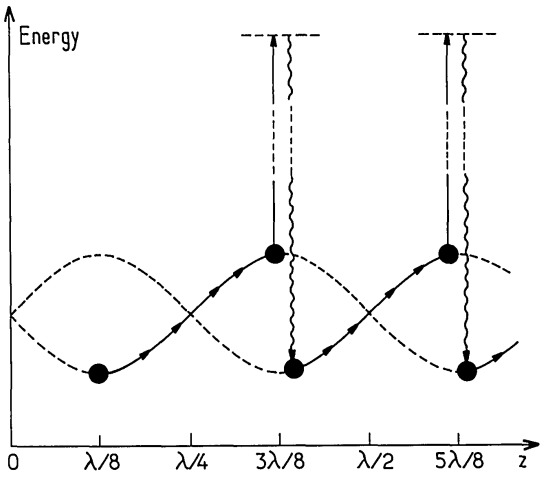

Figure 3.8: Cooling mechanism for lin $\perp$ lin configuration.

of its kinetic energy to increase its potential energy: the polarization, in fact, is changing and the sublevel $m_g = -1/2$ is always less coupled to the field. When the atom reaches $z = 3\lambda/8$, where the polarization is σ^+, it is pumped into the lower energy level $m_g = 1/2$. Since the spontaneously emitted photons have frequencies larger than the ones absorbed, in the process the atom converts part of its kinetic energy in potential energy, that is then radiatively lost: this is the cooling mechanism called *Sisiphus effect*. We underline that the atoms that efficiently undergo this process are only those with velocities in a small interval; in fact, only the atoms with a velocity such that they undergo a pumping process on a distance of $\lambda/4$ [86], are efficiently slowed down.

3.2.2 Configuration $\sigma_+\sigma_-$

In this sub-Doppler cooling mechanism, completely different from the lin $\perp$ lin, the counterpropagating laser beams are circularly polarized in opposite sense.

The resulting field is:

$$\mathbf{E}(z,t) = E_0\hat{\mathbf{x}}\cos(kz-\omega t) + E_0\hat{\mathbf{y}}\cos(kz+\omega t) + \tag{3.40}$$

$$+ E_0\hat{\mathbf{x}}\sin(kz-\omega t) + E_0\hat{\mathbf{y}}\sin(kz+\omega t) = \tag{3.41}$$

$$= 2E_0\cos\omega t(\hat{\mathbf{x}}\cos kz + \hat{\mathbf{y}}\sin kz). \tag{3.42}$$

the polarization is linear in every point in space but the polarization axis rotates of an angle π on the distance $\Delta z = \lambda/2$ (fig. 3.9). Considering a

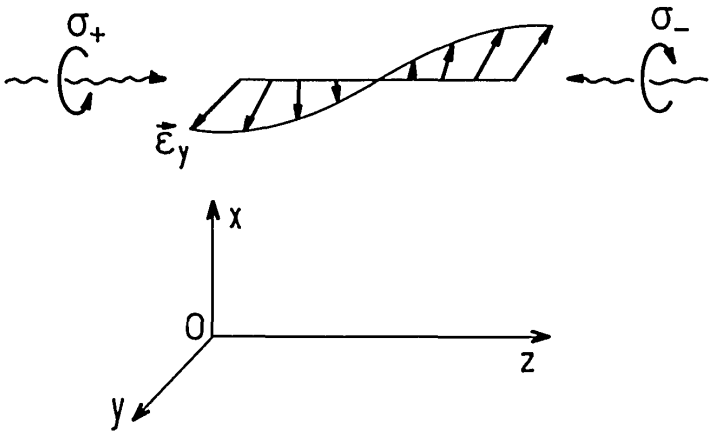

Figure 3.9: Spatial variation of the polarization of the field resulting from the superposition of two counterpropagating laser beams having opposite circular polarizations.

transition $J_g = 1 \rightarrow J_e = 2$, since the optical pumping tends to redistribute the population among the magnetic sublevels according to the local direction of polarization, the more populated sublevel will be the one with $M_g = 0$. However, since the atoms are moving, they have to be optically pumped to follow the rotation of the polarization axis. There is then a delay between the population of an atom in motion with respect to that of an atom fixed in that point. In [86] it has been shown that this effect results in a larger population of the level $M_g = 1$ with respect to the $M_g = -1$ for the atoms moving against the σ^+ polarized laser beam, In fact, the level $M_g = 1$ scatter the photons σ^+ six times more efficiently than the σ^-, because of the different Clebsch-Gordan coefficients. In this way a differential radiation scattering is

obtained, that brings to a viscous force proportional to the atomic velocity.

It is possible to show [60] that the temperature reached in the sub-Doppler cooling process is given by:

$$k_B T = c\frac{\hbar\Omega_0^2}{|\delta|} \tag{3.43}$$

where c is a constant that depends on the cooling scheme (lin $\perp$ lin or $\sigma_+\sigma_-$). In realistic experiments [87] the sub-Doppler temperature for Cesium can reach values below 3 μK. The atomic velocities, in this regime, are lowerly bound by the recoil velocity $v_r = \frac{\hbar k}{M}$, that is the velocity change of an atom emitting or absorbing a photon of momentum $\hbar k$. This implies a minimum temperature reachable called recoil temperature T_r. The values of T_r and v_r are reported in table 2.1.

Chapter 4

Laser-cooled ion beams

In this chapter we develop the treatment of the photoionization process we introduced in chapter 2. In section 4.1 we derive the general expression of the photoionization rate. Then, in section 4.2 we estimate, for our experimental configuration, the figures of merit (emittance and brightness) generally used to quantify the quality of an ion beam. Finally, in section 4.3 we compute the photoionization rate $r_{ion}(t)$ that we introduced in the eq. (3.32c) of section 3.1.7 for the two-photon, two-color ionization scheme, making also some considerations on the processes, collateral to the photoionization of the Cs atoms, that can contribute to the experimental ionization signal.

4.1 Photoionization rate

In a $N-$photon ionization process the ionization rate $r_{ion}^{(i)}$ can be written in general as [88]:

$$r_{ion}^{(i)} = \Sigma_{ion,N}^{(i)} j_{ion}^{N} \tag{4.1}$$

where $\Sigma_{ion,N}^{(i)}$ is the generalized N-photon ionization cross-section (expressed in $\mathrm{m^{2N}s^{N-1}}$) of the atom in the i^{th} energy level, while j_{ion} represents the ionizing laser photon flux density (expressed in $\mathrm{m^{-2}s^{-1}}$). The rate of the 1-photon ionization process can be obtained from eq. (4.1), where $N = 1$ (only one ionizing photon is involved) and the generalized ionization cross

section reduces to the ionization cross section of the i^{th} energy level:

$$r_{ion}^{(i)} = \sigma_{ion}^{(i)} j_{ion}. \tag{4.2}$$

Using the relation $j_{ion} = \lambda_{ion} I_{ion}/hc$, where λ_{ion} and I_{ion} are ionization wavelength and intensity, the ionization rate can then be written as:

$$r_{ion}^{(i)}(t) = \sigma_{ion}^{(i)} \frac{\lambda_{ion} I_{ion}(t)}{hc}. \tag{4.3}$$

The time dependence of the ionization rate has been introduced because of the intensity profile of the ionization laser beam. With a reasoning similar to the one followed in section 3.1.2, the ionization intensity can be written as:

$$I_{ion}(t) = I_{p,ion} e^{-\frac{t^2}{\tau_{ion}^2}} \tag{4.4}$$

where $\tau_{ion} \approx 60$ μs is the average interaction time between atoms and ionization radiation, computed similarly to what done in section 3.1.2 for the interaction time between atoms and excitation radiation. We remark that $\tau_{ion} < \tau_{exc}$ because, as we will see in section 7.1, ionization and excitation laser beams have different sizes in the atomic propagation direction.

4.2 Cold atomic beam as ion source: performance estimates

The quality of an ion beam can be quantified by the emittance, a measure of the phase space occupied by the beam and defined as [89]:

$$\epsilon_x' = \frac{1}{\pi} \left(\int \int dx d\theta_x \right) \tag{4.5}$$

where x and θ_x are the transverse position and angular coordinates of an ion and the integration is over the transverse intensity and angular distribution of the ion beam. Since ϵ_x' changes with the energy of the beam, the normalized emittance ϵ_x is often more useful and it is given by the emittance scaled by

the square root of the beam energy U:

$$\epsilon_x = \epsilon'_x \sqrt{U} \tag{4.6}$$

It can be shown that the normalized emittance is an invariant quantity along the focusing optics (neglecting aberrations and space charge effects), and that it determines the final resolution of the system [90]. Higher quality of the beam corresponds to lower emittance. As a reference we can take the measured normalized emittance value for a Gallium LMIS operated in high-resolution mode, $\epsilon_x \simeq 10^{-6}$ π mm mrad$\sqrt{\text{MeV}}$ [91].

The useful current that can be focused into a spot is instead measured by the brightness B, that depends on the amount of current J that is emitted from an area A into a solid angle Ω. Thus, the brightness of a source is inversely proportional to its phase space area, given approximately by the product of the cross sectional area of the source and the angular spread of the ions emitted [38]:

$$B = \frac{d^2 J}{d\Omega dA} \tag{4.7}$$

Since the solid angle can change with the beam energy U, a more useful quantity is the normalized brightness:

$$\beta = \frac{B}{U} \tag{4.8}$$

related to the emittance by [92]:

$$\beta = \frac{I}{\epsilon_x \epsilon_y} \tag{4.9}$$

where ϵ_x and ϵ_y are the normalized emittances[1] in the two orthogonal directions transverse to the propagation axis. As the normalized emittance, the normalized brightness is an invariant along the focusing optics, too. A high brightness allows a small focal spot with high current. Again as a reference, the Gallium LMIS can reach values of $\beta = 5.8 \cdot 10^7$ A cm^{-2}sr^{-1}MeV^{-1} [94]. A

[1]The expression of the normalized emittance in eq. (4.9) can differ by a factor $8\pi^2$ from other expressions found in the literature (e.g. [52, 93]).

high brightness source can thus be obtained by either a small effective area or a small angular spread. For example, the present LMIS ion sources attain a very high brightness from a tiny effective size of the source: about 50 nm [90], with an angular spread half angle of about 25°.

We conclude this section with some rough estimates for our two-photon, two-color ionization scheme of the parameters introduced above for the atomic beam. We consider an ion source in a field free region with a bidimensional Gaussian spatial distribution of standard deviations σ_x and σ_y in the $x,\ y$ transverse directions and a Gaussian transverse velocity distribution with temperature $T_{0,ion}$. In this case the normalized emittance $\epsilon_{x,y}$ can be written as [48]:

$$\epsilon_{x,y} = \sigma_{x,y}\sqrt{\frac{k_B T_{0,ion}}{2}} \tag{4.10}$$

If the photoionization takes place on threshold, because of the vanishing photon momentum and the huge inertia of the Cs atom, the produced ions inherit, approximately unmodified, the dynamical characteristics of the originating atoms. Thus we can infer that $T_{0,ion} = T_{0,at}$, where $T_{0,at} \approx 125\ \mu$K (see section 6.2) is the initial transverse atomic temperature. This is important in view of the applications of the apparatus as focused ion beam source. However, as we will see in section 4.3, in our configuration the available ionizing laser emits about 0.6 eV over-threshold. In this situation, a very rough estimate of $T_{0,ion}$ can be obtained considering the ionization process as a one dimensional collision between an excited atom and an ionizing photon, as shown in fig. 4.1. From the energy and momentum conservations it is straightforward to obtain an ion recoil kinetic energy less than 3 μeV and an electron recoil energy of about 0.6 eV. We observe that the electron recoil energy consists of practically all the excess energy of the ionizing photon in our above threshold photoionization, phenomenon well known and due to the large ion to electron mass ratio. From that value of the ion recoil kinetic energy we can roughly estimate an initial ion temperature $T_{0,ion} \approx 10$ mK. Furthermore, the transverse dimension of the ion source is determined by the geometry of the configuration in which the ionization takes place. Here we refer to the triple-beam crossed geometry, sketched in fig. 4.2, in which the

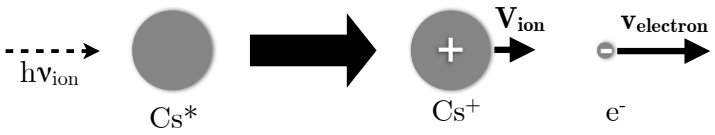

Figure 4.1: Collisional model of the photoionization process for an excited Cs atom. We remark that the electron emission is not necessarily taking place in the sketched direction.

photoionization of the atomic beam has been carried out (see section 7.1). In

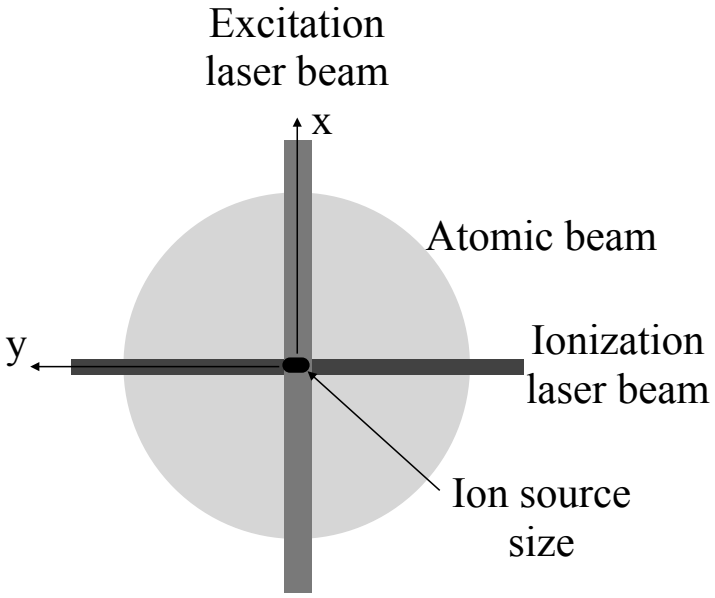

Figure 4.2: Sketch of the triple-crossed beam configuration in which the photoionization of the atomic beam (propagating in the direction perpendicular to the page) takes place. The ion source is defined by the intersection of the three beams: the atomic beam and the two laser beams, excitation and ionization.

this situation σ_x and σ_y are given by the transverse size of the excitation and ionization laser beams; with the data reported in section 7.1, we get:

$$\epsilon_x = 1.6 \cdot 10^{-5}\ \pi \text{ mm mrad } \sqrt{\text{MeV}} \tag{4.11}$$

$$\epsilon_y = 1.3 \cdot 10^{-5}\ \pi \text{ mm mrad } \sqrt{\text{MeV}}. \tag{4.12}$$

We underline that these values are just one order of magnitude larger (and, thus, worse) than those relative to the state-of-the-art LMIS; however, they refer to a set-up that has not been optimized at all and that, on the contrary, is still in its initial development stage.

To estimate the brightness, according to eq. (4.9), we need an estimate of the ion current. As we will see in section 7.1, the number of ions per second we can expect on the basis of our experimental parameters, in a CW regime, is about $3 \cdot 10^6$ singly-ionized ions/s, which correspond to about 0.5 pA. Also here, the comparison with the high-resolution mode LMIS is not favorable. However, we should again notice that, at least in principle, our experimental implementation is easily scalable, for example increasing the ionization power, to increase the number of ions.

4.3 Two-photon, two-color photoionization process

As already mentioned, in our photoionization scheme the atoms pass through two spatially superposed and collimated laser beams: one, at 852 nm, brings the atoms into one selected hyperfine sublevel of the excited state $6^2P_{3/2}$; the other, at 405 nm, is responsible for the above-threshold ionization of the excited atoms. Both the laser beams are linearly polarized and the relevant transitions scheme is sketched in fig. 4.3.

Before obtaining the expression of the photoionization rate suitable for our configuration, we make some considerations on the two-photon, two-color photoionization process. Here we focus on the interaction between Cs atoms and photons. The possible contributions to the ion yield given by the interaction between Cs atoms and entities different from photons (other Cs atoms and electrons) will be commented in section 4.3.1.

As we can see in fig. 4.4, the Cs atoms interact with photons of different energies $h\nu_{exc} = 1.45$ eV and $h\nu_{ion} = 2.44$ eV. As stated above, the photons of energy $h\nu_{exc}$ are resonant with the energy difference between two levels of the discrete energy spectrum (the ground and the first excited), while

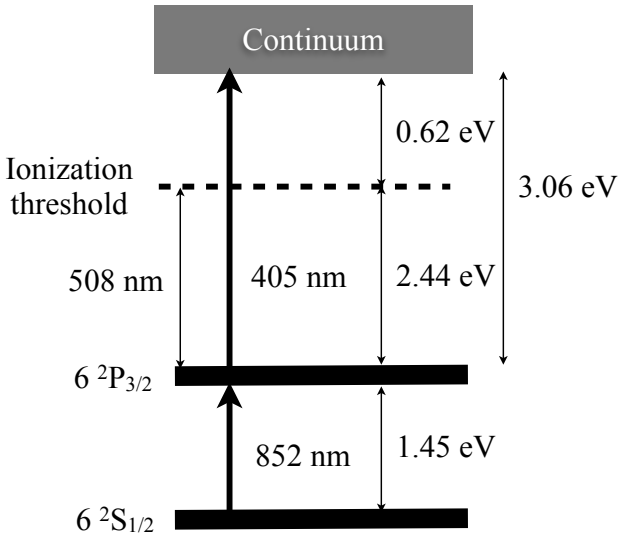

Figure 4.3: Laser configuration in the two-photon, two-color photoionization scheme. The beam at 852 nm resonantly excites the atoms to teh state $6^2P_{3/2}$, from which they are ionizaed over-threshold by the violet beam at 405 nm.

the others have an energy $h\nu_{ion}$ sufficient to ionize the Cs atoms that are in the first excited energy level. We note that $h\nu_{exc}$ and $h\nu_{ion}$, separately, are both less than $E_I = 3.89$ eV, the ground state Cs ionization energy. Therefore, no single photon can ionize a Cs atom in its ground state. On the contrary, $h\nu_{exc} + h\nu_{ion} > E_I$ implies that the photons necessarily have to sum up their energies in order to ionize the atoms. Given this condition, several processes, in principle, could lead to the formation of an ion: those involving two photons[2] are sketched in fig. 4.4. The process (a) consists of the absorption of an infrared (IR) excitation photon, followed by a violet (V) ionization photon. The rate of this process can be obtained using eq. (4.3), in which the ionization cross-section, relative to the first excited state and to the ionization wavelength used ($\lambda_{ion} = 405$ nm), is $\sigma_{ion} = 1.4 \cdot 10^{-17}$ cm^2 [95]. Furthermore, since the absorption of an IR and V photons are two statistically independent processes, the ion yield per unit time is given by the probability ρ_{ee} of the atom to be in the excited state, multiplied by the ionization rate of

[2]We neglect the processes with three and more photons since, as we will see in the following, they are extremely less probable than the processes at two photons.

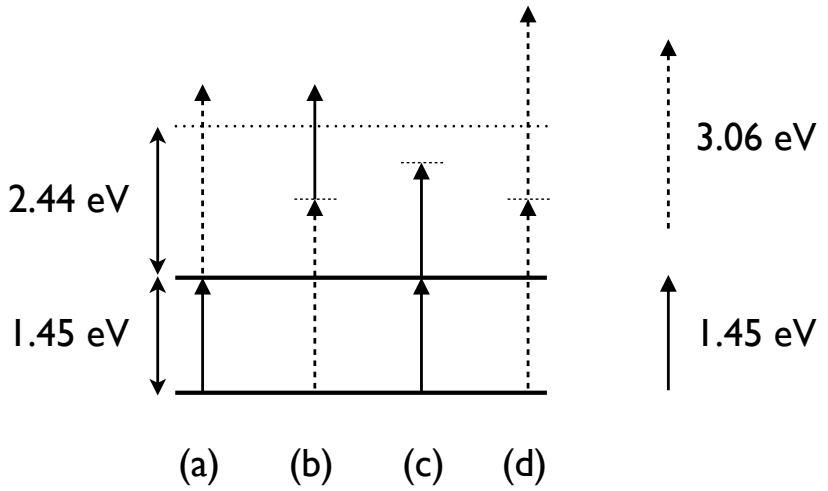

Figure 4.4: Several processes that can take place in the interaction atom-radiation in a two-photon, two-color ionization stage; involving only real atomic eigenstates: (a) absorption of infrared (IR) and violet (V) photons; involving virtual states: (b) absorption of V and IR photons; (c) absorption of two V photons; (d) absorption of two IR photons.

the excited state:

$$r_{ion}(t) = \rho_{ee} \cdot \sigma_{ion} \frac{\lambda_{ion} I_{ion}(t)}{hc}. \tag{4.13}$$

With a typical value of the peak ionization intensity of about 150 mW/cm^2, we estimate $r_{ion} \approx 4$ s^{-1}. This value justifies what we anticipated in the comments to the eq. (3.32): the extremely low invasiveness, in our experimental conditions, of the photoionization in probing the excited state population. From eq. (4.13) the number of ions (per second) R_{ion}, produced within the interaction volume V, can be obtained [95]:

$$R_{ion} = n_{ee} V r_{ion} = n_0 \rho_{ee} V \frac{\sigma_{ion} \lambda_{ion} I_{ion}}{hc} \tag{4.14}$$

where $n_{ee} = \rho_{ee} n_0$ is the density of excited atoms in the beam (n_0 is the atomic density of the beam).

Unlike the process (a) treated above, the other processes shown in fig. 4.4 involve virtual laser-induced states and, as such, are extremely less probable. The ionization yield due to the process (b) is extremely small, because the

photon at energy 3.06 eV cannot populate efficiently the excited states, being detuned more than 400 nm. Also the process (c) (absorption of two IR photons) cannot appreciably contribute to the ionization, since the energy of the two photons involved is less than the ground state ionization energy. More precisely, the process (c) represents a non-resonant two-photon ionization process, whose contribution would be not negligible only at laser intensities 8-9 orders of magnitude larger than the ones used in our experiment [96]. Finally, for the same reasons we can neglect also process (d) (absorption of two V photons): with our typical peak values of ionizing intensity and a value of about 10^{-50} cm^4 s for the two-photon non resonant generalized ionization cross-section relative to $h\nu_{ion} = 3.06$ eV [97, 98], for this process we can estimate an ionization rate of about 10^{-15} s^{-1}.

4.3.1 Background/noise processes

In this conclusive section we review the contributions to the ion yield due to the interactions among the Cs atoms or Cs atoms and electrons [95]:

1. $Cs^* + Cs^* \rightarrow Cs_2^+ + e^-$: the cross-section for associative ionization has been studied [99] and found to be on the order of 10^{-18} cm^2. Since in this process the ionization radiation does not have a role, it is enough to switch off it to ascertain if the associative ionization is giving some contribution. Experimentally, we did not find any net count in the absence of the ionization radiation. Furthermore, the relatively low density ($n_0 \approx 10^8$ cm^{-3}) of the atomic beam confirms us in neglecting this contribution.

2. $Cs + e^- \rightarrow Cs^+ + 2e^-$: ionization of ground state Cs atoms due to electron-impact ionization; the electrons can be produced by the ionization laser impinging on a cesiated internal surface of the vacuum chamber or by the Cesium photoionization itself. While this effect can be relevant in experiments working with ovens and not collimated ionizing radiation, in our setup the atomic beam does not interact with the chamber walls, the Cs background vapor pressure is extremely

low in the photoionization region and the ionization laser beam is well collimated. To be sure that this contribution is negligible, in the absence of atomic beam (pressure around 10^{-8} mbar), we sent the ionizing laser beam on several internal parts of the vacuum chamber in which the photoionization is accomplished, but we could not appreciate any net count. On the other hand, the electrons can come directly from the photoionization of Cesium atoms, but the very low density of ions produced safely ensures that this contribution can be neglected.

3. $Cs^* + e^- \rightarrow Cs^+ + 2e^-$: ionization of excited atoms due to electron-impact ionization. The cross section of this reaction is about $\sigma^*_{ion} = 3 \times 10^{-15}$ cm^2 [100] and, as above, the low density of the ions produced leads to neglect this contribution. A non rigorous confirmation is obtained *a posteriori* from the ratio between the rate of this process, R^*_{ion}, and of the photoionization (reported in eq. (4.14)):

$$\frac{R^*_{ion}}{R_{ion}} = \frac{\sigma^*_{ion} j_{el}}{\sigma_{ion} j_{ion}} \approx 2 \cdot 10^{-9} \tag{4.15}$$

where $j_{ion} \approx 3 \cdot 10^{17}$ cm^{-2} s^{-1} ($I_{ion} \approx 150$ mW/cm^2, see the comments on eq. (4.13)) and $j_{el} \approx 3 \cdot 10^6$ cm^{-2} s^{-1} are the fluxes of ionizing photons and electrons, respectively. The latter has been estimated from a reasonable count rate of about 10^4 ions per second, distributed on a surface of about 9 mm^2, equal to the forefront cross-section of the ionization volume in the configuration of fig. 7.2 (a).

In conclusion, we assert that the main contribution to the ion signals we will present in chapter 7 comes from the expected two-photon, two-color photoionization process, and that the effects of the collateral ionization processes can be safely neglected.

Chapter 5

Experimental apparatus

This chapter describes the experimental apparatus that has been mounted during this work and used to produce the cold and slow atomic beam. Even if its basic scheme comes from the preexisting apparatus [22, 101], three changes have been made to the original design, that implied a complete building of the set-up:

- the substitution of the old pyramid with a new, larger, one
- the mounting of an additional "observation" stage, in which all the measurements shown in chapter 6 have been accomplished
- the mounting of a new stage in which the atomic beam is ionized in order to produce a cold ion beam; the measurements shown in chapter 7 have been shown in this stage

5.1 Vacuum system and *in-vacuo* optics

The vacuum system is constituted by a stainless steel cylinder (diameter 100 mm), terminated by a fixed CF100 flange on one side and, on the other, by a rotatable CF63 flange. In fig. 5.1 the vacuum apparatus is schematically represented. The set-up can be conceptually divided into several stages, each one devoted to a specific aim: a MOT stage, where the pyramid and the dispensers are accommodated and where the MOT is formed; a collimation

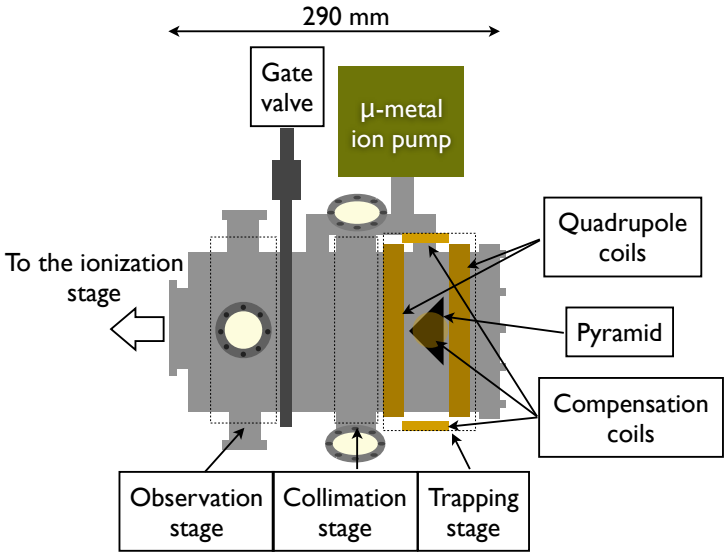

Figure 5.1: Schematic representation of the vacuum apparatus.

stage, where the atomic beam, right out of the pyramid, is collimated by means of a two-dimensional optical molasses; finally, the observation stage, not present in the old apparatus. The rotatable CF63 flange is the junction to the ionization chamber (not shown in the figure), that will be described in chapter 7. A vacuum condition of about 10^{-9} mbar is maintained in the apparatus by an ion pump (Varian, mod. *Vaclon Plus 20 Star Cell*), connected to the MOT and collimation chambers through a bypass. Its nominal pumping speed is 20 l/s and its operating current is proportional to to the internal pressure of the chamber. The ion pumps offer the advantage of absence of vibrations (important, because of the sensitivity of the laser frequency locking system), high vacuum level and vacuum maintaining also in case of electrical black-out. The stray magnetic field of the pump is screened with μ-metal shield. The vacuum is evaluated reading the current monitor on the power supply of the ion pump itself. The connection between observation and ionization stages is ensured by a gate valve, able to sustain a differential pressure of about 1 bar. The pumping in the ionization chamber relies on a turbomolecular pump (Varian, mod. *Turbo Macro Torr vt300*), with a nominal pumping speed of 300 l/s, connected in series with a membrane pump (Varian, mod. *MV2V*) with a pumping speed of 1.8 m^3/h and limit

vacuum 0.5 mbar. The vacuum in the ionization stage is monitored by an ionic gauge near the turbo pump. Finally, all the optical components and vacuum chambers are mounted on a vibration isolated table (Newport RS1000), while plastic curtains with an inner sheet of black cardboard shield acoustic noise sources, air flow and other light and noise sources due to the other running experiments.

5.1.1 MOT and collimation stage

The MOT and collimation chamber (see fig. 5.2) has eight flanges: a CF100, where the window (anti-reflection coated) for the entrance of MOT and repumping lasers is mounted; six CF40, of which four allow the passage of the collimation laser beams, one the connection with the ion pump and the last one the current cables for the dispensers. Inside the chamber there are the pyramid and the dispensers, mounted on the respective holders.

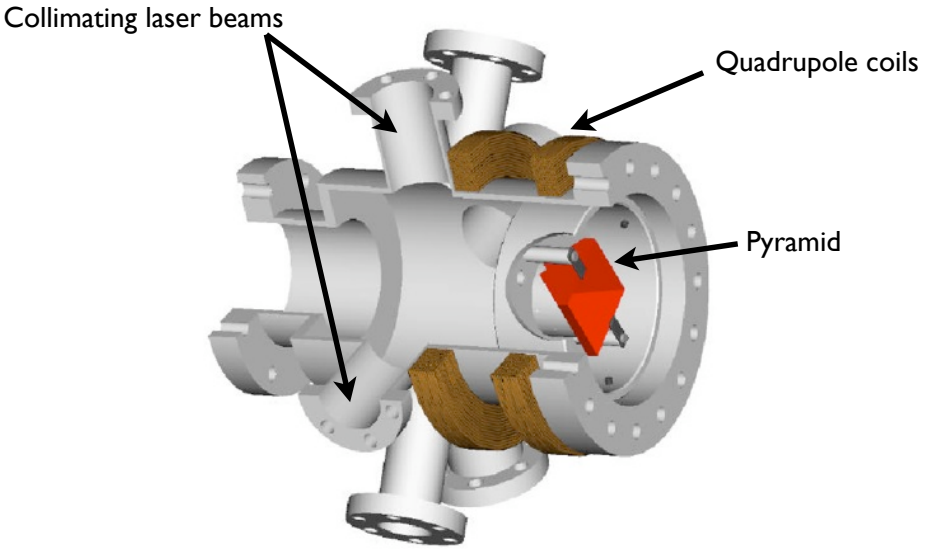

Figure 5.2: Sketch of the apparatus for the realization of the atomic funnel and for the collimation of the atomic beam.

In the old experiment the differential pumping between the chamber accommodating the pyramid and the one in which the atomic beam is transversely collimated relied on the presence of 6 holes through the wall between

the two chambers, on which the holder of the pyramid was screwed. Furthermore, the ion pump was connected directly to the collimation chamber, with the consequent impossibility to adjust the vacuum conditions in the MOT chamber. On the contrary, the bypass present in the existing setup allows an adjustment of the vacuum level in the MOT chamber through a bellows valve.

The pyramid

The main feature of our experiment is represented by the atomic source: a specific configuration of magneto-optical trap [61], called Pyramidal-MOT [63]. The name is due to the exploitation of a hollow reflective pyramid, whose internal volume is illuminated by a single, expanded and circularly-polarized laser beam. By means of the reflections on the inner surfaces of the pyramid, the atoms can stand in a configuration of radiation similar to that obtained in the traditional 6-beams MOT.

The first step in the mounting of the new apparatus was the assembly of the pyramid. The one present in the old apparatus had to be substituted, since the integrity of the highly reflective coating had been compromised by the oxidation of the Cesium (deposited on the surfaces by the vapor present in the MOT chamber) with the water vapor in the air, with which it got in touch several times during maintenance operations on the old apparatus.

The pyramid is made by an arrangement of two rectangular mirrors (with "chisel" cross sections, to enable maximum reflective surface area) arranged at 90°, and two prism-shaped pieces[1] sitting in the 90° valley, as shown in fig. 5.3. The length of the basis side is 5 cm and the assembly is held by a stainless steel mounting installed inside the chamber. This arrangement was chosen, with respect to the more simple one consisting of four identical triangular mirrors, to ensure a superior robustness and to minimize the number of cut edges that can scatter the trapping radiation, with detrimental effects on the performance of the source. The surfaces of all these optical elements are treated with highly-reflective coatings. Fundamental point, a hole (1×2 mm^2)

[1]Both the mirrors and the prisms were manufactured by *Halo Optics*, and the coating produced by *CVI*.

is left in the vertex to allow the formation of the cold atom beam [64].

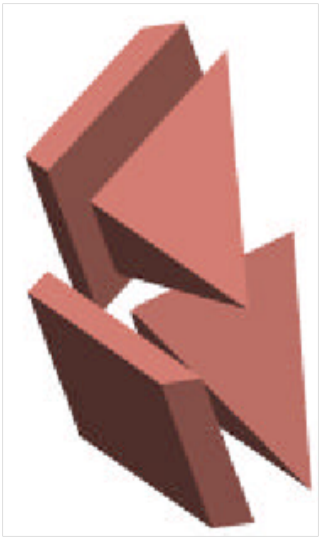

Figure 5.3: Scheme of the arrangement of prisms and mirrors that constitutes the pyramid.

The reflectivity of the inner surfaces of the pyramid have been tested, in order to check if a left-handed circularly polarized laser beam, incident at 45° on the surfaces, is reflected right-handed as required to obtain the MOT. The cross section of the incident beam was reduced, in order to probe different zones of the inner surface and to detect possible defects in the highly-reflective coating layer. The degree of circular polarization of the incident laser beam was (98 ± 1) %. We made the incident laser beam pass through a polarizing beam-splitter (a birifringent cube that splits incident light in two beams having linear orthogonal polarizations) and a $\lambda/4$ plate. Then, after reflection on the inner surface of one side of the pyramid, the beam crosses another $\lambda/4$ plate and, finally, another polarizing beam-splitter. By measuring the powers of the beams transmitted and reflected by the last cube, it is possible to infer the handness of the circular polarization of the reflected beam. We found the appearance of about 1 % of the unwanted handedness in the reflected beam, a percentage which is anyway adequate for the formation of the MOT [102].

Dispensers

The background Cesium vapor is produced by a couple of dispensers through which a continuous current flows (typically 3-4 A) and that are placed in front of the pyramid basis, parallel to the edges. The dispensers (*Saes Getters*) are constituted by a trapezoidal base stainless steel stripe (length about 8 cm, section 1 mm) containing a mixture of a few mg of Cs chromate and a non evaporable getter [103]. The passage of the electric current causes a heating of the dispenser and, above the activation temperature, a chemical reaction is started which leads to the emission of atomic Cs vapor that form the background from which the MOT is loaded. The other reaction products are trapped by the getter.

Coils

The quadrupole magnetic field for the MOT operation is generated by a pair of coils, made of 126 loops of enameled copper wire (2 mm diameter) through which, in operating conditions, currents of 4-5 A flow in opposite directions (anti-Helmholtz configuration). They are connected to separate power supplies and directly wound on the chamber. Their cross-section is 28×18 mm^2 (radial and axial directions, respectively) and the axial distance between their centers is about 4 cm .

Since it was not possible a direct measurement of the magnetic field inside the chamber, we developed a routine (based on general expressions of the magnetic field generated by a loop of wire [104]) to numerically compute the strength of the magnetic field, and its gradient, as a function of the current flowing in the coils (see section 6.1.3).

The compensation of earth and stray magnetic fields in the trapping volume relies on two pairs of coils (made of 150 loops), whose axes lie along the two directions orthogonal to the propagation of the beam. By means of these coils, it is also possible to switch between the regimes of stationary MOT and atomic funnel, shifting the zero of the magnetic field out of or onto the pyramidal axis, respectively. The loops are made of copper wire, mounted on U-shaped holders, inside which the wire is wound.

5.1.2 The observation stage

The introduction of the new observation stage satisfied the need, matured during the operation with the old apparatus, to have a part of the chamber where to accomplish measurements on the atomic beam, free from any radiation except the one of the probe laser beam. In this stage, featuring a good optical access (quantified by a geometrical numerical aperture of the AR-coated windows of 0.47), we accomplished the major part of the measurements whose results are reported in chapter 6. Moreover, the relatively long distance between this stage and the MOT stage (approximately 120 mm), allowed us to perform measurements without being concerned for the effects of stray magnetic fields, coming mainly from the trapping zone (quadrupole coils).

5.1.3 The ionization stage

The new ionization chamber represents the main change made to the set-up during this work. Its role is to accommodate the charge detection system (see fig. 5.4); it is cross shaped with six arms and it has four orthogonal flanges: two connect this stage to the observation stage and to a chamber that can be brought at atmospheric pressure. In the future development of the experiment, this chamber will be used to load the samples on which the cold ions will be deposited. Another pair is closed by windows for the laser beams. The final pair is closed by the housing for the detector and a metal sect. The housing for the detector is closed by a flange equipped with feedthrough BNCs connected to the several parts of the charge detection system that need appropriate electric potential.

5.2 Laser system

For the laser cooling the Cs atoms radiation tuned on the D_2 transition at 852 nm is used. The laser system is made of seven AlGaAs based laser diodes, of which six are mounted in *master-slave* configuration.

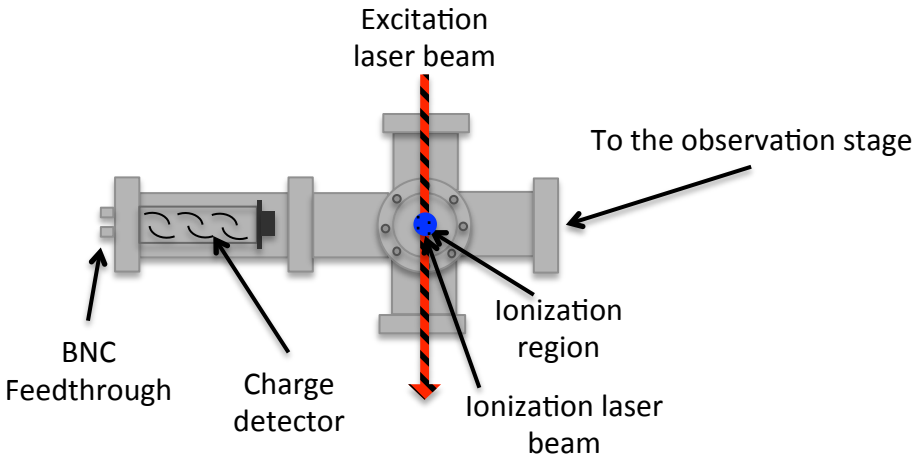

Figure 5.4: Schematic draw of the ionization chamber. In the scheme, the ionization laser beam is propagating in the direction perpendicular to the plane.

The *master* lasers, producing about 50 mW of radiation, are mounted in external-cavity configuration [105, 106] (fig. 5.5) in order to select the longitudinal oscillating mode and reduce the spectral width.

The divergence of the beam coming out of the diode chip is reduced with an anti reflection coated objective lens (*Melles-Griot*, f/8.0) and sent onto a holographic diffraction grating (*Edmund Scientific*, 1800 lines/mm), mounted in Littrow configuration, that closes the cavity. A piezoelectric transducer allows to change the tilting of the grating and the length of the cavity, with consequent tuning of the frequency on an interval of about 1 GHz, inside the 19 GHz free spectral range of the laser cavity. The astigmatism of the laser beams, due to the asymmetry of the emitting region, is corrected by pairs of anamorphic prisms to obtain circular spots. Moreover, to reduce optical feedback, each beam is sent into an optical isolator placed inside a telescope. The beam polarization configurations, necessary for the trapping and collimating operations, are obtained by means of quarter and half wavelength plates mounted on rotating holders.

The output radiation from the laser is split in two beams. One is used in the frequency stabilization (treated in section 5.2.2), while the remaining

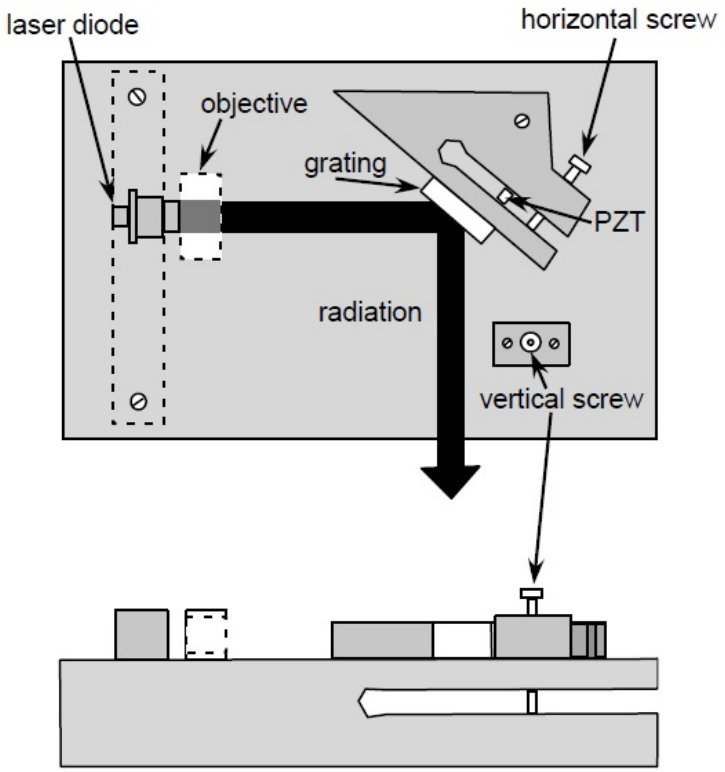

Figure 5.5: Scheme of the external cavity mount of the *master* laser.

part injects a higher power laser (*slave*), whose emission gets the spectral characteristics of the injected laser beam. The estimated spectral width of the *slave* laser radiation is below 1 MHz, with a power of about 100-150 mW.

Each one of the three couples *master-slave* provides the radiation for a specific task: trapping, collimating or exciting the atoms.

The trapping and collimating regions are also reached by the radiation of a Distributed Bragg Reflector (DBR) laser used to repump the atoms. The frequency tuning of the DBR laser is accomplished by means of the built-in thermo-resistance and Peltier element.

5.2.1 Current and temperature stabilization of the *master* lasers

The diodes are mounted on a holder of german silver (alloy of 62 % Cu, 18 % Ni and 20 % Zn), chosen for its elasticity, important for the mechanical adjustment of the mounting, and for the good thermal conductivity. The holder is, in fact, in thermal contact with a big parallelepiped of aluminum acting as thermostat.

The thermal contact between the two elements is provided with two Peltier connected in parallel; a temperature transducer (Analog Devices, mod. *AD590*), in thermal contact with the holder, is connected to a servo control circuit that supplies the Peltier in order to keep the temperature at the set level with an accuracy of 0.01 K. The external cavity is then placed in a plexiglass container coated with a sound and thermal insulating material which, in turn, is covered with a foil sticker.

Furthermore, the lasers are current stabilized (with a nominal accuracy of a tenth of mA) and equipped with safety circuits against overvoltage and current surges.

5.2.2 Frequency stabilization of the *master* lasers

The frequency stabilization follows a standard technique of frequency locking on the peaks of the saturated absorption signal obtained in a reference Cs cell

(shown in fig. 5.6). The general scheme of the frequency locking apparatus is

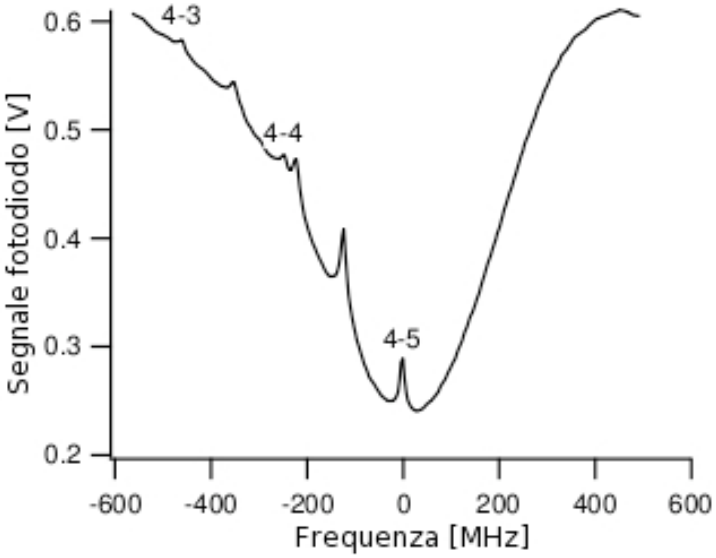

Figure 5.6: Saturated absorption signal of the D_2 transition in Cs vapor contained in a cylindrical room temperature cell.

shown in fig. 5.7. After passing through an optical isolator and a couple of anamorphic prisms, the radiation from the diode laser is split in two beams that are eventually superposed (propagating in opposite directions) in the Cs cell. One of these beams passes through an acousto-optic modulator (Crystal Technology) connected, through an RF amplifier, to a voltage controlled oscillator (VCO). The VCO plays the double role of detuning and modulating the frequency of the radiation: the detuning is needed to trap and collimate the atoms, while the modulation gives the possibility to lock the radiation frequency. In order to do this, a small amplitude, sinusoidal modulation at a frequency of 60 kHz is applied to the control voltage of the VCO, modulating the shift of the laser frequency. This modulation is then transmitted to the output signal of the photodiode that detects the transmitted intensity of the probe laser beam through the Cs cell. The signal of the photodiode is then sent to a lock-in amplifier that generates the error signal. This signal, after passing through an integrator, is applied to the laser-cavity piezoelectric, closing the feedback loop.

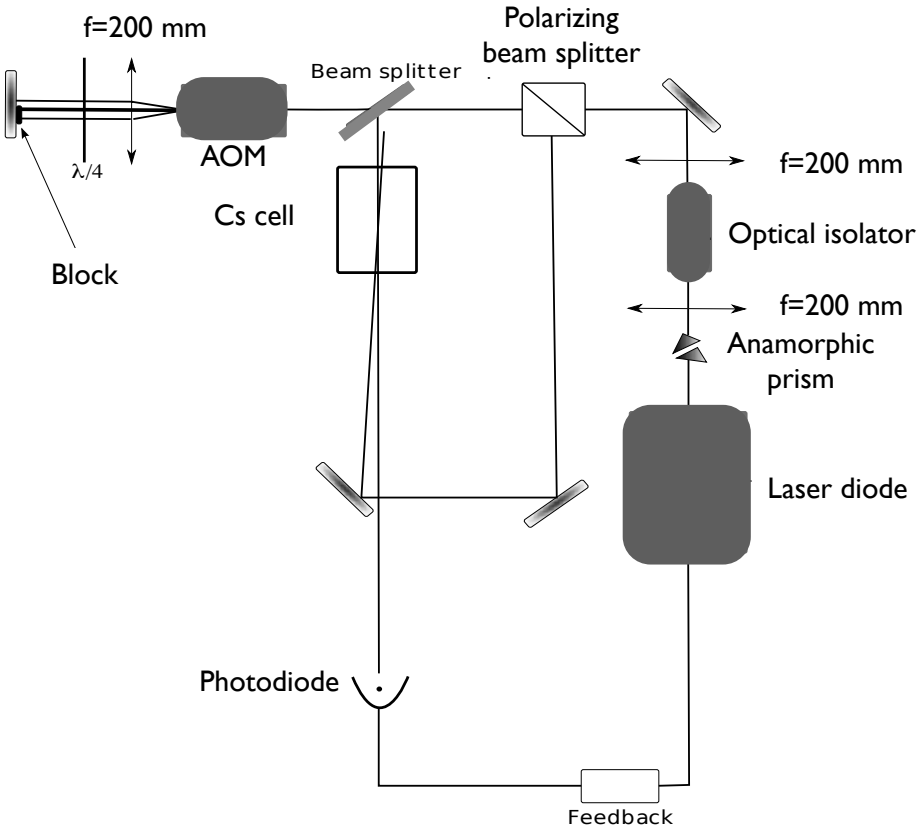

Figure 5.7: Schematic representation of the frequency locking apparatus. The beam out of the laser is split in two parts by the polarizing beam splitter. One beam passes through the AOM, detuning and modulating its frequency, and then is sent into the Cs cell. The other beam is directly sent to the photodiode, through the Cs cell.

5.2.3 Ionization laser

The ionization laser we used is a diode laser with active medium GaN (made by Nichia), produced by Oxxius. It was already available in our lab, and it is internally stabilized in temperature and current. This laser does not have any mechanism to control the output frequency, it emits radiation at 405 nm and the maximum power is about 50 mW. However, the power effectively exploited after passing through several optical elements is less than 20 mW. Finally, the output power can be modulated by sending suitable TTL signals to a BNC connector on the power supply of the laser.

5.3 Optical paths

We conclude this chapter with a general overview of the optical paths. fig. 5.8 shows how MOT and repump laser beams are superposed and enlarged with a telescope to a FWHM of about 4 cm. This size has been chosen to be slightly

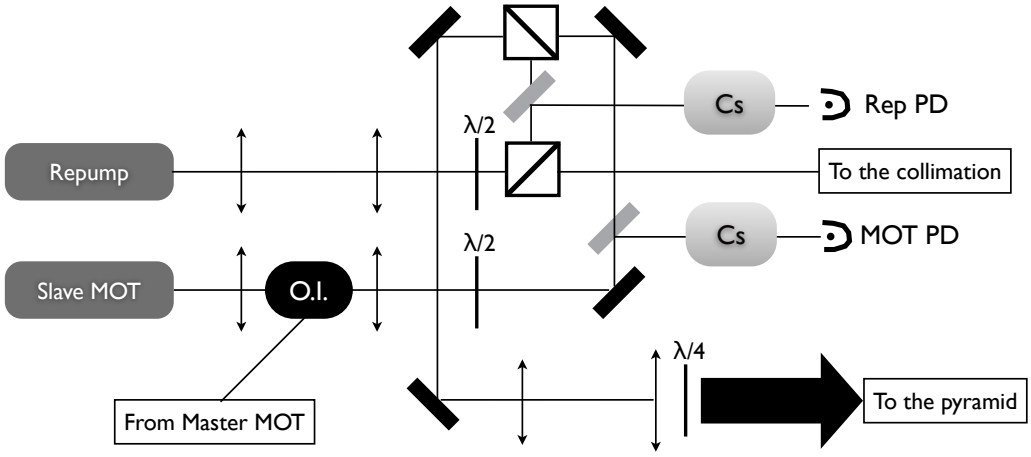

Figure 5.8: Schematic optical paths of the trapping and repumping beams. The radiation from the *master* MOT reaches the *slave* laser through an optical isolator (O.I.) with a lateral input. The beams from the MOT *slave* and repump lasers are superposed on a polarizing cube, enlarged with a telescope and then sent into the pyramid.

less than the size of the pyramid base, in order to avoid the scattering from

the edges of the mounting. The typical power of the trapping beam is 90 mW, corresponding to a Rabi frequency of around 2.5 Γ, while the typical detuning from the atomic resonance is about -12 MHz ($\delta = -2.3\ \Gamma$). The collimating laser beams are superposed to the remaining repump radiation (see fig. 5.9 (a)) and sent onto the atomic beam in two orthogonal directions (fig. 5.9 (b) and (c)).

After passing through a cylindrical telescope (consisting of two lenses with focal lengths $f = -40$ mm and $f = 150$ mm), the collimating laser beam cross-sections are about 0.5×3 cm^2 (FWHMs), with the longest side along the atomic beam propagation. The typical values of power and detuning are about 110 mW (corresponding to a Rabi frequency of 7.4 Γ) and -7.5 Γ, respectively. With these parameters, we can easily estimate the two-level atom spontaneous emission rate $\Gamma_{scatter}$ during the interaction with the collimating laser beams:

$$\Gamma_{scatter} = 0.16\ \Gamma, \tag{5.1}$$

corresponding to one spontaneous emission every $2 \cdot 10^{-7}$ s. Because of the low average longitudinal velocity, the atom-radiation interaction time is $\tau_{coll} \approx 2$ ms, so that the number of spontaneous emissions undergone by an atom in the collimation stage is roughly given by $\tau_{coll}\Gamma_{scatter} \approx 10^4$. This results in a quite efficient transverse cooling process, as we will see in section 6.2.

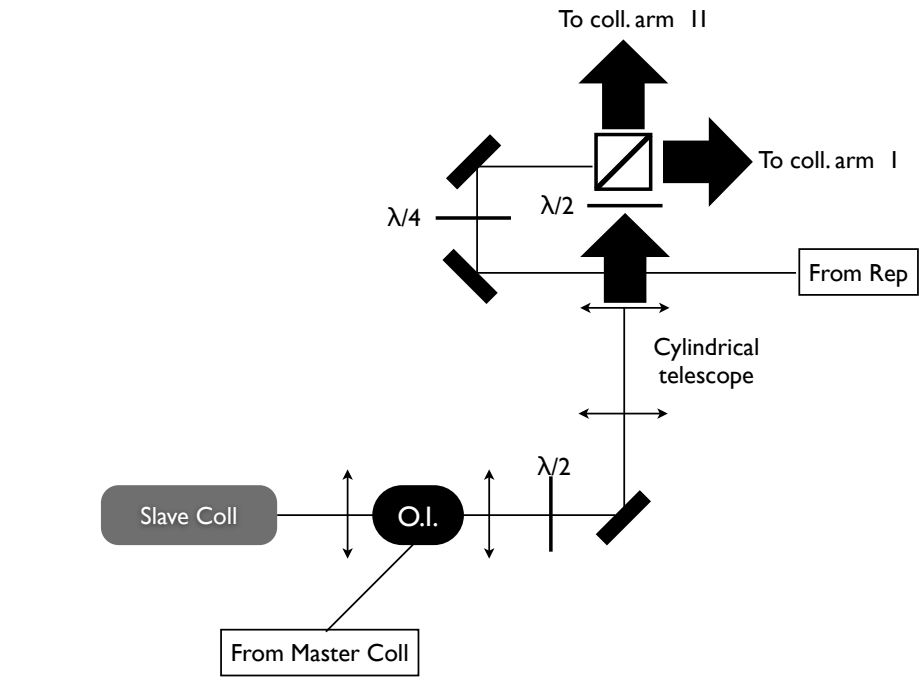

(a)

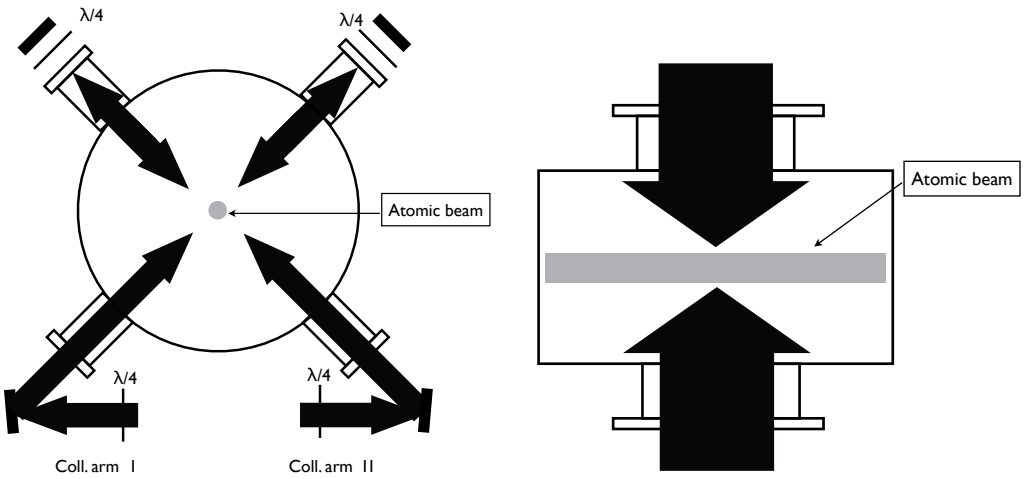

(b) (c)

Figure 5.9: (a) Schematic optical paths for the collimating and repumping laser beams. (b) and (c) front and side views, respectively, of the collimation stage.

Chapter 6

Atomic beam: properties

This chapter reports the features of our slow and cold atomic beam, in terms of number of particles per unit time and spatial distribution of the beam intensity. In section 6.1 we show how we determined the density of the atomic beam, and how we maximized it, exploiting its dependence on easily controllable parameters like trapping beam intensity and detuning, quadrupole magnetic field gradient and dispenser current. We then show, in section 6.2, the efficiency of the collimation stage on the atomic beam, detected by means of a scientific CCD camera collecting the fluorescence excited by a resonant probe beam. We continue with section 6.3, that illustrates the outcomes of the Time Of Flight (TOF) measurements accomplished to get the average value and spread of the atomic longitudinal velocity distribution. Finally, the transverse intensity distribution of the atomic beam in the ionization region is reported, again as measured by means of fluorescence imaging techniques.

6.1 Density

The density of the atomic beam has been determined through absorption spectroscopy measurements accomplished in the observation stage, that is the section of the vacuum chamber more close to the ionization stage and that provides enough optical access. The atomic beam is intersected orthogonally by a resonant laser beam whose frequency is swept around the hyperfine

transition $F_g = 4 \rightarrow F_e = 5$ (the strongest of the D_2 fine structure manifold, accessible by our lasers), sending a triangular waveform voltage to the piezoelectric crystal connected to the diffraction grating that closes the laser cavity.

The probe laser beam is linearly polarized along the atomic beam propagation direction, and to accomplish the measurements shown in the following a power of 0.3 μW on a cross section (FWHM) of 800 μm (for a peak intensity of about 0.04 mW/cm^2) has been used. Furthermore, to avoid optical pumping phenomena (taking place also at extremely low excitation intensities, see chap. 7) the probe is superposed to a repumping laser beam. The size of the laser beam is much smaller than the transverse atomic beam dimension in order to minimize the detection of light that has not interacted with the atoms. Since the transverse intensity distribution of the atomic beam is not flat, the absorption signal has been maximized translating the laser beam parallel to itself until the maximum absorption has been detected. The transmitted radiation is directed onto a photodiode (mod. DET 110A *Thorlabs*); furthermore, a small fraction of the probe beam is withdrawn before intersecting the atomic beam and sent directly to an identical photodiode: during the data analysis, this second signal is used to remove possible baselines in the spectrum.

To increase the S/N ratio, the signal from the photodiode is sent to an amplifier (mod. TM502A by *Tektronix*, input impedance 1 MΩ, associated capacity 47 pF, gain 10^3), provided with input filters.

The signals have been acquired with the oscilloscope *LeCroy* 9384 in *sequence* mode; this allowed us to get a reliable statistics of the absorption curves in a reasonable acquisition time. Typically 1000 sweeps for 20 ms each one are acquired, for a total measurement time of 20 s. All the error bars shown in the following represent the standard deviations of the measurements samples.

In fig. 6.1 we have a typical absorption curve. To determine the 8 MHz width, the signal has been fitted with a Lorentzian function, neglecting the convolution with a Gaussian that, in principle, should be considered due to the transverse velocity spread. This is justified because, as we will see in sec

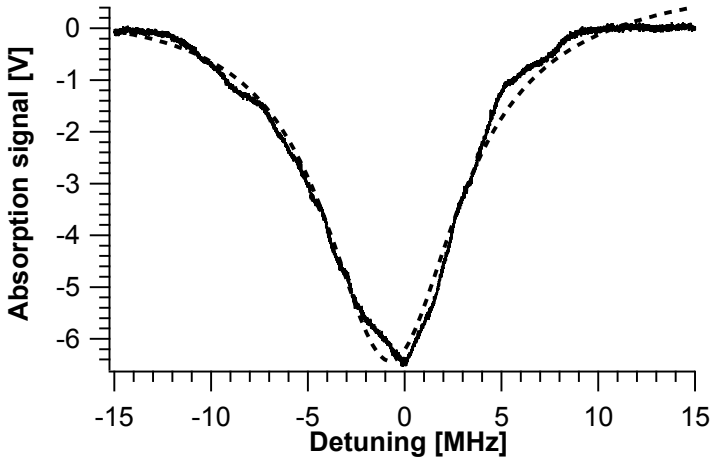

Figure 6.1: Absorption signal of the atomic beam in the observation stage. The vertical axis reports the amplified ($\times 10^3$) signal of the photodiode collecting the transmitted radiation. The DC signal on the photodiode, without atomic beam, is about 140 mV. The width of the absorption curve obtained from the fit, FWHM=8 ± 4 MHz, is compatible with the natural linewidth, within the experimental uncertainty. The accuracy of the calibration procedure has been limited by the frequency resolution of the interferometer, in conjunction with an unavoidable frequency jitter due to the piezo instability. This explains the quite large uncertainty we can reasonably estimate on the measured 8 MHz of linewidth for the spectrum in fig. 6.1.

6.2, the spread of the transverse velocity distribution (FWHM $\leq$ 10 cm/s) would be responsible for a line broadening of about 2 MHz, less than the 5.22 MHz natural width. The horizontal axis of the absorption spectrum has been independently calibrated in frequency, sending the probe radiation into a Fabry-Perot interferometer (*Thorlabs*, mod. SA200-5B, resolution 7.5 MHz) and measuring the variation of the frequency with the voltage sent to the piezoelectric. The accuracy of the calibration procedure pushed us to safely use large uncertainty values, which perhaps overestimate the error.

The atomic density has been obtained from the absorption spectra according to the following model. The atomic density can be written as:

$$n(x,y) = n_0 \exp\left(-\frac{x^2}{w_{at,x}^2}\right) \exp\left(-\frac{y^2}{w_{at,y}^2}\right) \tag{6.1}$$

where n_0 is the peak atomic density and $w_{at,x}$ and $w_{at,y}$ are the transverse dimensions of the atomic beam, propagating in the z direction. Similarly, the laser intensity (the laser beam propagates in the y direction) reads:

$$I(x,z) = I_0 \exp\left(-\frac{x^2}{w^2}\right) \exp\left(-\frac{z^2}{w^2}\right). \tag{6.2}$$

where $w = 480$ μm. Integrating:

$$\int_{I_{inc}}^{I_{trasm}} \frac{dI(x,\ z)}{I(x,\ z)} = -\int_{-\infty}^{+\infty} n(x,\ y)\sigma_{abs} dy \tag{6.3}$$

with $\sigma_{abs} = 2.3 \cdot 10^{-9}$ cm^2 (absorption cross section for the D_2 line and π polarized radiation [54]), we obtain the expression for the peak atomic density:

$$n_0 = -\frac{1}{w_{at,y}\sqrt{\pi}\sigma_{abs}} \log\left(\frac{I_{trasm}}{I_{inc}}\right). \tag{6.4}$$

Exploiting the value $w_{at,y} = 1.5$ mm for the atomic beam transverse size in the observation stage, obtained imaging the fluorescence spot generated in the intersection between atomic beam and a resonant orthogonal standing wave, we calculate a typical peak atomic density of about $(8 \pm 2) \times 10^7$ cm^{-3}. Since n_0 depends on the propagation length of the radiation through the laser beam,

the orthogonality between probe and atomic beam has been ascertained by putting two screens with small holes in the centers on the ingoing and outgoing windows of the observation chamber, and then maximizing the transmission of the laser beam. The departure from the orthogonality between atomic and probe beams can be estimated from $\arctan(d/D) \leq 1°$, where d=1 mm is the diameter of the holes and D=154 mm the distance between the two windows of the chamber.

Since one has to be careful not to saturate the atomic transition, in order to have faithful values of the atomic density we performed a preliminary measurement of the relative absorption as a function of the intensity of the probe laser beam; the results, shown in fig. 6.2, show the expected decrease of the absorption (quantified by the logarithm of the ratio between transmitted and incident radiation power), due to the saturation of the transition. In

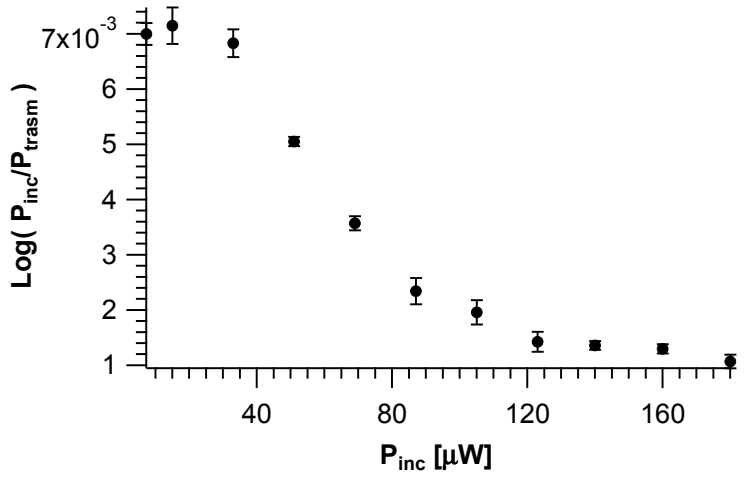

Figure 6.2: Absorption dependence on the probe beam power. The vertical axis reports the logarithm of the ratio between the transmitted and incident probe laser power.

the following we report the dependence of the relative absorption on several experimental parameters, an investigation we carried on to find the operative conditions which maximize the atomic beam density.

6.1.1 Density as a function of trapping laser detuning

In fig. 6.3 the variation of the atomic density with the trapping laser detuning with respect to the T45 atomic resonance frequency is shown. The collimation stage is off. We can note that the trapping laser frequency which maximizes

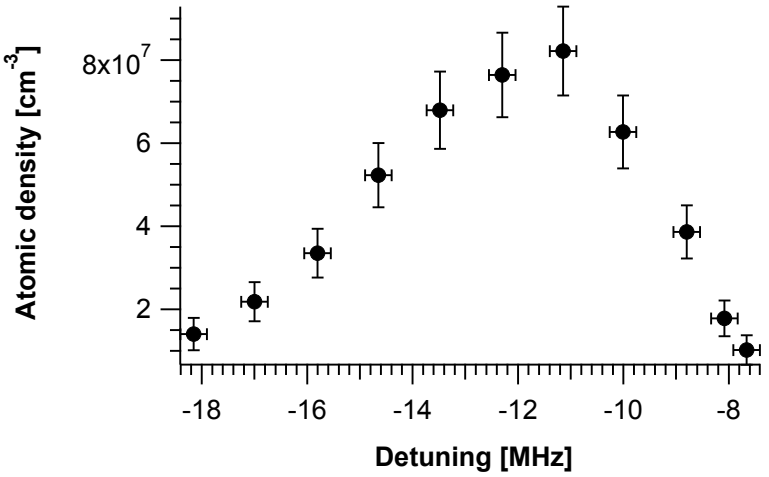

Figure 6.3: Dependence of the atomic beam density on the detuning of the trapping laser beam, with the collimation stage off. Operating parameters: $I_{MOT} = 10$ mW/cm^2, $b = 25$ G/cm.

the atomic beam density is detuned -2.3 Γ from the cycling T45 transition. It is known [107] that this detuning is larger than the one maximizing the number of atoms in the MOT. Probably this difference arises from the heating and, in case of intensity unbalances, the deflection of the atomic beam leaving the trap, due to the transverse laser beams reflected by the inner surfaces of the pyramid. Since the scattering rates, on which these deleterious effects depend, increase at lower detunings, the tendency of the atomic funnels to operate at these somewhat larger (absolute values) detunings can be explained.

6.1.2 Density as a function of trapping laser intensity

In fig. 6.4 how the measured atomic beam density depends on the trapping laser beam intensity is shown. The density increases with the radiation

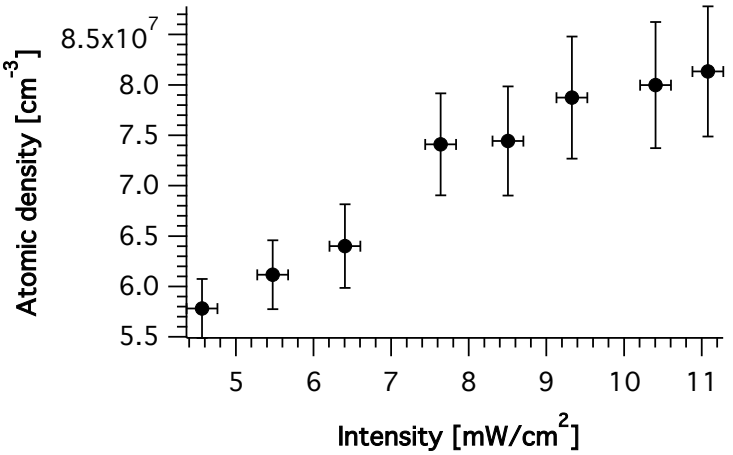

Figure 6.4: Dependence of the atomic beam density on the intensity of the trapping laser beam. Operating parameters: $\delta_{MOT} = -12$ MHz, $b = 25$ G/cm.

intensity and, in the range of powers we explored, we did not observe any saturation. A plateau in the high intensity regime would be expected, due to the saturation of the cooling transition and the balance between capture and funneling rates undergone by the atoms.

6.1.3 Density as function of magnetic field gradient

The magnetic field conditions in the MOT can be varied acting on the current flowing in the quadrupole coils. In fig. 6.5 the dependence of the atomic density on the magnetic field gradient is shown. Analogously to the dependence on the detuning, also the trend of fig. 6.5 can be interpreted in terms of the competition between atomic capture and channeling, processes that are maximized for an optimal value of the magnetic field, at a certain value of the trapping laser beam detuning.

Since we could not measure directly the magnetic field in the MOT region, the magnetic field gradient has been computed numerically. For this we exploited the general expressions of the radial B_r and axial B_z components of the magnetic field generated in the position $(r,\ z)$ by the $(m,\ n)^{th}$-loop

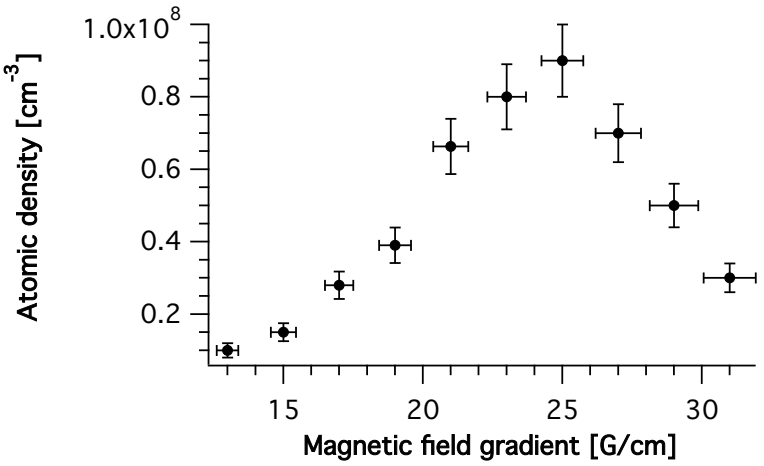

Figure 6.5: Dependence of the atomic density on the magnetic field gradient. Operating parameters: $I_{MOT} = 10$ mW/cm^2, $\delta_{MOT} = -12$ MHz.

(see fig. 6.6) of a coil [104]:

$$
\begin{aligned}
B_r(r,\ z) &= (z - z_n)\frac{I\mu_0}{2\pi}\frac{1}{\sqrt{(r + r_m)^2 + (z - z_n)^2}}\cdot \\
&\cdot\left(-\mathrm{K}\left(\frac{4r_m r}{(r_m + r)^2 + (z - z_n)^2}\right) + \right. \\
&\left. + \frac{r_m^2 + r^2 + (z - z_n)^2}{(r_m - r)^2 + (z - z_n)^2}\mathrm{E}\left(\frac{4r_m r}{(r_m + r)^2 + (z - z_n)^2}\right)\right) \\
B_z(r,\ z) &= (z - z_n)\frac{I\mu_0}{2\pi}\frac{1}{\sqrt{(r + r_m)^2 + (z - z_n)^2}}\cdot \\
&\cdot\left(\mathrm{K}\left(\frac{4r_m r}{(r_m + r)^2 + (z - z_n)^2}\right) + \right. \\
&\left. + \frac{r_m^2 - r^2 - (z - z_n)^2}{(r_m - r)^2 + (z - z_n)^2}\mathrm{E}\left(\frac{4r_m r}{(r_m + r)^2 + (z - z_n)^2}\right)\right)
\end{aligned}
$$

where I is the current flowing in the coil, r_m and z_n the radial and axial positions of the loop, while $\mathrm{K}(u)$ and $\mathrm{E}(u)$ represent elliptic integrals of first and second kind, respectively. The total magnetic field has been obtained summing on all the loops constituting the coil.

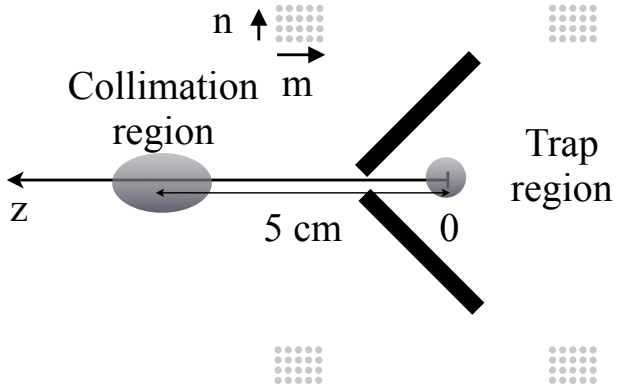

Figure 6.6: Schematic vertical cross-sectional draw of the relative positions of the quadrupole coils, the trapping and the collimation regions. The latter are shown by the gray circle and oval, respectively.

The axial component of the magnetic field and its gradient, computed on the axis and for a typical current of 4.5 A, are shown in fig. 6.7 (a) and (b), respectively. We note (this remark will be useful in sec. 6.2) that in the collimation stage (approximately at 5 cm on the z axis, see fig. 6.6), there is a relatively strong longitudinal magnetic field (the transverse component is negligible, as it can be seen in fig. 6.7) of about 40 G.

6.1.4 Density as a function of dispenser current

We completed the characterization of the atomic beam density dependence on the experimental parameters varying the dispenser current. The trend, shown in fig. 6.8, reveals an increase of the atomic density until about 4.5 A, beyond which the atomic beam becomes less dense. The reason is clear: when the background atomic density increases, the collisional rate between cold and background atoms balances the capture rate, preventing a further increase and eventually decreasing the atomic beam density.

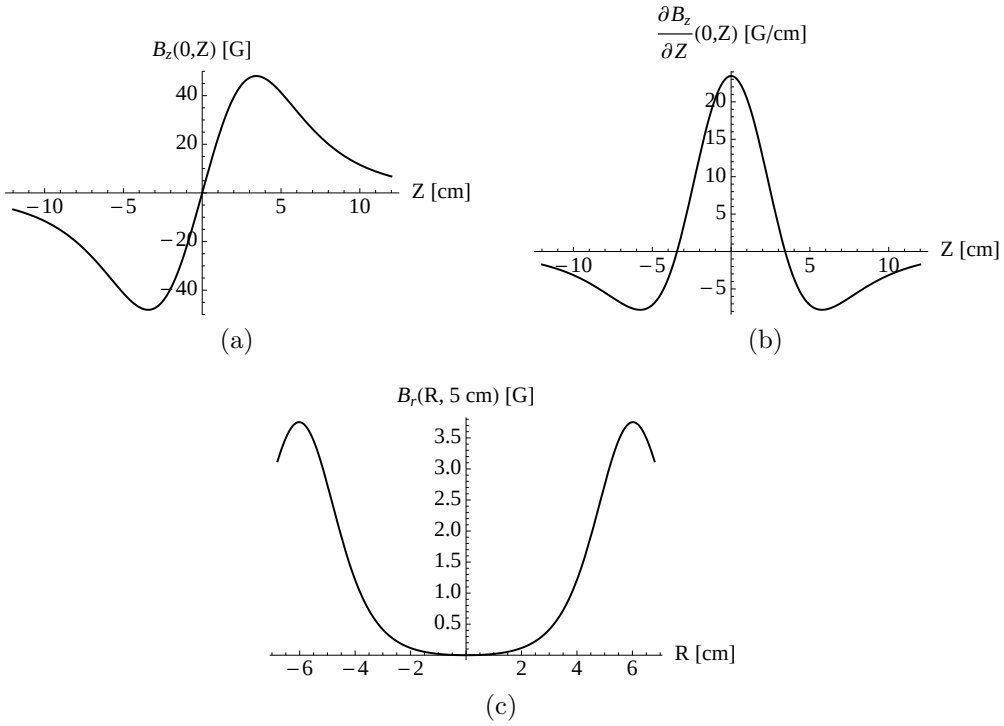

Figure 6.7: Results of the magnetic field calculation for two coils in anti-Helmholtz configuration. (a) Axial component of the magnetic field, computed on the axis; (b) Gradient of the axial component of the field, computed on the axis; (c) Radial component, computed in the collimation region. The current in the coils is 4.5 A; the zero of the longitudinal axis is midway between the coils, while the zero of the radial axis is in the center of the coils.

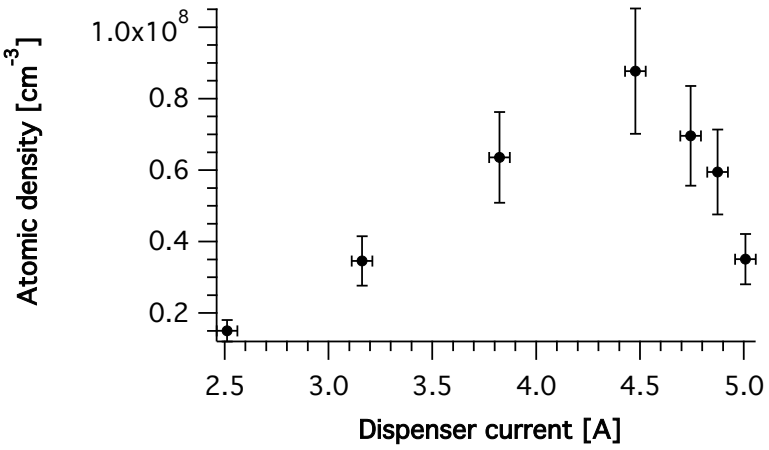

Figure 6.8: Atomic density as function of the dispenser currents.

6.2 Divergence

The divergence of the atomic beam coming out of the pyramid is reduced by means of a two-dimensional collimation stage, whose scheme has been already shown in fig. 5.9. A visual evidence of the efficacy of the collimating radiation on the atomic beam has been obtained, in the ionization stage, detecting the fluorescence spot at the intersection between a resonant standing wave and the atomic beam with a scientific CCD camera (*Princeton Instruments*). The images obtained with and without the collimation beams are shown in fig. 6.9 (a) and (b), respectively. The corresponding transverse intensity profile, shown in fig. 6.9 (c), shows an approximately ten-fold increase in the peak beam intensity, due to the presence of the transverse optical molasses. We remark that the images in fig. 6.9 refer to one single position of the probe laser beam. Translating in the vertical direction the probe beam, we obtained the three-dimensional intensity distribution of the atomic beam, which will be presented in section 6.4.

By means of the spatial calibration of the CCD camera, we have obtained a FWHM of the atomic beam in the ionization stage $D = 4.0 \pm 0.5$ mm. Knowing the FWHM $d = 2.4 \pm 0.5$ mm, measured according to the same technique in the observation stage, and the distance between this point and

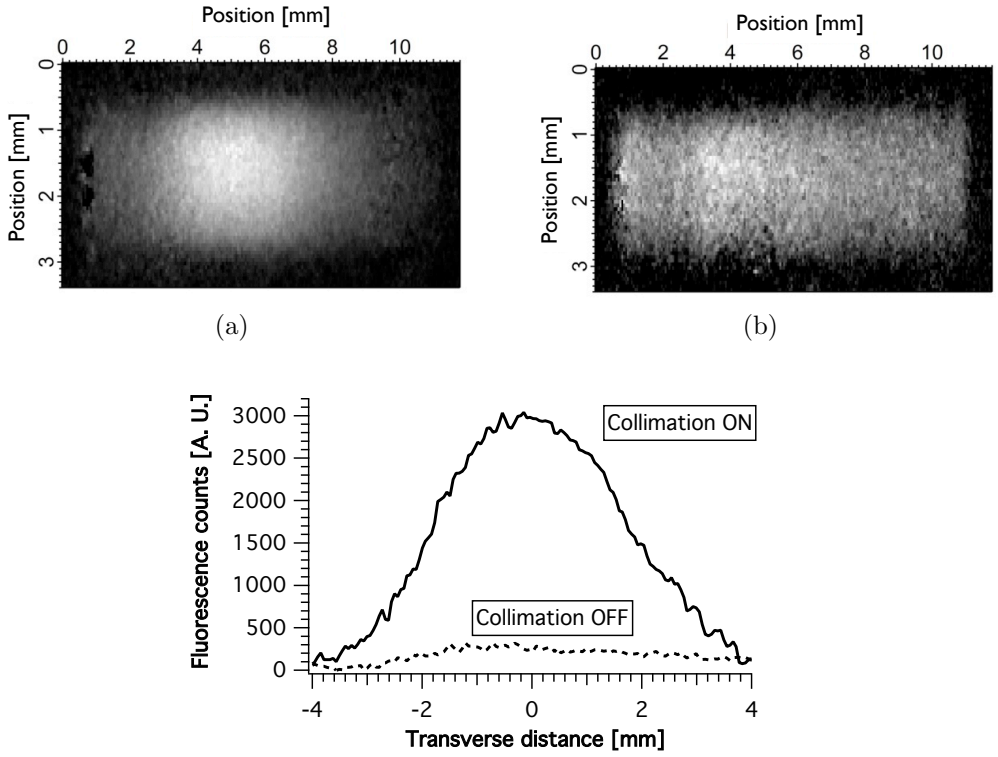

Figure 6.9: Images, acquired with a spatially calibrated CCD camera, of the fluorescence spot in the intersection between the atomic beam (propagating in vertical direction) and a resonant standing wave (in horizontal direction) (a) with and (b) without the collimating laser beams. Note that the dynamical range is not the same for the two images. (c) Corresponding transverse intensity profiles (computed on the peak fluorescence intensity and integrated on 0.1 mm in the profile normal direction) obtained from (a) and (b). The almost ten-fold increase of the peak atomic density due to the action of the collimating radiation is evident. From the line profile with the collimation on we obtain a FWHM=4 ± 0.5 mm for the atomic beam in the ionization stage.

the ionization stage ($L = 220$ mm), with a simple geometrical argument we obtain a full divergence angle:

$$\theta = 2 \arctan\left(\frac{D-d}{2L}\right) \approx 7 \text{ mrad.} \tag{6.5}$$

From the uncertainties on the values of the distance L and of the transverse sizes d and D, an estimated uncertainty of ± 1 mrad follows. Using the average longitudinal velocity $\langle v_l \rangle = 12$ m/s (see sec. 6.3), we obtain the transverse temperature $T_{trasv} = M/k_B \cdot \Delta v_{trasv}^2 = M/k_B \cdot (\theta \cdot \langle v_l \rangle)^2 \approx 125$ μK, Doppler temperature for Cesium [54]. We finally remark that it was not possible to decrease the divergence exploiting phenomena of sub-Doppler cooling. We believe the reason lies in the relatively strong magnetic field present, as we remarked in section 6.1.3, in the collimation stage. This is confirmed by the literature, where the inhibiting effects of the magnetic field on the sub-Doppler cooling [108, 109] are well known.

6.3 Average and spread of the longitudinal atomic velocity distribution

Time Of Flight (TOF) measurements have been performed to establish the main features (average and FWHM) of the velocity distribution in the atomic beam. The configuration is shown in fig. 6.10. An intense plug laser beam, placed in proximity of the vertex of the pyramid, deflects the atomic beam. By means of an AOM (*Crystal Technology*, mod. 3110-120), connected to an RF switch (*Mini Circuits*, mod. M2P2T-18-12), the laser beam can be gated off for a variable time interval (we investigated time intervals ranging between 180 μs and 900 μs). When the plug beam is gated off, it allows only a short bunch of atoms to travel to the probe region, located 90 mm downstream, in the observation stage. The fluorescence of the atoms as they cross a probe laser beam is detected by a photomultiplier. In order to detect the weak fluorescence of short atom bunches, a mechanical shutter has been mounted on the trap laser beam, in order to remove the diffuse light in the

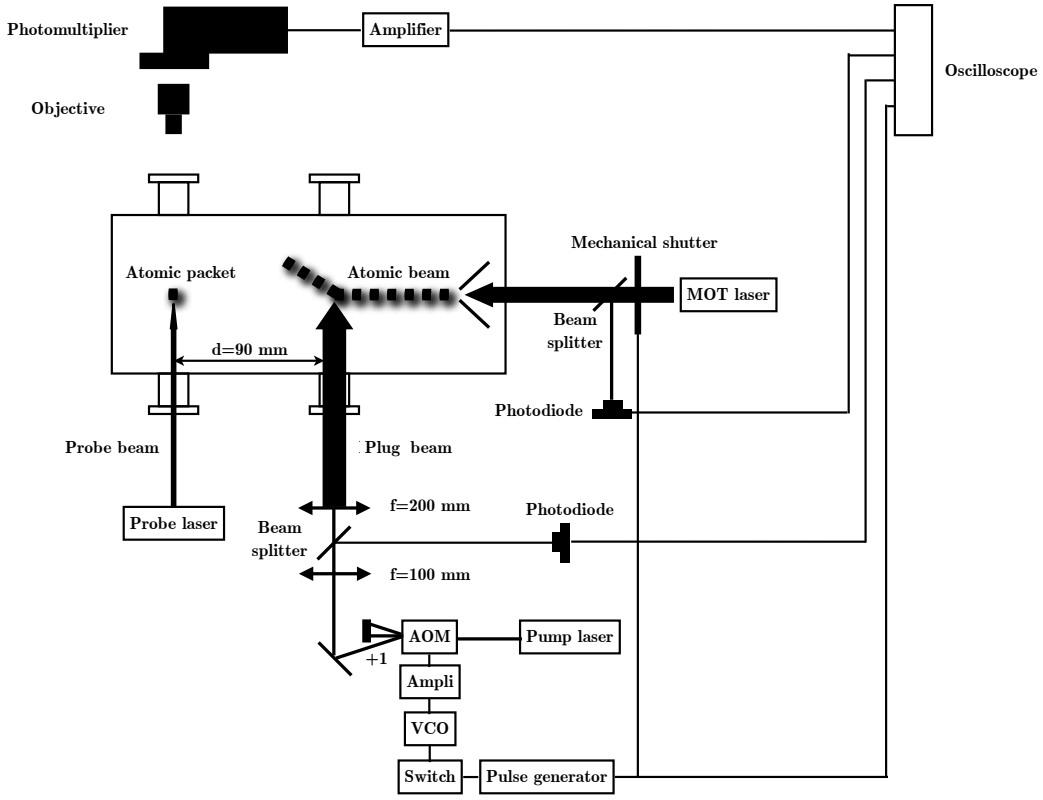

Figure 6.10: Experimental set-up used for the TOF measurement.

vacuum chamber and the atom bunch fluorescence caused by the fraction of MOT radiation passing through the apical hole of the pyramid. An example of the timing used in this measurements is shown in fig. 6.11. The trace in fig. 6.11 (a) represents the signal of the photodiode observing the switching of the plug laser beam; in this case the plug laser beam is gated off for 900 μs. After about 3 ms (see fig. 6.11 (b)) also the trap laser beam is switched off. Finally, in fig. 6.11 (c) the photomultiplier signal, due to the passage of the atom bunch through the probe beam, is shown.

The travel time of the atom bunch yields the average velocity of the atoms, whereas the width of the fluorescence signal can be used in determining the spread of the longitudinal velocity distribution.

The signal in fig. 6.11 (c) has been fitted according to the model function:

$$g(t) = \frac{A}{t^2} \exp\left(-\pi A^2 \left(\frac{1}{t} - \frac{1}{\bar{t}}\right)^2\right). \tag{6.6}$$

where A and $\bar{t} \equiv d/\bar{v}$ (d flight distance and $\bar{v}$ average longitudinal velocity) are the fit parameters.

The eq. 6.6 is obtained from:

$$f(v)dv = g(t)dt, \tag{6.7}$$

in which $v = d/t$ and a Gaussian atomic velocity distribution is assumed:

$$f(v) = \frac{1}{\sqrt{\pi}\Delta v} \exp\left(-\left(\frac{v - \bar{v}}{\Delta v}\right)^2\right). \tag{6.8}$$

The average $\bar{v}$ and width Δv of the longitudinal atomic velocity distribution are related to the fit parameters $\bar{t}$ and A by:

$$\bar{v} = \frac{d}{\bar{t}} \tag{6.9}$$

$$\Delta v = \frac{d}{\sqrt{\pi}A} \tag{6.10}$$

Furthermore, it is possible to show [110] that, given the diameter D of

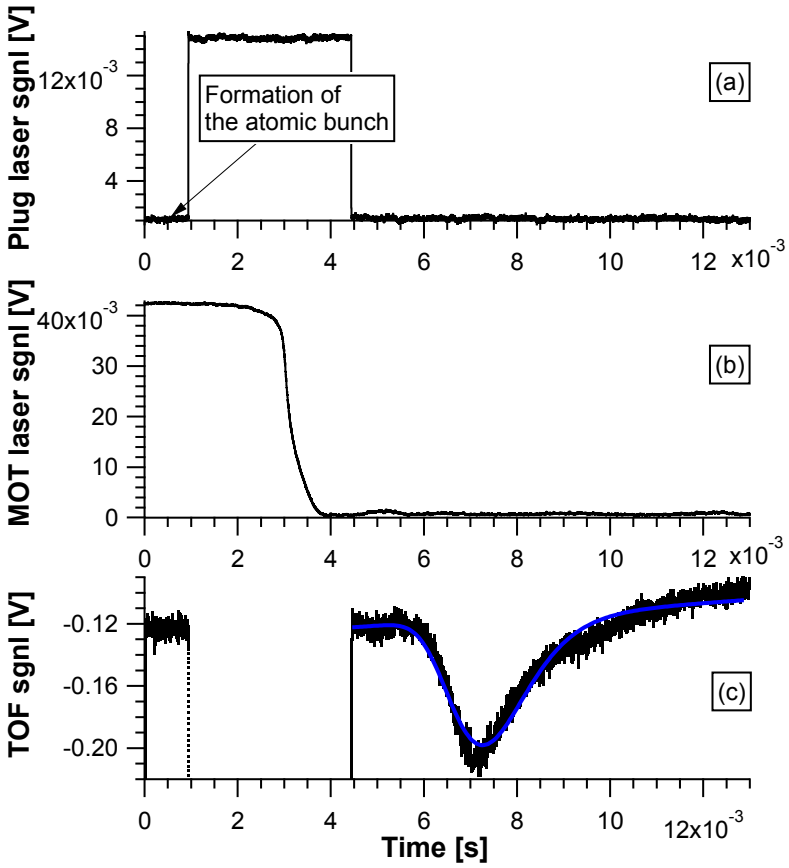

Figure 6.11: Timings used in the TOF measurements on the atomic beam. (a) Signal of the photodiode observing the plug laser beam. (b) Signal of the photodiode observing the trap laser beam, switched off by a mechanical shutter. (c) Relevant part of the signal of the photomultiplier detecting the fluorescence of the atom bunch, passing through the probe laser beam. The atom bunch is formed when the plug laser beam is switched off (and the photodiode signal (a) is about zero) between 0 and 900 μs. In this interval, the MOT laser beam is on (trace (b)) and the photomultiplier (c) detects a background signal of about -0.12 V. After 900 μs, the plug laser beam is switched on until about 4.5 ms to block further atoms of beam. Switching on the plug beam increases the radiation scattered inside the vacuum chamber, and the signal of the photomultiplier (c) jumps to a level not shown in the graph. In the meantime, at 3 ms the mechanical shutter switches off the MOT laser beam (at about 5 ms we can note a small local increase in trace (b) due to a "bounce" of the shutter blade). Finally, switching off, at about 4.5 ms, the plug beam, allows to detect the fluorescence atomic bunch (at about 7 ms) in dark conditions.

the probe laser beam, the distance d between the points in which the atomic pulse is created and detected, the time interval δt during which the atomic pulse is formed, the resolution of the TOF measurement is given by:

$$\frac{\delta v}{v} = \frac{D}{d} + \frac{\bar{v}\delta t}{d}. \tag{6.11}$$

The minimum resolution we achieved, with $\delta t = 180$ μs, is 0.4 m/s. A further decrease of δt reduced the number of atoms in the bunch to a level that the fluorescence signal was not detectable. With $\delta t = 180$ μs we measured an average longitudinal velocity of 12.1 ± 0.2 m/s, and a FWHM of 1.4 ± 0.2 m/s. The uncertainty has been estimated as half of the resolution.

6.4 Intensity distribution in the ionization stage

Finally, we investigated the spatial variation of the atomic beam intensity in the ionization stage. The scheme, already commented in sec. 6.2, is depicted in fig. 6.12: a CCD camera (observing in the $-\hat{x}$ direction) collects the fluorescence excited by a probe (propagating in the $\hat{y}$ direction) orthogonal to the atomic beam (propagating in the $\hat{z}$ direction). The probe can be moved in the vertical direction, to obtain several images of the fluorescence spot at different probe heights X. In this way the size and shape of the atomic beam cross-section is obtained.

Using the expression of the atomic density $n(x, y)$, reported in eq. 6.1, and of the excited population fraction for a two-level system, $\rho_{ee}(x - X, z)$

$$\rho_{ee}(x - X, z) = \frac{I(x - X, z)}{2I(x - X, z) + I_{sat}} \tag{6.12}$$

where $I(x - X, z)$ is the intensity of the laser beam centered at height X (see eq. (6.2)), the image of the fluorescence spot (that lies in the $(y,\ z)$ plane)

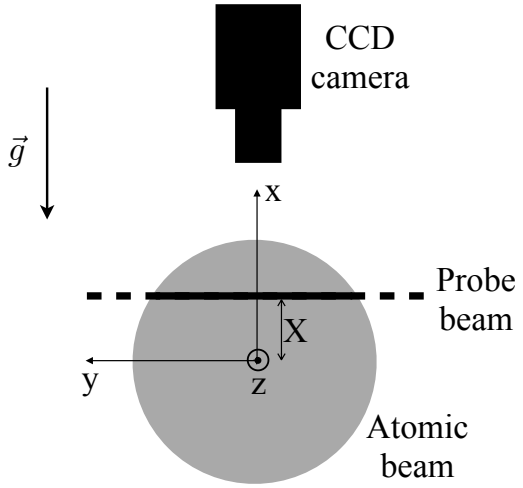

Figure 6.12: Scheme of the fluorescence detection configuration. The probe beam (dashed line) is translated perpendicularly to the x axis. For every height X, an image of the fluorescence spot (solid line) is acquired with the CCD. The atomic beam, propagating along the z axis, is represented by the gray circle.

can be expressed as:

$$S(X,\ y,\ z) = S_0 \int_{-\infty}^{\infty} \rho_{ee}(x - X, z) n(x, y) dx = \tag{6.13a}$$

$$= S_0 e^{-\frac{y^2}{w_{at,y}^2}} \int_{-\infty}^{\infty} \frac{I_0 e^{-\frac{(x-X)^2}{w_x^2}} e^{-\frac{z^2}{w_z^2}}}{I_{sat} + 2I_0 e^{-\frac{(x-X)^2}{w_x^2}} e^{-\frac{z^2}{w_z^2}}} n_0 e^{-\frac{x^2}{w_{at,x}^2}} dx \tag{6.13b}$$

with S_0 a factor including the fluorescence rate Γ and the collection efficiency of the optical system. The integration on y is due to the fact that the CCD collects the fluorescence from a volume defined by the intersection of probe and atomic beams and by the depth of field of the objective.

The parameters we are interested in, $w_{at,x}$ and $w_{at,y}$, are related to the size of the atomic beam cross-section. The function $S(X, y, z)$ has been used to make two-dimensional fits of the fluorescence images, using $w_{at,x}$ and $w_{at,y}$ as fit parameters. With the $w_{at,y}$ and $w_{at,x}$ found from the fit, we infer an horizontal FWHM=3.6 ± 0.2 mm and a vertical FWHM=4.3 ± 0.4 mm for the

atomic beam. We conclude remarking that the asymmetry between horizontal and vertical directions is probably an effect of the gravity on the atomic beam.

6.4.1 Summary of the properties of the cold atomic beam and comparison with different configurations

In the tab. 6.1 we report, as reference, a non comprehensive comparison among the performances of the atomic beams produced by several groups, as known from the literature. In the development of the laser-cooling based atomic sources, a wide variety of schemes has been explored.

Almost 20 years ago, one of the first implementations relied on a 2D MOT, a configuration in which the trapping is accomplished only in two dimensions, with the formation of a narrow atomic beam in the third one. However, in this scheme, the longitudinal atomic motion, not affected by the 2D MOT action, cannot be controlled. To make up for this configuration's shortcomings, in [111] a longitudinal optical molasses (OM) was added to the 2D MOT configuration, reducing significantly the average longitudinal velocity with respect to the bare 2D MOT scheme [112].

Another source, based on the same working principle of the PMOT (and of the conical mirror funnel CMF [62]), but completely different in terms of actual implementation, is the LVIS (Low Velocity Intense Source) [107]: a 3D MOT in which a small part of one laser beam is not retroreflected (one of the mirrors has a small hole in its center), so as to create a dark column in the radiation field, through which the atoms propagate forming a beam. We appreciate that the beams produced by LVIS and PMOT have approximately the same longitudinal velocities and flux, since both are based on inducing a "leakage" in a static 3D MOT. This implies that the performances of the produced atomic beam are somehow dictated by a compromise that must be established between the background atoms capture rate and the funnel action, which forms the beam. A broader functionality (that comes, for example, with the possibility of tuning the longitudinal velocity for almost an order of magnitude) can be reached using a "pushing" laser beam, as done in the

conventional 3D MOT setup of [113].

A systematic comparison between the performances of the three main schemes (2D MOT + OM - called, in [114], 2D$^+$MOT-, 2D MOT and LVIS) of cold atoms sources has been accomplished in [114].

We conclude highlighting the good performances of our PMOT, in comparison, for example, with the atomic yield of a very brilliant source like a Zeeman slower (ZS, [115]). In fact, even though the ZS is capable of generating a flux almost two orders of magnitude higher than a cold atomic source, this is not due to a particularly high atomic density but, rather, to a high average atomic velocity; this makes, in principle, the control of the position and velocity of few atoms very demanding.

Table 6.1: Summary of the properties of the atomic beams produced in several groups. LVIS: low velocity intense source; PB: pushing beam; CMF: conical mirror funnel; ZS: Zeeman slower; OM: optical molasses.

Ref.	Config.	Year	At.	n_{atom} (cm^{-3})	$\langle v_{long} \rangle$ (m/s)	Δv_{long} (m/s)	T_{long} (mK)	T_{trasv} (mK)	Flux (at/s)	$\Delta\theta$ (mrad)	Brightness (at/(sr·s))
[111]	2D MOT + OM	1990	Na	10^8	2.7	0.25	0.18	0.3	10^9		$3 \cdot 10^{10}$
[112]	2D MOT	1994	Cs	10^9	35	8					
[116]	ZS+OM	1994	Ne*		19						$3 \cdot 10^{10}$
[107]	LVIS	1996	Rb		14	2.7	76		$5 \cdot 10^9$	16	$5 \cdot 10^{12}$
[117]	2DMOT	1996	Rb		3-10		0.5	0.38	10^{10}		
[114]	$2D^+$ MOT 2D MOT LVIS	1998	Rb		8 11 26	3.3 12 6.3			$9 \cdot 10^9$ $5 \cdot 10^9$ $3 \cdot 10^7$	43 46 27	
[118]	PMOT	1998	K								
[64]	PMOT	1998	Cs		8-12	2-3			$1.1 \cdot 10^9$	40	$8.5 \cdot 10^{11}$
[119]	2D MOT	2000	Rb	$2.8 \cdot 10^8$	2-8		0.05	0.23	$7.4 \cdot 10^8$	56	$1.3 \cdot 10^{11}$
[113]	MOT+PB	2001	Rb		14				$7 \cdot 10^7$		
[22]	PMOT	2001	Cs	1.6×10^8	8-12	1.5	46	0.24	$4 \cdot 10^9$	26	$7 \cdot 10^{12}$
[62]	CMF	2001	Rb		4-6	0.54		0.38	$2.2 \cdot 10^{10}$	150	
[120]	PMOT	2003	Cs		7-16				$2.2 \cdot 10^9$	11-16	$1.2 \cdot 10^{13}$
[115]	ZS	2005	Rb	$7 \cdot 10^7$	45-115		90	3	$1.7 \div 3.2 \cdot 10^{12}$		
Pisa	PMOT + 2D OM	This work	Cs	$8 \cdot 10^7$	12	1.4	46	0.13	$1.2 \cdot 10^{10}$	7	$7.8 \cdot 10^{13}$

Chapter 7

Cold ion beam: experiment and properties

In this final chapter we report on the properties of the ion beam produced by photoionization of the atomic beam. In section 7.1 we describe the charge detection system used in the photoionization stage. Section 7.2 then reports the results of measurements made to determine the cold ion beam CW ion yield dependence on ionization intensity, excitation intensity and excitation frequency. As anticipated in section 3.1.6, we analyze the optical pumping effects observed at the variation of the excitation intensity on the ion yield, comparing, in section 7.3, the experimental data with the results of the simulations. Finally, in section 7.4 we report the features of the ion velocity distribution as determined by pulsed time of flight measurements.

7.1 Charge detection system and measurement protocol

To detect the ions we use a counting electron multiplier (mod. 226EM, *Thorn Emi*), already available in our laboratory, that is shown in fig. 7.1. It has 16 curved oxidised BeCu dynodes, with a typical total gain of $5 \cdot 10^7$ at the operating voltage 3 kV, and a clear aperture of 17×17 mm^2. The typical background is about 5 counts/s.

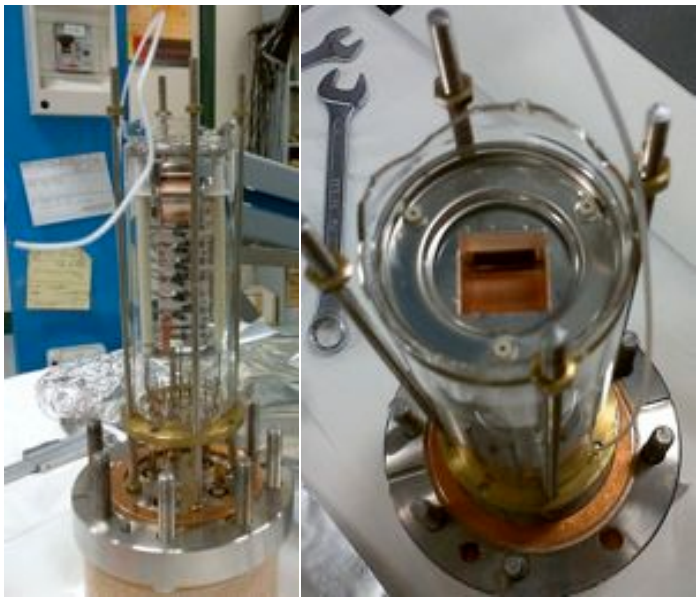

Figure 7.1: Images of the ion detector, the electron multiplier mod. 226EM *Thorn Emi*. On the left there is the detector enclosed in the glass and metal housing with which it is placed under vacuum. On the right the first dynode is imaged, curved and with a clear aperture 17×17 mm^2.

The measurements shown in section 7.2 and section 7.4 have been accomplished in two different configurations of the detector and of the rest of the charge detection system, as shown in fig. 7.2.

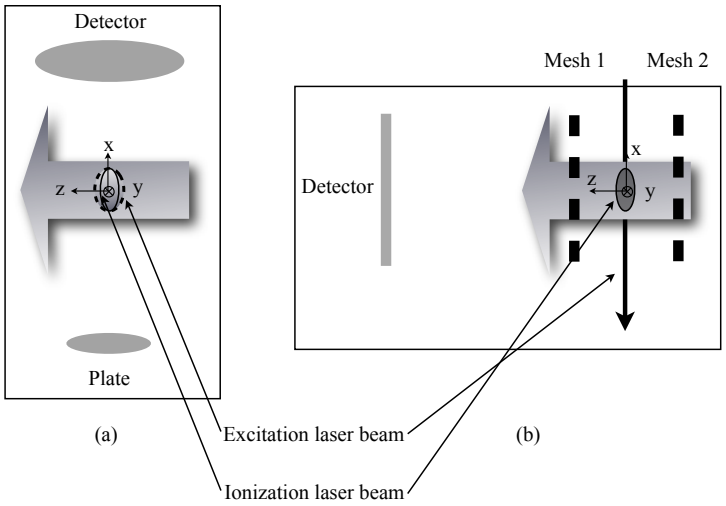

Figure 7.2: Schematic configurations of the charge detection system and laser beam arrangements in the ionization region. In the origin of the (x, y, z) reference system, maximum atomic density, maximum ionization intensity and maximum excitation intensity coincide. Configuration (a) has been used to measure the CW yield of the ion beam, while configuration (b) for the pulsed TOF measurements.

The first one (fig. 7.2 (a)) has been used to determine the CW yield of the ionization process as a function of the ionization and excitation laser power and excitation laser frequency (section 7.2). In this scheme the detector is oriented at 90° with respect to the atomic beam. The field in the ionization region is defined by the surface of the first dynode (kept at -3 kV) and a plate (10 mm diameter) placed about 3 cm under the atomic beam, typically biased at about 200 V in order to repel ions and push them onto the first dynode. In the rough approximation of uniform field, the extraction electric field is around 150 V/cm. We remark that this field causes a completely negligible (less than 50 Hz) DC Stark effect on the hyperfine lines of Cesium.

As mentioned in section 3.1.2, the laser beam spot is astigmatic; in the directions x and z (see fig. 7.2) the Gaussian intensity profiles (eq. (3.8))

have $w_{z,exc} = 1.1 \pm 0.1$ mm, $w_{x,exc} = 1.6 \pm 0.1$ mm for the excitation and $w_{z,ion} = 0.7 \pm 0.1$ mm, $w_{x,ion} = 1.6 \pm 0.1$ mm for the ionization laser beam. Since the atomic beam in the ionization stage has a FWHM of $d_y^{at} = 4$ mm (see section 6.4), we take as measure of the ionization volume V, defined by the intersection of the superposed copropagating excitation/ionization beams with the perpendicular atomic beam, the value $V = \pi w_x^{ion} w_z^{ion} d_y^{at} \simeq 15$ mm^3.

With a peak atomic beam density $n_0 \approx 10^8$ cm^{-3} (section 6.1), in conditions of strong saturation of the excitation transition ($\rho_{ee} \approx 0.5$), from eq. (4.14) we estimate an ion yield per unit time of about $3 \cdot 10^6$ ions/s. With this rate, low in comparison to the atomic flux on the order of 10^9 atoms/s, the charges are produced in a regime in which the local ion production rate is not limited by the number of neutrals per unit time that move into the ionization laser beam [45]. Due to these relatively low ion signals, experimental protocols (synchronous detection, background subtraction) to increase the S/N ratio have been exploited. On the other hand in this regime the inter-ion Coulomb effects [93] that degrade the ion source quality are safely negligible. The reason will be explained in section 7.2.

In the second configuration (fig. 7.2 (b)) the ionization laser beam has been pulsed in order to determine, in the framework of a TOF measurement, the average value and FWHM of the ion velocity distribution (section 7.4). The detector is placed on the axis of the atomic beam, while the ionization region is at about 15 cm from the first dynode surface, between two grids perpendicular to the atomic beam and kept at voltages that can be varied independently to control the electric field. The two grids are fixed at a reciprocal distance of 6 cm, they transmit about 60 % (as computed by the ratio between the diameter of the wire and the pitch), and their diameters, about 27 mm, are much larger than the transverse size of the interaction region, in order to ensure a high collection efficiency for the ions and reduced boundary effects in the ion production region.

The excitation beam can be easily moved since it is guided by a single-mode optical fiber mounted on a zy translator stage; the spot is circular, with transverse size $w^{exc} = 0.7 \pm 0.1$ mm. The ionization laser beam passes through a telescope and an AOM connected to an RF switch; the first order

diffracted beam (sent in the ionization region) has an approximately circular cross section, with $w^{ion} = 0.4 \pm 0.1$ mm. The ionization volume is defined by the intersection between excitation and ionization laser beams, and it is about 0.7 mm^3, much smaller than for the other configuration so that the ion bunch created is more spatially localized, leading to a better resolution of the TOF measurement .

The impinging ions are detected in a counting regime, easily allowed by the fast time response of the detector (2 ns rise time and 3 ns for pulse width FWHM). The pulses generated by the ion detector are sent to a dual channel gated photon counter (Stanford Research System, mod. SR400). This device is provided with two independent gates, whose length, delay with respect to an external trigger and discriminator level can be adjusted independently. The discriminator level can be used to distinguish the signal from the background counts. Furthermore, the gates can be set in a fixed position relative to the trigger, or scanned to recover time-varying signals. The input is followed by a DC to 300 MHz amplifier, allowing detection of pulses as small as 10 mV, while the two channels can count at rates up to 200 MHz. The counter has also two programmable scanning output voltages, that can be used to control other instruments. The photon counter is then connected, via GPIB interface, to a computer for automated data acquisition.

7.2 Properties of the ion beam

In this section we analyze the CW yield of the ions as a function of ionization laser intensity, excitation laser intensity and excitation laser frequency. Before showing the results of the measurements, we want to remark that what we obtain in our experimental conditions is an ionized gas, rather than a plasma.

A plasma is typically defined as an ionized gas in which the charged particles show collective effects [121]. The length scale which discriminates individual particle behavior and collective behavior is the Debye screening length λ_D, defined as the distance over which an electric field is screened by

the redistribution of electrons in the plasma. It is given by:

$$\lambda_D = \sqrt{\frac{\epsilon_0 k_B T_e}{e^2 n}} \tag{7.1}$$

where ϵ_0 is the electric permittivity of vacuum, k_B the Boltzmann constant, T_e the electronic temperature, e the elementary charge and n the electron density. The two parameters we need to estimate the Debye length, that are the kinetic electronic temperature T_e and the electronic density n, can be roughly calculated with simple topics. In section 4.2 we estimated a kinetic energy of the photoelectrons produced in our experimental conditions of about 0.6 eV. This energy corresponds to $T_e \approx 7000$ K.

On the other hand, the electronic density can be roughly estimated from the product $n_0 \rho_{ee} r_{ion} \tau_{ion} \approx 10^4$ electron/cm^3, where we used $n_0 \approx 10^8$ atoms/cm^3, $\rho_{ee} \approx 0.5$ in saturation regime, r_{ion} as given in eq. (4.13), $\tau_{ion} \approx 60\ \mu s$ (on the order of magnitude of the ionization radiation-atom interaction time) and, finally, we exploited the fact that the atoms are singly-ionized (this implies that, at least immediately after the ionization process, electronic and ionic densities are the same). With these two values, a simple calculation gives $\lambda_D \approx 4$ cm. The condition for creating a plasma is $\lambda_D < \sigma$ [122], where σ represents a typical dimension of the ionized system (in our situation it can be represented by the transverse size of the ionization volume, on the order of 3-4 mm). Therefore the condition for the formation of a plasma is clearly not satisfied in our situation, and the result of the atomic beam ionization is an ionized gas , not a plasma.

7.2.1 Ion yield as function of the ionization laser intensity

The aim of these measurements is to ascertain the linear dependence of the ion yield on the ionization laser intensity, as dictated by eq. (4.14). The results in fig. 7.3 show the expected linear increase of the ion counts with the ionization power. The fact that this linearity is respected, at least in the range of ionization powers explored, represents a direct confirmation of what

we claimed in chapter 4, that the ion yield is, in practice, totally due to the one-photon ionization of the excited atoms.

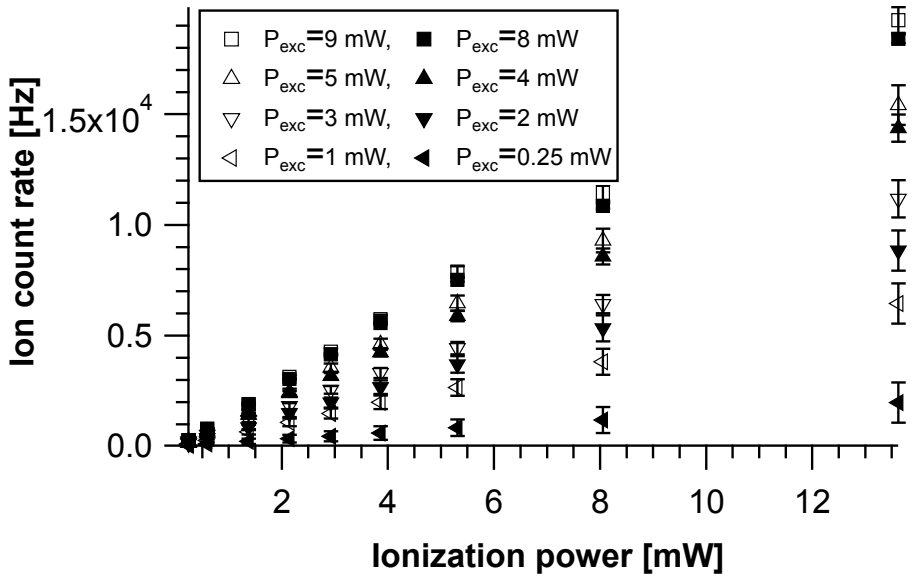

Figure 7.3: Ion signal as function of the ionization laser power, for several excitation laser powers. The gate of the photon counter is open for 0.5 s. The error bars represent the statistic fluctuations of ion counts in repeated measurements.

These measurements have been accomplished for several excitation powers. As expected, a change in the excitation power modifies only the slope of the experimental trends, as again prescribed by eq. (4.14). Furthermore, the increase in the excitation power is connected to a progressively smaller increase in the slope: this behavior is a clue of the saturation of the first transition in the two-step photoionization, and it will be analyzed more in detail in section 7.2.2.

Unluckily, without an absolute calibration of the detector and a precise knowledge of the ion collection efficiency, the experimental ion counts do not allow determining the absolute charge amount generated in the photoionization.

Finally, the signal-to-noise ratio of these measurements have been increased

with a background subtraction and implementing a synchronous detection: the timing is sketched in fig. 7.4. One of the analog voltage outputs of the

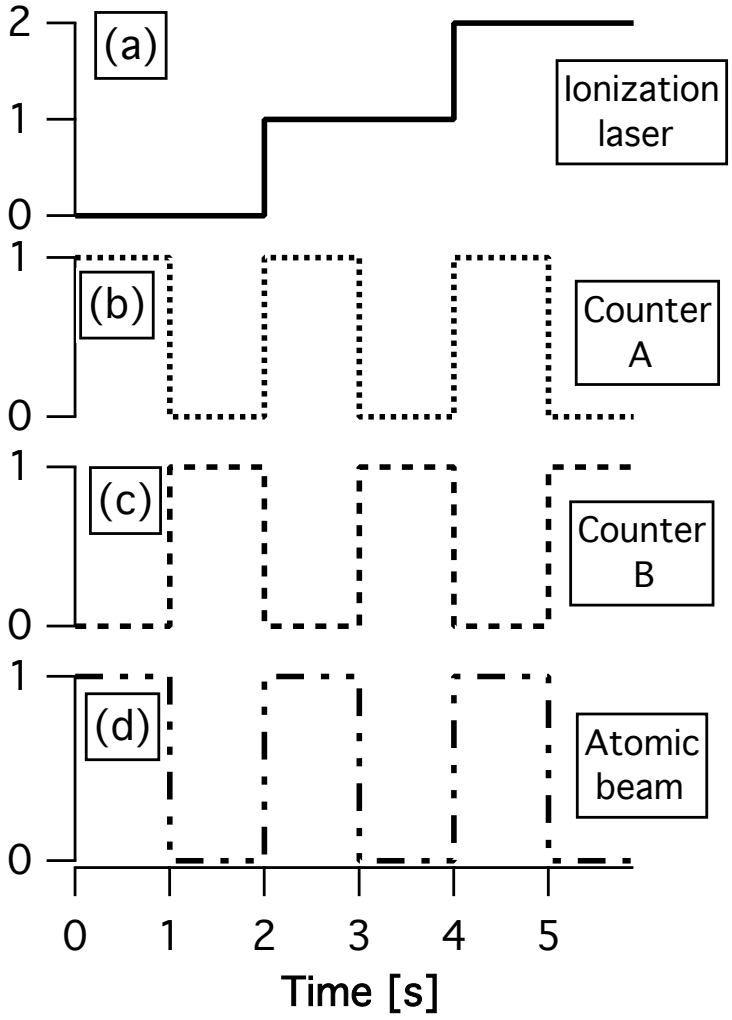

Figure 7.4: Schematic representation of the timing used to measure the ion yield as a function of the ionization intensity. Trace (a) represents the ladder voltage sent to the ionizing laser in order to increase its output power. For every step in the radiation power, the atomic beam (trace (d)) is switched on and off. The counter A (trace (b), counting is enabled when high) detects the signal due to the ionization of the atomic beam and the background; the counter B (trace (c)) counts only the background. The difference between these counts is considered in the analysis of the experimental results.

photon counter has been programmed to generate a ladder voltage (trace (a) in fig. 7.4) that, sent to a TTL input in the laser current control, allows to increase the power of the laser radiation (in exponentially increasing steps, due to the IV characteristic of the diode). We remark that the effects of the detuning of the ionization laser beam frequency due to the power increase is safely negligible. At the same time, another output of the counter generates a time varying voltage (trace (d) in fig. 7.4) that, sent to a switch connected to the compensation coils, allows the switching of the atomic beam. Finally, both the gates of the counter are exploited: gate A (trace (b) in fig. 7.4) detects the signal of the atomic beam and the background, while gate B (trace (c) in fig. 7.4) counts only the background pulses produced in the absence of the atomic beam. We underline that the counters are opened 5 ms after the current in the compensation coils has been switched, in order to avoid any transient in the atomic beam density.

The difference between the gate A and gate B counts is the signal, purified from every contribution not due to the photoionization of the atomic beam (see the end of section 7.1), including the instrumental pedestal (noise) of the detector. Another advantage of this scheme is the fast measurement (in total about 20 s per scan), that reduces the effects of drifts and instabilities of the experimental apparatus.

7.2.2 Ion yield as a function of the excitation laser intensity

Contrary to the ionization intensity case, the dependence of the ion signal on the excitation laser intensity is strongly non linear, since it reflects the saturation of the atomic transition. In fig. 7.5 the ion signal is shown as a function of the excitation laser intensity, with the excitation frequency locked on the T43, T44 and T45 hyperfine transitions and without repumping radiation. The error bars are determined by the fluctuations of the ion counts during the acquisitions.

These ion signals are proportional to the transition line intensities defined, for the two-level system, in eq. (3.1). Beyond the saturating trend, evident in

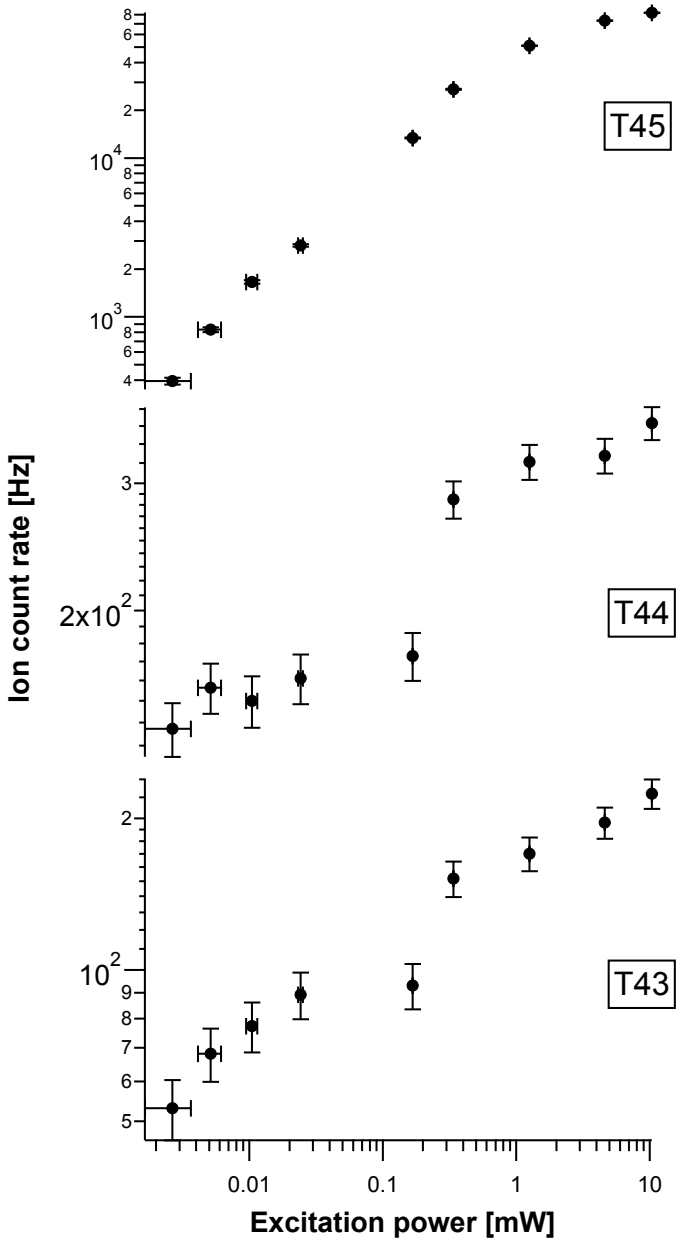

Figure 7.5: Ion signal as function of the excitation laser intensity. The exciting frequency is locked (from top to bottom) on the T45, T44 and T43 atomic resonances. The gate length is 0.5 s. The error bars represent the statistic fluctuations of ion counts in repeated measurements.

all the three transitions, it is remarkable also the huge difference, almost two orders of magnitude, between the high-excitation-power counts of the T45 and of the other two transitions. This implies that the relative line intensities are not correctly reproduced by the two-level theory, as we anticipated in section 3.1.5. In section 7.3 we will show how these results can be interpreted based on the occurrence of HP and ZP effects.

7.2.3 Ion yield as a function of the excitation laser frequency

Sweeping the frequency of the excitation laser leads to produce a typical ion yield spectrum as the one shown in fig. 7.6. In the spectrum the three peaks

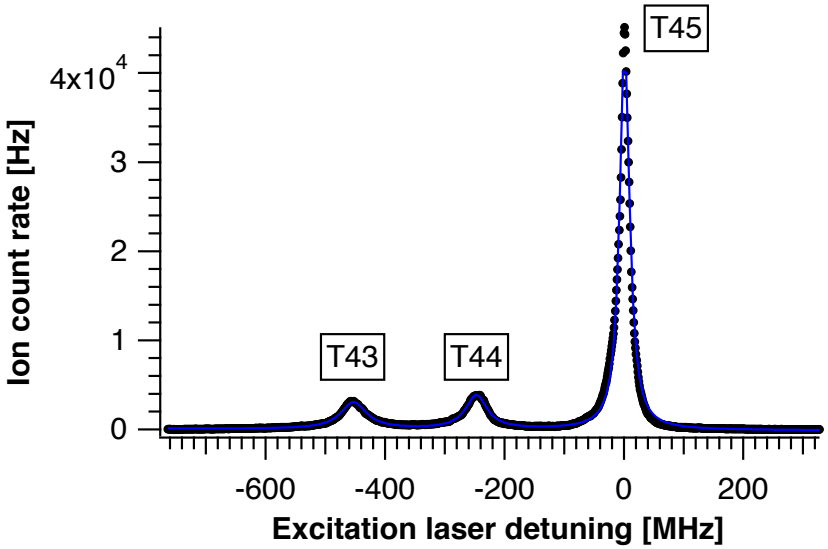

Figure 7.6: Ion signal (points) acquired sweeping the frequency of the excitation laser ($P_{exc} = 3$ mW). From the left to the right the peaks of the T43, T44 and T45 are detected. The line represents the best fit obtained from a superposition of Lorentzian functions centered on the atomic resonance frequencies.

corresponding (from left to right) to the T43, T44 and T45 are clearly visible.

The fit in fig. 7.6 is a superposition of Lorentzian functions, centered on the atomic resonance frequencies. We chose the Lorentzian function to model the lineshapes because, in principle, the photoionization causes an homogeneous

broadening, since it affects in the same way all the excited atoms. However, in practice the photoionization rate is so low that the broadening due to this loss mechanism is fully negligible.

The horizontal frequency axis, whose origin corresponds to the T45 frequency, has been calibrated acquiring simultaneously the saturated absorption signal of the laser in the Cs reference cell and comparing the corresponding peaks. We estimate the uncertainty associated to the mentioned calibration procedure in about 3 MHz; this value is mainly due to two contributions: (i) non linearity and hysteresis in the elongation of the piezoelectric translator that moves the grating closing the laser cavity; since the frequency of the excitation laser is changed just suppliyng a voltage ramp to this piezoelectric, a non-linearity makes difficult to find a relation between the voltage and the frequency change; (ii) a too high uncertainty in the fitting procedure of the peaks in the saturated absorption signal.

The lack of other independent frequency measurement tools prevented improving the accuracy. The acquisition of these spectra was rather cumbersome: every point of the spectrum corresponds to a counter gate aperture of 0.5 s. During this interval the voltage to the piezoelectric is kept constant, but we do not have any possibility to keep the *frequency* stable, within the quoted uncertainty. In summary, *a posteriori* we selected spectra without too strong instabilities, as the one shown in fig. 7.6.

The low accuracy of the frequency calibration makes the spectra we acquired not very useful, at least to determine the spectral broadening of the transitions. However, these data can be useful for a "visual" evidence of the variation of the relative line intensities with the excitation power. In fact, in the spectra shown in fig. 7.7 we can easily appreciate the variation in the peak ratios (the T45 peak is normalized to 1) with the power of the excitation laser beam.

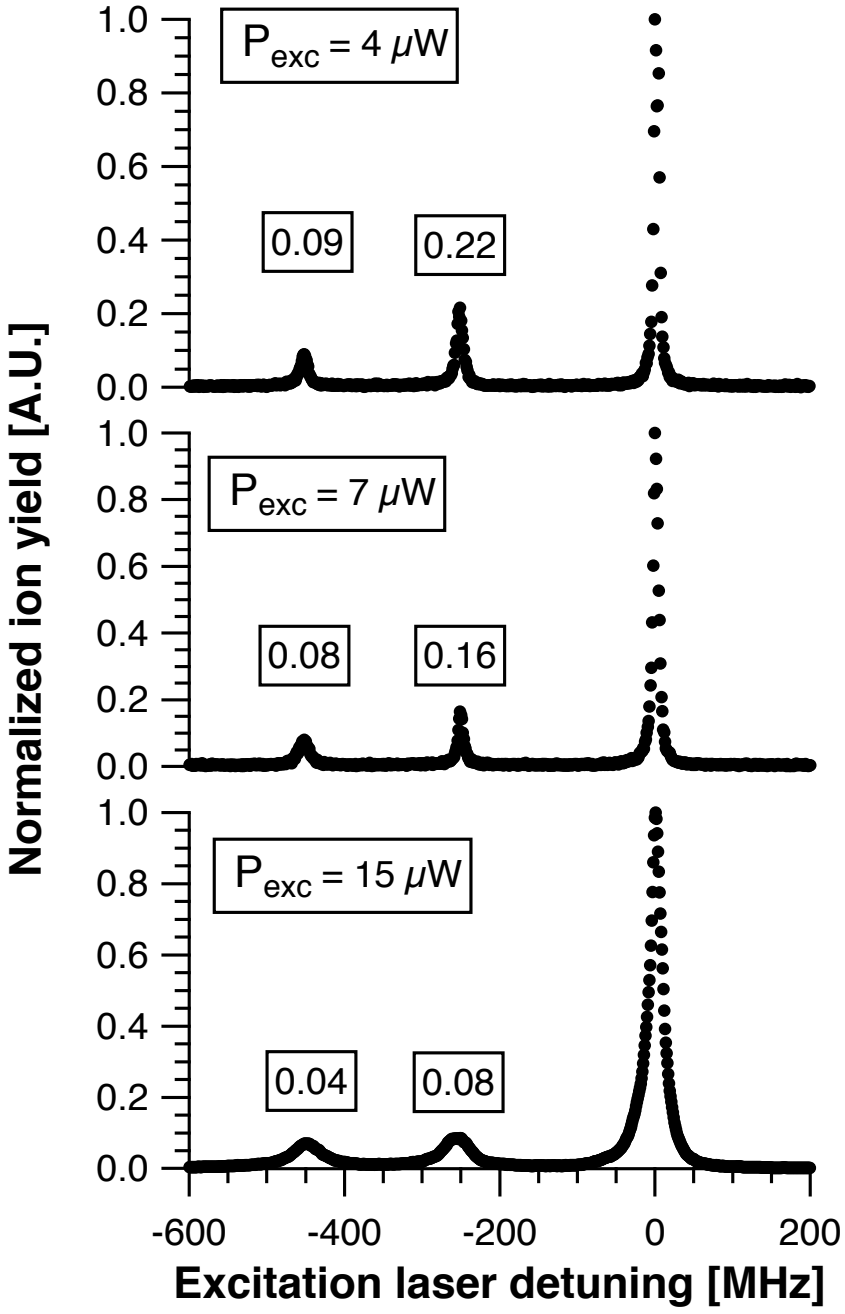

Figure 7.7: Normalized ionization spectra acquired with different excitation laser power, as shown in the legend, in which the peak intensity of the T45 is set to 1. The values of the relative intensities of the T44 and T43 peaks are shown in the frames: it is clear their decrease with the excitation intensity.

7.3 Optical pumping effects on the hyperfine transition strength ratios

This section concludes the part of the chapter dealing with the measurements accomplished in CW regime. The importance of the optical pumping effects in the interpretation of some aspects of the experimental data shown previously is highlighted here, together with the outcomes of the numerical simulations whose implementation has been introduced in section 3.1.7.

7.3.1 Experimental data

In fig. 7.8 the dependence of $\mathcal{R}_{45,44}$ and $\mathcal{R}_{44,43}$ (eq. (3.38)) on the excitation laser intensity is shown. The points represent the experimental data, obtained as ratios of the ion counts reported in fig. 7.5. The lines represent the results of the simulations; in particular, the eq. (3.32) have been numerically solved corresponding to the power used experimentally and for each one of the T43, T44 and T45 transitions. Then, the quantities in eq. (3.33) have been computed, from which the numerical relative line intensities $\mathcal{R}_{45,44}$ and $\mathcal{R}_{44,43}$ have been obtained via the eq. (3.38). The lines in fig. 7.8 represent these numerically obtained relative line intensities.

As commented in section 3.1.5, we notice that both the experimental (fig. 7.8) and the two-level theoretical (fig. 3.5) relative line intensities match, at low excitation intensities, the theoretical transition strength ratios ($\mathcal{R}_{45,44} = 2.09$ and $\mathcal{R}_{44,43} = 3$). When the excitation intensity is increased, the discrepancy between the trends in fig. 3.5 and fig. 7.8 strongly suggests that the two-level model becomes completely unuseful. In particular, while $\mathcal{R}_{44,43}$ retains somehow the behavior predicted by the two-level model, decreasing with the excitation intensity, the $\mathcal{R}_{45,44}$, instead, departures completely from the predictions of the model.

In order to ascertain separately the roles of HP and ZP in the relative line intensities trends, we carried out the numerical simulations in two regimes. In one of them we accomplished the computation without summing the spontaneously emitted photon polarizations in eq. (3.32a) and eq. (3.32b),

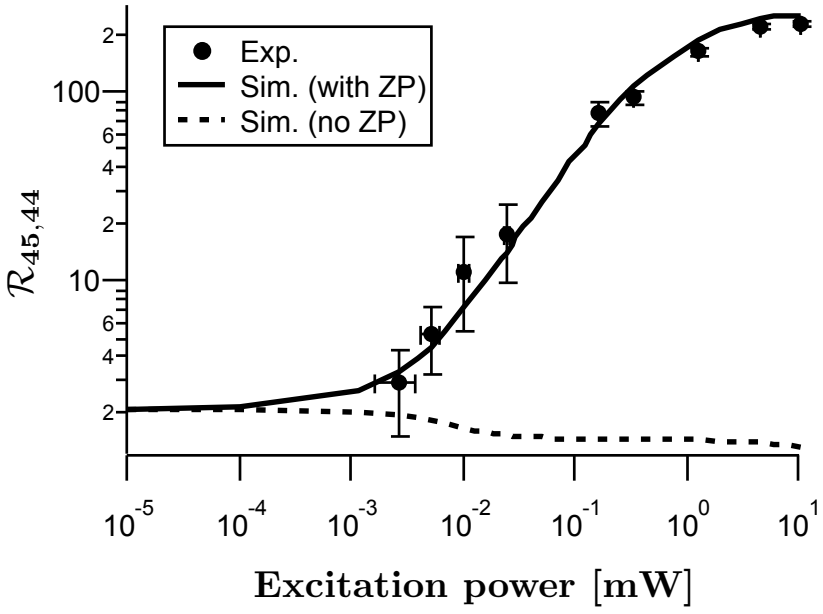

(a)

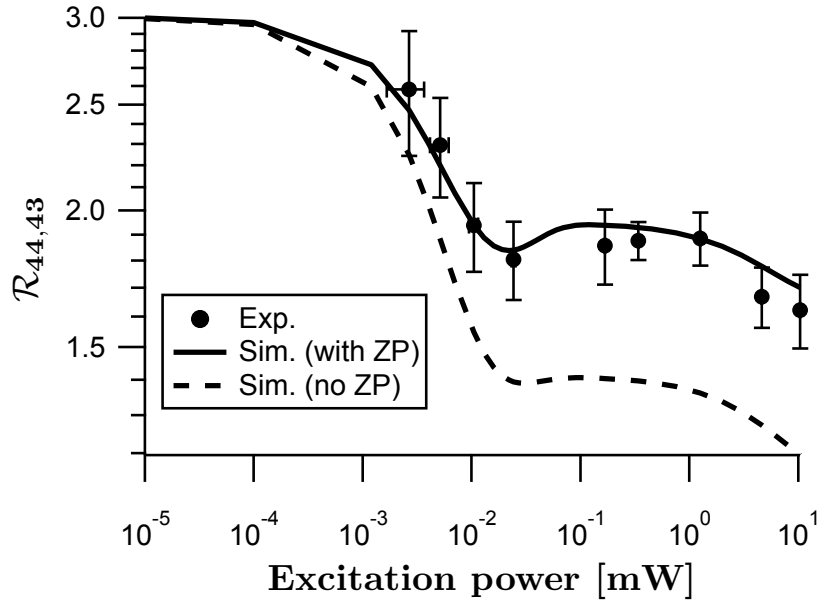

(b)

Figure 7.8: Relative line intensities $\mathcal{R}_{45,44}$ and $\mathcal{R}_{44,43}$ (points) as a function of the excitation power. The points represent the experimental data; the dashed lines are the results of the simulation based on eq. (3.32), in which the ZP effects have been disregarded; the continuous lines represent the results of the numerical simulation in which both HP and ZP are taken into account.

that is neglecting the ZP. The results are the dashed lines in fig. 7.8. In the other regime, all the terms in eq. (3.32) have been considered, and the results are the continuous lines.

We note that neglecting the ZP does not allow to reproduce correctly the experimental data, and the disagreement is particularly large for the $\mathcal{R}_{45,44}$.

7.3.2 Interpretation of the experimental data

In this section we explain the trends of the relative line intensities investigated experimentally, treating separately the $\mathcal{R}_{45,44}$ and the $\mathcal{R}_{44,43}$.

Before going into the details, we introduce the *branching ratios*, quantities that will be useful in the following discussion. The importance of the HP can be quantified [65, 83] by means of the branching ratios Π_{eg} that give the probability for an atom excited from a state F_g to a state F_e, to return to the level F_g as a consequence of a spontaneous emission event. According to the procedure drafted in [65], it is possible to compute the values of the branching ratios reported in tab. 7.1.

Π_{33}	Π_{34}	Π_{43}	Π_{44}	Π_{54}
3/4	1/4	5/12	7/12	1

Table 7.1: Branching ratios Π_{eg} computed for the hyperfine transitions of the Cesium D_2 line we are interested in.

Comparing table 3.1 and table 7.1 we see that Π_{eg} and S_{F_g,F_e} are proportional: this is a trivial consequence of the fact that the higher the excitation probability (proportional to S_{F_g,F_e}) from a level F_g to F_e, the higher the probability (proportional to Π_{eg}) for an atom in F_e to decay back to F_g .

We notice that $\Pi_{54} = 1$ confirms that the T45 is a closed transition, as discussed in section 3.1.6.

On the contrary, we see that $\Pi_{44} = 7/12 \approx 0.6$ implies that an atom excited to the $F_e = 4$ level has only 60% of probability to come back to the starting level $F_g = 4$. The situation is similar for the T43, with a probability $\Pi_{34} = 1/4 = 0.25$ for an atom in the $F_e = 3$ level to come back to $F_g = 4$.

On the basis of these values, at the first sight one could think that HP affects the intensity of the T43 more than the T44, since $\Pi_{34} < \Pi_{44}$ implies that the atoms are "pumped away" from the T43 faster than from the T44. Surprisingly, as demonstrated in [65], the actual situation is exactly the opposite: a transition is much more influenced by the optical pumping as much as its branching ratio is near to 0.5. Then, we conclude that T43 is actually less affected by HP than T44.

Ratio $\mathcal{R}_{45,44}$

The experimental relative line intensity $\mathcal{R}_{45,44}$ increases monotonically with the excitation power: this means that the T45 increases its intensity with the excitation power much faster than the T44. As we know, this is a consequence of the HP. In particular, the huge values of the $\mathcal{R}_{45,44}$ at high excitation intensity are due to the fact that the HP effects increase with the excitation intensity: the more atoms are excited in the $F_e = 4$, the more are lost to the $F_g = 3$. Hence, apparently the experimental trends are easily explained just on the basis of only the HP. Actually, the dashed line in fig. 7.8 (a), obtained neglecting the ZP, is in strong disagreement with the experimental data in the moderate/high excitation intensity regime. This is because, in the high intensity regime, the ZP is no longer a negligible mechanism because several absorption-spontaneous emission cycles accumulate an appreciable fraction of the population in the level $|F_g = 4,\ m_g = 0\rangle$. Consequently, the increasing (with the excitation power) probability for an atom to be trapped in the non interacting Zeeman state reduces the line intensity of the T44, leading to the large increase in the relative line intensity of the T45 with respect to the T44.

Ratio $\mathcal{R}_{44,43}$

The case of the $\mathcal{R}_{44,43}$ is very different from the previous one, since here both the transitions we are considering are affected by HP and ZP. Consequently, the interpretation of the relative line intensity trend, not monotone as for the $\mathcal{R}_{45,44}$, in this case is more difficult. We begin a tentative explanation remarking that ZP effects are expected to be more marked in the T43 than in

the T44, simply because the former has two trap states ($|F_g = 4,\ m_g = \pm 4\rangle$), while the latter has only one trap state ($|F_g = 4,\ m_g = 0\rangle$), as shown in fig. 3.6. This is confirmed by the fact that the $\mathcal{R}_{44,43}$ computed neglecting the ZP, represented by the dashed line in fig. 7.8 (b), is always lower than the experimental data: this means that neglecting the ZP overestimates the intensity of the T43. Therefore this should imply, increasing the excitation power, a growth in the T43 intensity lower than in the T44, leading then to an increasing $\mathcal{R}_{44,43}$. On the contrary, HP affects more the T44 than the T43, for what mentioned in the beginning of this section. This implies a decrease in the $\mathcal{R}_{44,43}$ with the excitation power. In synthesis, the resulting trend of $\mathcal{R}_{44,43}$ can be considered as resulting from the balancing effects of HP and ZP.

We conclude remarking that the numerical model reproduced with a very good agreement the experimental data, allowing us to discern the roles played by the different optical pumping mechanisms in the experimental trends. Furthermore, the extremely low invasiveness of the photoionization process allowed the investigation of optical pumping processes critically dependent on the atom-radiation interaction time and free from self-pumping processes [73] due to the probe itself, as it happens in the conventional saturated absorption configuration conventionally used to explore these phenomena.

7.4 Ion time of flight

The features of the ion beam velocity distribution have been determined by means of TOF measurements, whose results are reported in section 7.4.1. In section 7.4.2 we explain how we modeled numerically the electrostatic configuration in which the TOF measurements have been accomplished and how we implemented a simple Monte Carlo simulation reproducing the ion bunch dynamics. Finally, in section 7.4.3 we compare experimental and numerical results.

7.4.1 Experimental results

The TOF signals have been acquired pulsing the ionizing beam by means of an AOM (*Crystal Technology*, mod. 3200-120); both the acceleration field generated by the two meshes (configuration depicted in fig. 7.2 (b)) and the excitation laser beam are on during the ionizing laser pulse.

The measurements have been carried out according to the timing sketched in fig. 7.9. Both the counter and the control circuit of the AOM are triggered by the same pulse generator. The counter is used in a "boxcar" mode: for a certain delay of the gate (open for 0.5 μs) with respect to the trigger, the counts are accumulated on 10^6 trigger pulses (i.e. laser shots); completed the accumulation, the delay of the gate is incremented by 0.5 μs, and another accumulation starts.

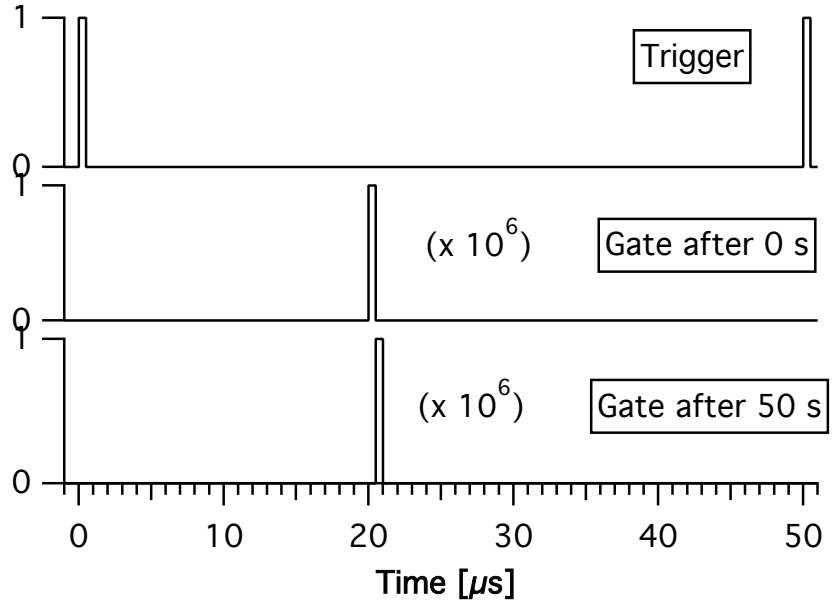

Figure 7.9: Timing of the TOF measurement. The top trace shows the trigger pulse, with a repetition period of 50 μs. The position of the gate with respect to the trigger (delay of 20 μs) at the beginning of the measurement is shown in the middle trace. Completed 10^6 accumulations, hence after $10^6 \times 50\ \mu\text{s} = 50$ s, the gate is moved to the position shown in lowest trace. The process ends when a complete sweep is accomplished (typical maximum gate delay 27 μs).

In this way, TOF signals like the one shown in fig. 7.10 are acquired. On the same split horizontal axis (the two halves have the same scale) are plotted both the time profiles of the ionizing beam laser (on the left, represented by the dots) and the ion signal (on the right, represented by bars).

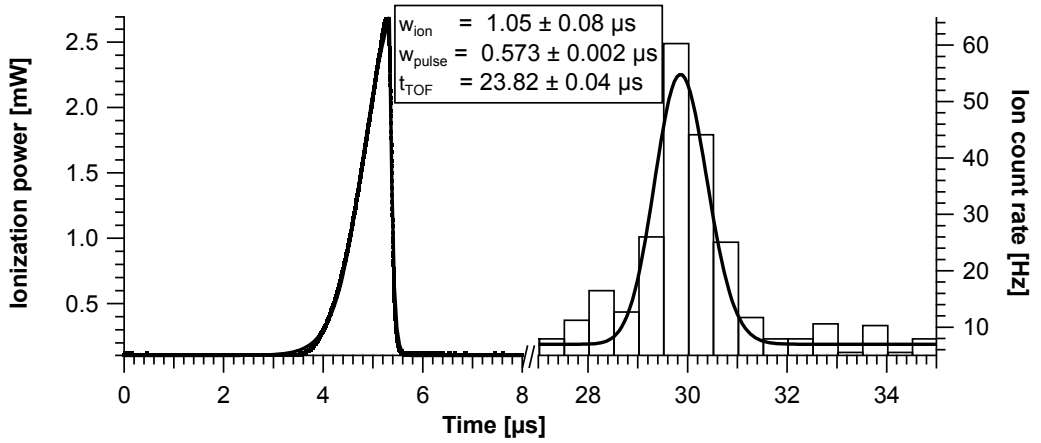

Figure 7.10: Ion signal (bars) detected after the ionizing pulse. The temporal profile of the laser pulse (dots) is measured by means of a fast photodiode (resolution in the order of 50 ns).

The time profile of the ionizing beam power has been measured sending a small fraction of the ionization beam on a calibrated fast photodiode, whose time resolution is about 50 ns. We remark that the strong departure of the ionizing pulse shape from the expected square wave profile results from a combination of factors (limited bandwidth of the electronic control circuit of the AOM, large size of the laser beam and of the AOM clear aperture) limiting the available bandwidth.

The bars representing the ion signal show the ion counts acquired with a gate length of 0.5 μs and accumulated on 10^6 laser shots.

In order to numerically reproduce in the more possible accurate way the experimental results, we took a certain care in choosing the appropriate function to fit the ionization pulse. In fact, in section 7.4.2 we will show how the fitting function has been used as probability distribution from which the random "creation" times of the ions are extracted. We found that the laser

temporal profile shown in fig. 7.10 is well represented by the function:

$$f(t) = V_0 \left(1 + \tanh\left(\frac{t - t_{c1}}{\tau_1}\right)\right) \cdot (1 - \mathrm{H}(t - t_{c2})) + \\ + V_0 \left(1 + \tanh\left(\frac{t_{c2} - t_{c1}}{\tau_1}\right)\right) \cdot \mathrm{H}(t - t_{c2}) \exp\left(-\frac{t - t_{c2}}{\tau_2}\right), \qquad (7.2)$$

where the functions $H(t - t_0)$ are Heaviside functions, whose value is 0 for $t < t_0$ and 1 elsewhere. The pulse width (FWHM) of the function in eq. 7.2 is $w_{pulse} = t_{c2} + \tau_2 \ln 2 - t_{c1}$, while the maximum value is obtained for $t = t_{c2}$ and it is given by $P_{max} = V_0 \left(1 + \tanh\left((t_{c2} - t_{c1})/\tau_1\right)\right)$.

On the left of fig. 7.10 the result of the fit using the model function of eq. 7.2 (continuous line) is superposed on the measured laser temporal profile: the resulting pulse width (FWHM) is $w_{pulse} = 0.573 \pm 0.002$ μs. Instead, the ion signal has been fitted with the function reported in eq. (6.6), obtaining a pulse width (FWHM) $w_{ion} = 1.05 \pm 0.08$ μs. For the fit we use a neutral atom TOF function because we neglect the ion-ion interactions (see the end of section 7.4.2 for a discussion of this approximation) and, even if the ions are accelerated in the detector field, from the fit we extract the value of the average longitudinal ion energy.

An ion signal wider than the ionizing pulse suggests that the time resolution of the measurement is not limited by the width of the ionizing pulse itself. Therefore, we can conclude that the measured temporal width of the ion signal is an intrinsic property of the ion velocity distribution.

7.4.2 Numerical modeling of the electrostatic configuration: ion dynamics

In section 7.2 and section 7.3 we investigated the trends in the ion yield changing several parameters not related to the electric field configuration that, on the contrary, has been kept fixed. Consequently, in order to reproduce numerically the experimental data we did not need to model the electrostatic setup.

On the contrary, the analysis of the dynamical properties of the ions, being

mainly determined by the interaction of the ions with the surrounding electric field, requires the numerical computation of the extraction electric field. To this task we exploited the numerical tool *Poisson Superfish*, freely available online. We modeled the configuration as much precisely as possible, taking into account the shape of the vacuum chamber (kept at ground potential), of the detector first dynode (kept at -3 kV) and of the other elements of the charge collection system. One limitation of the program is that it allows to model only two-dimensional or three dimensional cylindrically-simmetric systems. The routines allow the computation of the cartesian components of the electric field and the electrostatic potential in the region of interest. The results have been interpolated, generally on 20000 points uniformly covering a region - about 20×3 cm^2 - corresponding to the longitudinal cross section of the volume in which the motion of the ions takes place. The interpolated components[1] of the electric field, E_x and E_z (for the reference system, see fig. 7.11) are then used in the ion equations of motion:

$$\frac{dx}{dt} = \frac{qE_x(x,z)}{M}$$
$$\frac{dz}{dt} = \frac{qE_z(x,z)}{M}$$

where $q = 1.6 \cdot 10^{-19}$ C is the modulus of the electron charge and M the atomic mass of Cs. From the numerical solution of these equations the ion trajectories are obtained.

One example of results obtained from Poisson-Superfish is reported in fig. 7.11, where the electric field lines in the ionization region are shown for the configuration in which the TOF measurements have been carried out (see fig. 7.2 (b)).

The ion trajectories are computed starting from initial conditions that mimic the experimental ones. The (x, z) initial positions of the ions are randomly extracted from a two-dimensional Gaussian distribution, whose standard deviations σ_x and σ_z match the transverse sizes w_z^{ion} and w_x^{exc} of

[1]For analogy with other parts of the thesis, in this section the components of the vector quantities are expressed in a cylindrical coordinate system in which x and z indicate the components orthogonal and parallel to the symmetry axis, respectively.

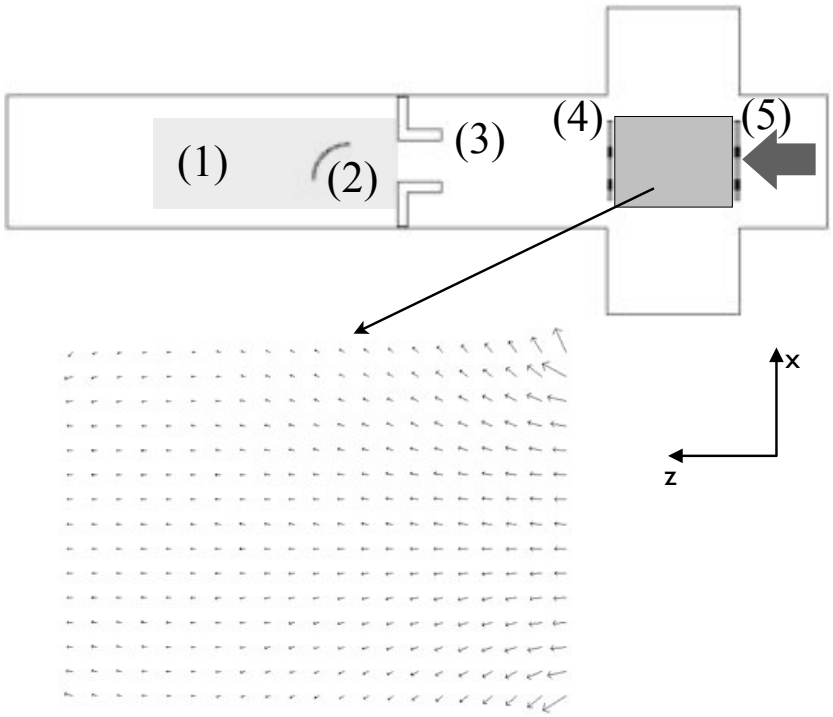

Figure 7.11: Schematic representation of the configuration used for the TOF measurements. The electric field lines in the ionization region (grey rectangle) are reported as computed with Poisson-Superfish. The atomic beam direction is indicated by the thick grey arrow. Legend: (1) detector glass envelope; (2) first dynode; (3) holder of the detector, kept at ground potential; (4), (5) meshes.

the ionization and excitation orthogonal laser beams defining the ionization volume. The initial ion velocities are assumed to be the same of the atoms. However, these parameters are not critical, since the fast acceleration undergone by the ions after their creation hides the original atomic dynamics. The ion creation times have been randomly extracted from a probability density function (PDF) given by eq. (7.2)[2]. We exploited the cumulative distribution function (CDF) method [123], that allows the generation of random variates according to an arbitrary PDF $f(t)$, based on the fact that its invertible CDF $F(t)$ is comprised between 0 and 1 for every t.

Following this method, a random number $\bar{t}$ distributed according to $f(t)$ can be obtained extracting a random number u from a uniform distribution on the interval $(0, 1)$ and then solving the equation $F(\bar{t}) = u$. Following this procedure and computing, from eq. 7.2, the CDF $F(t) = \int_{-\infty}^{t} f(t')dt'$:

$$F(t) = \tau_1 \mathcal{N} \log\left(1 + \exp\left(\frac{2(t - t_{c1})}{\tau_1}\right)\right)(1 - \mathrm{H}(t)) + \\ + \tau_2 \mathcal{N}\left(1 + \tanh\left(-\frac{t_{c1}}{\tau_1}\right)\right)\left(1 - \exp\left(-\frac{t}{\tau_2}\right)\right)\mathrm{H(t)}, \tag{7.3}$$

with

$$\mathcal{N} = \frac{1}{\tau_2 + \tau_1 \log\left(1 + \exp\left(-\frac{2t_{c1}}{\tau_1}\right)\right)} \tag{7.4}$$

(where, without losing generality, we put $t_{c2} = 0$) we obtained, for every ion, the initial time from which to start computing the evolution.

Typically we computed the trajectories of 10000 ions, following their motion from the ionization volume to the first dynode surface. The integration time and the interpolation grid steps for the electric field have been adjusted verifying the convergence of the outcomes. An example of the results is shown in fig. 7.12: every red dot represents the position of one ion at a certain time; the background is a gray-scale image of the electric field absolute value, as obtained from Poisson-Superfish. The typical value for the electric field in the

[2]We assume that the initial temporal ion distribution follows the laser beam time profile because of the linearity between ionization rate and laser intensity and the extremely short time required for an ionization event to take place.

ionization region is about 40 V/cm. The ion positions are sampled at regular intervals of 1 μs; in this way, looking at the image from right to left, we can see the evolution of the ion bunch from the formation to the impinging onto the detector.

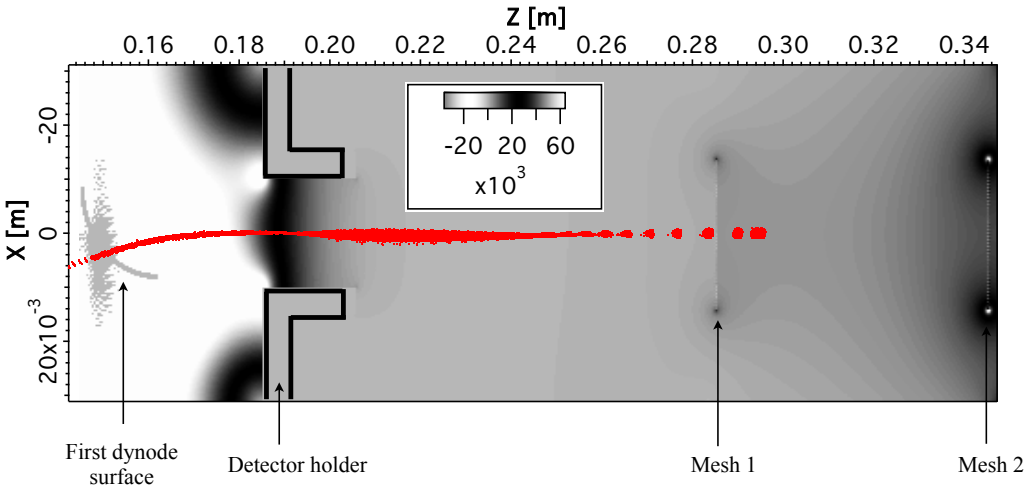

Figure 7.12: Simulated ion trajectories in the experimental configuration. The position of the relevant elements is shown for reference.

In modeling the dynamics of the ion bunches we did not take into account the inter-ion Coulomb interactions and the space charge effects that, according to simulations and results from different experimental set-ups [93], are of great relevance in determining the dynamical features of the ion beam. We justify this approximation as follows. In [93] the authors implement a simulation taking into account the inter-ion interactions because, according to the experimental ion current, the estimated average number of ions per bunch is about 35. With our experimental parameters, the average number of ions per bunch is extremely low, actually less than one. If we assume, in a first approximation, an efficiency $\eta = 1$ of the charge detection system (the ions detected are *all* the ions produced), from the integration of the ion signal shown in fig. 7.10 we have that the accumulation on 10^6 laser shots results in about 150 ions. This means that, on the average, on the detector 1 ion impinges every $6 \cdot 10^3$ shots: since the shots repetition period is 50

μs, we conclude that, on the average, an ion impinges on the detector every $6 \cdot 10^3 \times 50$ μs=0.3 s. Since the time of flight of the ions is much smaller than 0.3 s, we infer that when an ion was created, the preceding one already reached the detector. In this condition, it is clear that the inter-ion Coulomb interactions cannot play any role.

The assumption $\eta = 1$ suggests that 0.3 s should be regarded as a higher bound for the average time between the arrivals of two successive ions. In fact, a more realistic $\eta < 1$ implies that the actual ion production rate could be higher than the observed, and consequently that the arrival time between the ions could be shorter than 0.3 s. A lower bound for the average time between two ion arrivals can be estimated from the assumption that *all* the ions produced are detected. In this case, the average number of excited atoms interacting with the ionization beam is about $3 \cdot 10^4$; the peak ionization rate can be obtained from eq. 4.13 with $I_{ion} \approx 150$ mW/cm^2: $r_{ion}^{peak} \approx 5$ s^{-1}. Since the ionization pulse duration is around 1 μs, we can estimate a maximum of about 0.2 ions per laser shot produced, equivalent to 1 ion every about 5 shots, that is 1 ion every about 5×50 μs=250 μs. However, also in this case, the time interval between the arrival of two ions is too low to produce appreciable space charge effects.

7.4.3 Comparison with the simulated results

The TOF signals have been numerically reproduced according to the procedure explained in sec. 7.4.2. Figure 7.13 represents the simulated version of fig. 7.10. The left peak represents the histogram (bin width of 0.1 μs) of the ion creation times, randomly extracted according to the method explained in section 7.4.2. The peak on the right, centered around 24 μs, is obtained binning the ionic arrival times on the first dynode surface of the detector. Similarly to the experimental ion signal in fig. 7.10, the simulated signal has been fitted with the function in eq. (6.6), in order to get comparable values of the time of flight and the ion peak width. We can appreciate the good agreement between the experimental, 23.82 ± 0.04 μs, and the simulated, 23.93 ± 0.02 μs, time of flights, suggesting that the numerical model has been able to capture the

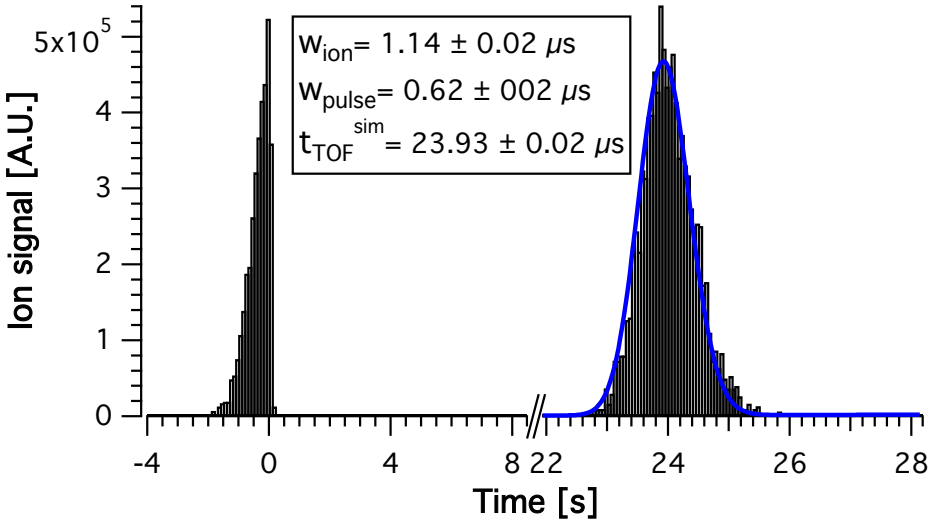

Figure 7.13: Results of the simulation: initial (left) and final (right) ion temporal distribution. The initial distribution has been obtained according to the method explained in the text. The simulated ion final distribution is obtained binning the arrival times on the detector.

main characteristics of the experimental configuration.

The experimental ion TOF value gives, on a flight distance of 15.3 ± 0.5 cm, an average kinetic energy of the ions of 26.5 ± 1.8 eV.

We remark that the temporal width of the ion signal is equivalent to an energy spread $\Delta E \approx 2.4$ eV. This value cannot be ascribed to the initial atomic energy spread, estimated on the order of 25 μeV. Actually, the width of the ion signal is due to the spatial extension of the ionizing laser beam. In fact, from a numerical computation made with *Poisson Superfish* and the potentials of the meshes used during the measurement, it is found that the ionization takes place in an electric field $E_0 \approx 3350$ V/m. Accordingly, the initial ion energy broadening can be roughly estimated by $\sigma_r e E_0 \approx 2.3$ eV, where $\sigma_R = 660$ μm is the FWHM of the ionization laser beam.

In conclusion, we demonstrated the feasibility of an ion beam obtained by photoionization of a cold and slow atomic beam. This configuration puts as apart from the mainstream research in the field of the UCIS (ultracold ion source [49]), where generally photoions are extracted from cold atomic

clouds in magneto-optical traps. The relatively low atomic density available, leading to a low number of ions produced, can be mitigated implementing a transverse compression stage on the atomic beam (for example a 2D MOT) in order to increase the atomic density. This, of course, would be at cost of the experimental simplicity.

On the other hand, our experimental configuration (similar, we recall, to the first inception of these schemes [124]) can be advantageous for its independence on the need of an acceleration/extraction longitudinal electric field, since the ions, at the moment of their creation, have already an average velocity different from zero, that is the contrary of what happens when a static atomic sample like the one in a MOT is ionized. This could imply a simplification in the experimental configuration, and the possibility of getting read of the accelerating electrodes. Another benefit would be the practical possibility of transferring, without modifications, not only the transverse but also the longitudinal dynamical features of the atoms to the ions. For example, in our experiment there would be the possibility to obtain ions with an average longitudinal energy of only 100 μeV, with an energy spread of 25 μeV. Such low translational energy charges could be have interesting applications in probing surface chemistry or in alternative implementations of ion microscopy.

Conclusions

In this thesis we reported the production of a Cesium atomic beam by means of laser cooling techniques and its photoionization. A comprehensive analysis of the atomic beam has been carried out, based on a variety of diagnostics such as, fluorescence imaging at different distances from the pyramidal-MOT, absorption spectroscopy, optical time-of-flight. The results demonstrate that the atomic beam owns peculiar dynamical properties, in particular in terms of longitudinal and transverse velocity distribution. The average value of the longitudinal velocity is on the order of ten m/s, with a spread on the order of m/s, accompanied by a few mrad divergence: such features motivate the names "slow" and "cold" we have attributed to our atomic beam. Thanks to them, the beam can find applications where sources of particles with controlled and rather homogeneous dynamical properties are required, including atom lithography, as demonstrated in the past.

The main motivation behind photoionization of the Cesium beam was to set the basis for exploring the capabilities of the slow and cold beam in producing an ion beam. This part of the research was carried out within the frame of a European industry-oriented collaboration (FP7-MC-IAPP Project "COLDBEAMS") aimed at exploiting laser manipulation tools for the realization of unconventional charged particle beams with superior dynamical properties. The technology presently used for instance in FIB columns is in fact based on beams with "thermal" velocity distribution, that leads to non-monochromatic samples severely suffering chromatic aberration in the focusing stage.

To this aim, a two-color photoionization scheme has been implemented, involving resonant excitation of Cesium 6P atoms and interaction with 405

nm photons. The choice of this scheme has been mostly dictated by its simplicity, that allows us to get rid of complicated excitation pathways such as, for instance, those involving highly-excited states. On the other hand, coherently with the exploration stage of this part of the research, no specific effort has been devoted to attain dense ion beams. For instance, a low power laser has been used for ionization, providing some ten mW 405 nm radiation in the interaction region. Moreover, a small ionization volume has been realized, that helped to geometrically define the ion production region in the characterization measurements.

Analysis of the ion yield required to integrate a charge detector into the pre-existing ultra-high vacuum system. Two different collection geometries have been used, with the line-of-sight axis either parallel or orthogonal with respect to the beam longitudinal direction. Rather than looking at the greatest collection and detection efficiency, the design was inspired by the requirement of leaving the widest possible optical access, in order to allow for different measurement configurations. Photoionization was demonstrated and the rate estimated on the order of about $3 \cdot 10^6$ s^{-1}. The corresponding ion current is on the order of 0.5 pA, a value which is obviously much smaller than the typical current of commercial FIB columns based on field emission ionization from liquid metal sources (LMIS). Achieving a practically usable ion current was indeed beyond the scope of the present research. We remark once more that the photoionization rate might easily increase by using more intense ionization laser beams. Moreover, the flux of the neutral atom beam might also get larger when implementing trapping lasers with larger power, as allowed by the present technologies.

A preliminary insight into the dynamical properties of the ion beam has been given by ion time-of-flight measurements upon pulsed laser ionization. Interpretation of the results required a careful description of the electric fields in the collection region, which, while not being optimized by design for this specific purpose, were numerically simulated. The results demonstrate that, owing to the peculiar features of the neutral atom beam, the ions exhibit a rather monochromatic longitudinal energy distribution. In particular $\Delta E_{long} = 2.4$ eV and $\Delta E_{long}/\langle E_{long} \rangle \approx 0.1$, essentially limited by the size of

the ionizing laser beam and by the weak collection field. At present, such properties are comparable to those of LMIS beams. Furthermore, no evidence was found for space charge Coulomb effects, as expected due to the charge yield achieved.

There is a number of improvements which deserve to be tested in the future, including for instance the design and realization of highly efficient ion extraction configurations and tight focusing of the ionizing laser beam. They are expected to improve the ion beam monochromaticity up to unprecedented levels.

Therefore, we can conclude by stating that the basic idea underlying the research, i.e., that the dynamical properties of the slow and cold neutral beam can be transferred, to some extent, to the charged beam, is provisionally confirmed within the accuracy allowed by the present, exploratory, experiments. As already mentioned, further efforts have to be spent in order to achieve a practically usable ion source with a performance in line, or better, than what offered by the conventional technologies. Among others, efforts should be also devoted to investigate and eventually demonstrate the ability of laser manipulation tools to attain deterministically controlled bunches of ions with well defined dynamical properties. Such a task can hardly be conceived with conventional approaches, where the inherently thermal character of the ion sample prevents a reliable control of the velocity, position and density of the ion bunch. On the contrary, suitable laser manipulation schemes might be implemented to achieve deterministic control, in terms of velocity and number, in the neutral atom source which, once duly ionized, might result in the realization of ion packets with engineered properties.

From the applicative point of view, the availability of such ion bunches, controlled at the level of the single ion, might pave the way for innovative exploitation of the ion beams in single atom technologies, for instance in the precision doping of materials. The conventional FIBs, where on the contrary a large beam brightness is searched with a consequently huge flux of charges, cannot be employed to this aim, which hence would represent a significant extension of the technique capabilities. Preliminary efforts towards such a direction, not reported in this thesis, have been already made, for instance

through the implementation of a pushing laser beam to control the extraction of cold atoms out of the pyramidal MOT.

The thesis reported also a comprehensive study of optical pumping effects, which can be regarded, in some sense, as part of those efforts. In fact, properly designed optical pumping schemes and the engineered creation of "dark" (not absorbing) states, might be used as an additional handle to control the neutral atom beam prior and independently of ionization. Optical pumping has been an important branch of vapor spectroscopy since a long time, fostering a large variety of researches on alkali atoms. At the best of our knowledge, however, the thesis brings results allowing an unprecedented accuracy in the description of the associated phenomena. The reasons lie essentially in the peculiar features of the atomic beam, for instance in its small longitudinal velocity (leading to long interaction times) and strong collimation (leading to negligible Doppler effects). Moreover, the availability of the highly sensitive and non obtrusive detection system enabled by ionization and charge collection allowed us to extend the range of investigated parameters (hyperfine transition, excitation laser intensity) compared to previous investigations based on optical diagnostics, ensuring neat and reliable results. The quality of the collected spectroscopy information can be inferred from the excellent agreement with the theoretical predictions, based on numerical simulations of the interaction between the laser radiation and a multi-level system accurately describing the Cesium atom.

Bibliography

[1] D. Meschede and H. Metcalf. Atomic nanofabrication: atomic deposition and lithography by laser and magnetic forces. *J. Phys. D: Appl. Phys.*, 36:R17, 2003.

[2] M. K. Oberthaler and T. Pfau. One-, two- and three-dimensional nanostructures with atom lithography. *J. Phys.: Condens. Matter*, 15:R233, 2003.

[3] C. O Dwyer, G. Gay, B. Viaris de Lesegno, J. Weiner, A. Camposeo, F. Tantussi, F. Fuso, M. Allegrini, and E. Arimondo. Atomic nanolithography patterning of submicron features: writing an organic self-assembled monolayer with cold, bright Cs atom beams. *Nanotechnology*, 16:1536, 2005.

[4] J. Li, D. Stein, C. McMullan, D. Branton, M. J. Aziz, and J. A. Golovchenko. Ion-beam sculpting at nanometre length scales. *Nature*, 412:166, 2001.

[5] J. Melngailis. Focused ion beam technology and applications. *J. Vac. Sci. Technol. B*, 5:469, 1987.

[6] International technology roadmap for semiconductors. Technical report, SEMATECH, 2011.

[7] IBM Builds World's Smallest SRAM Memory Cell. http://www-03.ibm.com/press/us/en/pressrelease/24942.wss. Press Release, August 2008.

[8] C. Mack. *Fundamental Principles of Optical Lithography: The Science of Microfabrication.* Wiley, 2008.

[9] T. Ito and S. Okazaki. Pushing the limits of lithography. *Nature*, 406:1027, 2000.

[10] H. Meiling, V. Banine, H. Meijer, N. Harned, B. Blum, and P. Kuerz. Development of the ASML EUV alpha demo tool. In *Proc. SPIE 5751*, volume 90, 2005.

[11] M. Kohler and W. Fritzsch. *Nanotechnology. An introduction to nanostructuring techniques.* Wiley-VCH, 2004.

[12] A. N. Broers, W. Molzen, J. Cuomo, and N. Wittels. Electron beam fabrication of 80 angstrom metal structures. *Appl. Phys. Lett.*, 29:596, 1976.

[13] G. Timp, R. E. Behringer, D. M. Tennant, J. E. Cunningham, M. Prentiss, and K. K. Berggren. Using light as a lens for a submicron, neutral-atom lithography. *Phys. Rev. Lett.*, 69:1636, 1992.

[14] M. Prentiss, G. Timp, N. Bigelow, R. E. Behringer, and J. E. Cunningham. Using light as a stencil. *Appl. Phys. Lett.*, 60:1027, 1992.

[15] J. J. McClelland, E. C. Palm, and R. J. Celotta. Laser-focused atomic deposition. *Science*, 262:877, 1993.

[16] D. Meschede. Atomic nanofabrication: perspectives for serial and parallel deposition. *J. Phys.: Conf. Ser.*, 19:118, 2005.

[17] B. Rohwedder. Atom optics, a tool for nanofabrication. *Am. J. Phys.*, 75:394, 2007.

[18] R. W. McGowan, D. M. Giltner, and S. A. Lee. Light force cooling, focusing and nanometer-scale deposition of Aluminum atoms. *Opt. Lett.*, 20:2535, 1995.

[19] S. J. Rehse, R. W. McGowan, and S. A. Lee. Optical manipulation of group III atoms. *Appl. Phys. B*, 70:657, 2000.

[20] S. J. Rehse, K. M. Bockel, and S. A. Lee. Laser collimation of an atomic Gallium beam. *Phys. Rev. A*, 69:063404, 2004.

[21] B. Kloter, C. Weber, D. Haubrich, D. Meschede, and H. Metcalf. Laser cooling of an Indium atomic beam enabled by magnetic fields. *Phys. Rev. A*, 77:033402, 2008.

[22] A. Camposeo, A. Piombini, F. Cervelli, F. Tantussi, F. Fuso, and E. Arimondo. A cold cesium atomic beam produced out of a pyramidal funnel. *Opt. Comm.*, 200:231, 2001.

[23] E. Sligte, B. Smeets, K. M. R. van der Stam, R. W. Herfst, P. van der Straten, H. C. W. Beijerinck, and K. A. H. van Leeuwen. Atom lithography of Fe. *Appl. Phys. Lett.*, 85:4493, 2004.

[24] A. J. Palmer, M. Baker, and R. T. Sang. Towards creation of iron nanodots using metastable atom lithography. *Nanotechnology*, 17:1166, 2006.

[25] J. J. McClelland and J. L. Hanssen. Laser cooling without repumping: A magneto-optical trap for Erbium atoms. *Phys. Rev. Lett.*, 96:143005, 2006.

[26] R. Ohmukai, S. Urabe, and M. Watanabe. Atomic nanofabrication using an Ytterbium atomic beam. *Sci. Technol. Adv. Mat.*, 5:585, 2004.

[27] S. B. Hill and J. J. McClelland. Performance of a feedback-controlled, deterministic source of single chromium atoms. *J. Opt. Soc. Am. B*, 21:473, 2003.

[28] S. B. Hill and J. J. McClelland. Atoms on demand: Fast, deterministic production of single cr atom. *Appl. Phys. Lett.*, 82:3129, 2003.

[29] S. Yoon, T. CHoi, S. Park, J. Kim, J. Lee, and K. An. Definitve number of atoms on demand: controlling the number of atoms in a few-atom magneto-optical trap. *Appl. Phys. Lett.*, 88:211104, 2006.

[30] F. Ruschewitz, D. Bettermann, J. L. Peng, and W. Ertmer. Statistical investigations on single trapped neutral atoms. *Europhys. Lett.*, 34:651, 1996.

[31] D. K. Poon, J. M. Dykes, C. Choo, J. T. K. Tsui, J. Wang, G. H. Chapman, Y. Tu, P. Reynolds, and A. Zanzal. Adding grayscale layer to chrome photomasks. In *Society of Photo-Optical Instrumentation Engineers (SPIE) Conference Series*, volume 6349, 2006.

[32] L. A. Giannuzzi and F. A. Stevie. *Introduction to focused ion beams: Instrumentation, theory, techniques and practice*. Springer, 2005.

[33] K. Nikawa. Applications of focused ion beam technique to failure analysis of very large scale integrations: A review. *J. Vac. Sci. Technol. B*, 9:2566, 1991.

[34] P. D. Prewett and P. J. Heard. Repair of opaque defects in photomasks using focused ion beams. *J. Phys. D: Appl. Phys.*, 20:1207, 1987.

[35] B. W. Ward, J. A. Notte, and N. P. Economou. Helium ion microscope: A new tool for nanoscale microscopy and metrology. *J. Vac. Sci. Technol. B*, 24:2871, 2006.

[36] L. A. Giannuzzi and F. A. Stevie. A review of focused ion beam milling techniques for TEM specimen preparation. *Micron*, 30:197, 1999.

[37] S. Reyntjens and R. Puers. A review of focused ion beam applications in microsystem technology. *J. Micromech. Microeng.*, 11:287, 2001.

[38] J. Orloff. High-resolution focused ion beams. *Rev. Sci. Instrum.*, 64:1105, 1993.

[39] V. E. Krohn and G. R. Ringo. Ion source of high brightness using liquid metal. *Appl. Phys. Lett.*, 27:479, 1975.

[40] P. D. Prewett and D. K. Jefferies. Characteristics of a gallium liquid metal field emission ion source. *J. Phys. D: Appl. Phys.*, 13:1747, 1980.

[41] J. Orloff and L. W. Swanson. Fine focus ion beams with field ionization. *J. Vac. Sci. Technol.*, 15:845, 1978.

[42] S. K. Guharay, E. Sokolovsky, and J. Orloff. Characteristics of ion beams from a Penning source for focused ion beam applications. *J. Vac. Sci. Technol. B*, 17:2779, 1999.

[43] C. Wilbertz, T. Maisch, D. Huttner, K. Bohringer, K. Jousten, and S. Kalbitzer. A focused gas-ion beam system for submun application. *Nucl. Instrum. Meth. B*, 63:120, 1992.

[44] L. Scipioni, D. Stewart, D. Ferranti, and A. Saxonis. Performance of multicusp plasma ion source for focused ion beam applications. *J. Vac. Sci. Technol. B*, 18:3194, 2000.

[45] S. B. van der Geer, M. P. Reijinders, M. J. de Loos, E .J. D. Vredenbregt, P. H. A. Mutsaers, and O. J. Luiten. Simulated performance of an ultracold ion source. *J. Appl. Phys.*, 102:094312, 2007.

[46] B. J. Claessens, S. B. van der Geer, G. Taban, E. J. D. Vredenbregt, and O. J. Luiten. Ultracold electron source. *Phys. Rev. Lett.*, 95:164801, 2005.

[47] B. J. Claessens, M. P. Reijinders, G. Taban, O. J. Luiten, and E. J. D. Vredenbregt. Cold electron and ion beams generated from trapped atoms. *Phys. Plasmas*, 14:093101, 2007.

[48] J. L. Hanssen, J. J. McClelland, and E. A. Dakin. Laser-cooled atoms as a focused ion-beam source. *Phys. Rev. A*, 74:063416, 2006.

[49] M.P. Reijnders, P.A. van Kruisbergen, G. Taban, S.B. Van der Geer, P.H.A. Mutsaers, E.J.D. Vredenbregt, and O.J. Luiten. Low-energy-spread ion bunches from a trapped atomic gas. *Phys. Rev. Lett.*, 102:034802, 2009.

[50] M. P. Reijinders, N. Debernardi, S. B. van der Geer, P. H. A. Mutsaers, E. J. D. Vredenbregt, and O. J. Luiten. Phase-space manipulation of ultracold ion bunches with time-dependent fields. *Phys. Rev. Lett.*, 105:034802, 2010.

[51] M. P. Reijinders, N. Debernardi, S. B. van der Geer, P. H. A. Mutsaers, E. J. D. Vredenbregt, and O. J. Luiten. Time-dependent manipulation of ultracold ion bunches. *J. Appl. Phys.*, 109:033302, 2011.

[52] J. L. Hanssen, S. B. Hill, J. Orloff, and J. J. McClelland. Magneto-optical-trap-based, high brightness ion source for use as a nanoscale probe. *Nano Letters*, 8:2844, 2008.

[53] P. Normand, E. Kapetanakis, P. Dimitrakis, D. Skarlatos, K. Beltsios, D. Tsoukalas, C. Bonafos, G. Ben Assayag, N. Cherkashin, A. Claverie, J. A. Van den Berg, V. Soncini, A. Agarwal, M. Ameen, M. Perego, and M. Fanciulli. Nanocrystals manufacturing by ultra-low-energy ion-beam-synthesis for non-volatile memory applications. *Nucl. Instr. and Meth. in Phys. Res. B*, 216:228, 2004.

[54] D.A. Steck. Cesium D line data. 1998.

[55] L. I. Schiff. *Quantum Mechanics*. McGraw-Hill, 1949.

[56] C. Cohen-Tannoudjii, B. Diu, and F. Laloe. *Quantum Mechanics*. Wiley-Interscience, 2006.

[57] D. J. Wineland and W. M. Itano. Laser cooling of atoms. *Phys. Rev. A*, 58:699, 1979.

[58] S. Stenholm. The semiclassical theory of laser cooling. *Rev. Mod. Phys.*, 13:699, 1986.

[59] T. W. Hänsch and A. L. Schawlow. Cooling of gases by laser radiation. *Opt. Comm.*, 13:68, 1975.

[60] H. Metcalf and P. van der Straten. *Laser cooling and trapping*. Springer, 2001.

[61] E. L. Raab, M. Prentiss, A. Cable, S. Chu, and D.E. Pritchard. Trapping of neutral sodium atoms with radiation pressure. *Phys. Rev. Lett.*, 59:2631, 1987.

[62] K. H. Kim, K. I. Lee, H. R. Noh, and W. Jhe. Cold atomic beam produced by a conical mirror funnel. *Phys. Rev. A*, 64:013402, 2001.

[63] K. I. Lee, J. A. Kim, H. R. Noh, and W. Jhe. Single-beam atom trap in a pyramidal and conical hollow mirror. *Opt. Lett.*, 21:1177, 1996.

[64] J. J. Arlt, O. Maragò, S. Webster, S. Hopkins, and C. J. Foot. A pyramidal magneto-optical trap as a source of slow atoms. *Opt. Comm.*, 157:303, 1998.

[65] I. Sydoryk, N. N. Bezuglov, I. I. Beterov, K. Miculis, E. Saks, A. Janovs, P. Spels, and A. Ekers. Broadening and intensity redistribution in Na(3p) hyperfine excitation spectra due to optical pumping in the weak excitation limit. *Phys. Rev. A*, 77:042511, 2008.

[66] T. Lindvall and I. Tittonen. Interaction-time-averaged optical pumping in alkali-metal-atom doppler spectroscopy. *Phys. Rev. A*, 80:032505, 2009.

[67] J. Sagle, R.K. Namiotka, and J. Huennekens. Measurement and modelling of intensity dependent absorption and transit relaxation on the Cesium D1 line. *J. Phys. B: At. Mol. Opt. Phys.*, 29:2629, 1996.

[68] P. Siddons, C. S . Adams, C. Ge, and I. Hughes. Absolute absorption on rubidium D lines: comparison between theory and experiment. *J. Phys. B: At. Mol. Opt. Phys.*, 41:155004, 2008.

[69] G. Moon, M. Heo, S. Shin, H. Noh, and W. Jhe. Calculation of analytic populations for a multilevel atom at low laser intensity. *Phys. Rev. A*, 78:015404, 2008.

[70] R. Loudon. *The quantum theory of light.* Oxford University Press, 1983.

[71] L. P. Maguire, R. M. W. van Bijnen, E. Mese, and R. E. Scholten. Theoretical calculation of saturated absorption spectra for multi-level atoms. *J. Phys. B: At. Mol. Opt. Phys.*, 39:2709, 2006.

[72] I. I. Sobelman. *Atomic spectra and radiative transitions*. Springer, 1992.

[73] M. L. Harris, C. S . Adams, S. L. Cornish, I. C. McLeod, E. Tarleton, and I. G. Hughes. Polarization spectroscopy in rubidium and cesium. *Phys. Rev. A*, 73:062509, 2006.

[74] P. Hannaford and D. C. McDonald. Determination of relative oscillator strengths of the copper resonance lines by atomic absorption spectroscopy. *J. Phys. B: At. Mol. Opt. Phys.*, 11:1177, 1978.

[75] W. K. Hensinger, A. G. Truscott, H. Rubinsztein-Dunlop, and N.R. Heckenberg. Variations of relative line intensity in saturation spectroscopy due to low magnetic field. *Opt. Quant. Electron.*, 31:391, 1999.

[76] D. A. Smith and I. G. Hughes. The role of hyperfine pumping in multilevel systems exhibiting saturated absorption. *Am. J. Phys.*, 72:631, 2004.

[77] S. R. Shin and H. R. Noh. Calculation of the absorption coefficient for a doppler-broadened multilevel atom. *J. Korean. Phys. Soc.*, 56:195, 2010.

[78] P.G. Pappas, M. M. Burns, D. D. Hinshelwood, M. S. Feld, and D. E. Murnick. Saturation spectroscopy with laser optical pumping in atomic barium. *Phys. Rev. A*, 21(6):1955, 1980.

[79] B. Gao. Effects of zeeman degeneracy on the steady-state properties of an atom interacting with a near-resonant laser field: analitic result. *Phys. Rev. A*, 48:2443, 1993.

[80] J.J. McClelland and M.H. Kelley. Detailed look at aspects of optical pumping in sodium. *Phys. Rev. A*, 31:3704, 1985.

[81] T. J. O'Kane, R. E. Scholten, P. M. Farrel, and M. R. Walkiewicz. Nonlinear interactions of multilevel atoms with a near-resonant standing wave. *Phys. Rev. A*, 59:4485, 1999.

[82] K. Blum. *Density Matrix. Theory and applications.* Plenum Press, 1996.

[83] F. Renzoni, W. Maichen, L. Windholz, and E. Arimondo. Coherent population trapping with losses observed on the hanle effect of the d_1 sodium line. *Phys. Rev. A*, 55:3710, 1997.

[84] P. D. Lett, R. N. Watts, C. I. Westbrook, W. D. Phillips, P. L. Gould, and H. J. Metcalf. Observation of atoms laser-cooled below the Doppler limit. *Phys. Rev. Lett.*, 61:169, 1988.

[85] J. Dalibard and C. Cohen-Tannoudjii. Laser cooling below the Doppler limit by polarization gradients: simple theoretical models. *J. Opt. Soc. Am. B*, 6:2023, 1989.

[86] J. Dalibard and C. Cohen-Tannoudjii. Dressed-atom approach to atomic motion in laser light: the dipole force revisited. *J. Opt. Soc. Am. B*, 2:1707, 1985.

[87] C. Salomon, J. Dalibard, W. D. Phillips, A. Clairon, and S. Guellati. Laser cooling of Cesium atoms below 3 μK. *Europhys. Lett.*, 12:683, 1990.

[88] S. I. Chin and R. Lambropoulos, editors. *Multiphoton ionization of atoms.* Academic Press, 1984.

[89] Ian G. Brown, editor. *The Physics and Technology of Ion Sources.* Wiley-VCH, 2004.

[90] J. Orloff, M. Utlaut, and L. Swanson. *High resolution focused ion beams.* Plenum Press, 2003.

[91] G. D. Alton and P. M. Read. The emittance characteristics of a gallium liquid-metal ion source. *J. Appl. Phys.*, 66:1018, 1989.

[92] J. L. Hanssen, E. A. Dakin, J. J. McClelland, and M. Jacka. Using laser-cooled atoms as a focused ion beam source. *J. Vac. Sci. Technol. B*, 24:2907, 2006.

[93] A. V. Steele, B. Knuffman, and J. J. McClelland. Inter-ion coulomb interactions in a magneto-optical trap ion source. *J. Appl. Phys.*, 109:104308, 2011.

[94] R. L. Seliger, J. W. Ward, V. Wang, and R. L. Kubena. A high intensity scanning ion probe with submicrometer spot size. *Appl. Phys. Lett.*, 34:310, 1979.

[95] K. J. Nygaard, R. E. Hebner, J. D. Jones, and R. Corbin. Photoionization of the $6^2P_{3/2,1/2}$ fine-structure levels in Cesium. *Phys. Rev. A*, 12:1440, 1975.

[96] V. Letokhov. *Laser Control of Atoms and Molecules*. Oxford University Press, 2007.

[97] E. H. A. Granneman and M. J. Van der Wiel. Two-photon ionization measurements on atomic caesium by means of an argon ion laser. *J. Phys. B: At. Mol. Opt. Phys.*, 8:1617, 1975.

[98] M. R. Teague, P. Lambropoulos, D. Goodmanson, and D. W. Norcross. Theory of two-photon ionization of cesium. *Phys. Rev. A*, 14:1057, 1976.

[99] D. H. Pollock and A. O. Jensen. Absorption of resonance radiation and formation of molecular ions in cesium vapor. *J. Appl. Phys.*, 36:3184, 1965.

[100] M. Gryzinski. *Atomic collision processes*. North-Holland, 1964.

[101] A. Camposeo, F. Cervelli, A. Piombini, F. Tantussi, F. Fuso, M. Allegrini, and E. Arimondo. A laser-cooled atom beam for nanolithography applications. *Mater. Sci. Eng. C*, 23:217, 2003.

[102] H.R. Noh and W. Jhe. Atom optics with hollow optical system. *Phys. Rep.*, 372:269, 2002.

[103] T. M. Roach and D. Henclewood. Novel rubidium atomic beam with an alkali dispenser source. *J. Vac. Sci. Technol. A*, 22:2384, 2004.

[104] J.D. Jackson. *Classical electrodynamics*. New York: Wiley, 1999.

[105] K. C. Harvey and C. J. Myatt. External-cavity diode laser using a grazing-incidence diffraction grating external-cavity diode laser using a grazing-incidence diffraction grating external-cavity diode laser using a grazing-incidence diffraction grating. *Opt. Lett.*, 16:910, 1991.

[106] C. E. Wieman and L. Hollberg. Using diode lasers for atomic physics. *Rev. Sci. Instrum.*, 62:1, 1991.

[107] Z. T. Lu, K. L. Corwin, M. J. Renn, M. H. Anderson, E. A. Cornell, and C. E. Wieman. Low-velocity intense source of atoms from a magneto-optical trap. *Phys. Rev. Lett.*, 77:3331, 1996.

[108] M. Walhout, U. Sterr, and S. L. Rolston. Magnetic inhibition of polarization-gradient laser cooling in $\sigma_+ - \sigma_-$ optical molasses. *Phys. Rev. A*, 54:2275, 1996.

[109] C. Valentin, M. C. Gagne, J. Yu, and P. Pillet. One-dimension sub-Doppler molasses in the presence of static magnetic field. *Europhys. Lett.*, 17:133, 1992.

[110] T. M. Brzozowski, M. Maczynska, M. Zawada, J. Zachorowski, and W. Gawlik. Time-of-flight measurement of the temperature of cold atoms for short trap–probe beam distances. *J. Opt. B: Quantum Semiclass. Opt.*, 4:62, 2002.

[111] E. Riis, D. S. Weiss, K. A. Moler, and S. Chu. Atom funnel for the production of a slow, high density atomic beam. *Phys. Rev. Lett.*, 64:1658, 1990.

[112] J. Yu, J. Djemaa, P. Nosbaum, and P. Pillet. Funnel with orientated Cesium atoms. *Opt. Comm.*, 112:136, 1994.

[113] L. Cacciapuoti, A. Castrillo, M. de Angelis, and G. M. Tino. A continuous cold atomic beam from a magneto-optical trap. *Eur. Phys. J. D*, 15:245, 2001.

[114] K. Dieckmann, R. J. C. Spreeuw, M. Weidemuller, and J. T. M. Walraven. Two-dimensional magneto-optical trap as a source of slow atoms. *Phys. Rev. A*, 58:3891, 1998.

[115] C. Slowe, L. Vernac, and L. V. Hau. High flux source of cold Rubidium atoms. *Rev. Sci. Instrum.*, 76:103101, 2005.

[116] A. Scholz, M. Christ, D. Doll, J. Ludwig, and W. Ertmer. Magneto-optical preparation of a slow, cold and bright Ne* atomic beam. *Opt. Comm.*, 111:155, 1994.

[117] T. B. Swanson, N. J. Silva, S. K. Mayer, J. J. Maki, and D.H. McIntyre. Rubidium atomic funnel. *J. Opt. Soc. Am. B*, 13:1833, 1996.

[118] R. S. Williamson, P. A. Voytas, R. T. Newell, and T. Walker. A magneto-optical trap loaded from a pyramidal funnel. *Opt. Expr.*, 3:111, 1998.

[119] H. Chen and E. Riis. Cold atomic beam from a rubidium funnel. *Appl. Phys. B*, 70:665, 2000.

[120] J. M. Kohel, J. Ramirez-Serrano, R. J. Thompson, L. Maleki, J. L. Bliss, and K. G. Libbrecht. Generation of an intense cold-atom beam from a pyramidal magneto-optical trap: experiment and simulation. *J. Opt. Soc. Am. B*, 20:1161, 2003.

[121] F. F. Chen. *Introduction to plasma physics.* Plenum Press, 1974.

[122] T. C. Killian, S. Kulin, S. D. Bergeson, L. A. Orozco, C. Orzel, and S. L. Rolston. Creation of an ultracold neutral plasma. *Phys. Rev. Lett.*, 83:4776, 1999.

[123] Luc Devroye. *Non-Uniform Random Variate Generation.* Springer-Verlag, 1986.

[124] B. G. Freinkman, A. V. Eletskii, and S. I. Zaitsev. A proposed laser source of ions for nanotechnology. *Microelectron. Eng.*, 73-74:139, 2004.